UNIVERSITY OF OKLAHOMA

GRADUATE COLLEGE

GENERATION AND CONTROL OF ATOMIC RESONANT SQUEEZED LIGHT

A DISSERTATION

SUBMITTED TO THE GRADUATE FACULTY

in partial fullfillment of the requirements for the

Degree of

DOCTOR OF PHILOSOPHY

By

SAESUN KIM
Norman, Oklahoma
2022

GENERATION AND CONTROL OF ATOMIC RESONANT SQUEEZED LIGHT

A DISSERTATION APPROVED FOR THE
HOMER L. DODGE DEPARTMENT OF PHYSICS AND ASTRONOMY

BY THE COMMITTEE CONSISTING OF

Dr. Alberto M. Marino, Chair

Dr. Arne Schwettmann

Dr. Bruno Uchoa

Dr. Doerte Blume

Dr. Zhisheng Shi

To Truth

Acknowledgements

I would like to first thank Dr. Alberto Marino, who has mentored me for 7 years. He provides tremendous support, shows how to develop a physicist mindset and care for details. His influence affects me and will move me in the right direction in my future endeavors. I wish to thank the members of my committee, Dr. Doerte Blume, Dr. Arne Schwettmann, Dr. Bruno Uchoa, Dr. Zhisheng Shi for walking with me a long journey of the Ph.D program. Especially Dr. Doerte Blume and Dr. Arne Schwettmann for their kind support throughout my Ph.D. I would like to thank Tim Woodworth, Dr. Marino and the committee members for his assistance in preparing this document.

It all started when I came to America. I met Odelle Lee Paulson and we lived together during my high school exchange program in the US. He showed me a lot of the world through art and music. During my high school in Wabu and Minnewaska, I was fortunate enough to meet my high school close friends, Tyler, Junyong, and Suyoun. After graduating from high school, I took a short vacation as a working holiday in Australia while performing street magic tricks and working at a Korean restaurant. During my time in Sydney, I was so grateful to spend time with Jiwon, Chungman, Tracy, and co-workers at Madang. I have gained a lot of experience which laid the foundation for my social life.

After a short vacation, I was admitted to a small liberal arts college, University of Minnesota Morris. I acquired a lot of knowledge and, learned research methods while working with Dr. Michael Korth, Dr. Jong-min Kim, Dr. Catherine Smith, Dr.

Sylke Boyd, Dr. David Roberts, Dr.Peter Dolan, and Dr. Barry McQuarrie. So many people helped me during my university years, but I would like to especially thank Nancy Pederson and David Israels-Swenson. Of course I can't forget people I met: Al, Jaehoon, Yuna, Wang, Cassie, Seungjun, Natalie, Amber, Yejin, Junho, and Elsie Willson.

After graduation, I have started my PhD in Physics at the University of Oklahoma. A lot of things have changed from the time I joined the program, and it was a very meaningful moment to be part of the transformation to the Center for Quantum Research and Technology.

The PhD was very difficult, but I learned a lot from Dr. Ashok Kumar, who cared for and loved me; my lab colleague Tim provided inspiration and systematic knowledge of physics and religion; Gaurav taught me how to do a deeper dive into physics and many good philosophical discussion; Umang, Kit and Daida who worked with me showed great patience with my young mentorship; Sho Onoe collaborating with my multipartite project. Thank you for amazing team at the electronic and mechanical shop: Alex Rybicki, Chad Cunningham, and Berry Bergeron. I've been meeting a lot of people over the past 7 years, and I'm so happy to spend brief time with Matthew, Joseph, Anita, Quang, Hio, Delaram, Mingoo, Jiung, Mimbo, Sunghyun, Kiwon, Kyuran, Van, Jumin, Irene, Kay, Hua, Seunggyu, Yujin, Thomas, Taemin, Junhyeong, Gyuseung, Jaekwon, Grace, Bumgi, Shan, Taekoung, Kelly, Sam, Ricky, Ritaban, TK, Quang, Elderied, Sangwook, Yongjae, Seowoo and the team members of Entango.

During my Ph.D. program at the Center for Quantum Research and Technology at the University of Oklahoma, I was able to learn not only physics, but also understand the purpose of my life. I want to express my gratitude to Pastor Chang for letting me understand what really matters and help me see the world. Thank you Dr. Michael Strauss and Dr. Doerte Blume for good discussion and influence through your leadership. Travis Scholten's strong mentoring on career and life direction, Tom Wavering and Drew Hendricks on entrepreneurship experience, Sean Oh on building an insight of quantum business, and Shin Soyoung's strong mentoring on self-confidence have made me what I am today and I am looking forward to seeing what happens next. Alex Rybicki at the machine shop, I was able to learn and gain broad range of wisdom which I cannot have learnt elsewhere.

I am so honored to have my grandfather, Kijoong, who conveyed good beliefs and vision, my uncle Yuntae as my role model, Haeun for being my adorable cousin, and my step father pastor Sewoo, thank you for loving my mother. Thank you all my family members: Misun, Bosoon, Sunghyun, Yunhong, Seunghan, Yonghee, Jinhae, Hwanil, Jangwoo, Jihae, Inha, Juha, Jiwoo and Connie.

I would like to express my gratitude with all my soul to my mother, sister and Jisu who protected and stayed with me during the difficult and the lowest moments during my doctoral course. Last but not least, I would like to thank my father SeongHoon, friend Taejin, my grandmother Boseok, my grandfather Odelle Lee Paulson for taking the brief journey with me. Your memories will always be with me.

Table of Contents

List of Tables

List of Figures

Abstract

Quantum metrology is a new emerging technology studying of extreme sensitive and high resolution measurement based on quantum mechanical principles such as quantum entanglement and squeezing, which can potentially revolutionize modern technology for defense and national security [1].

Squeezed light plays a fundamental role in quantum metrology due to its reduced noise properties. Recently, it was used to increase the sensitivity of the LIGO interferometer to measure gravitational waves and provide new ways to observe the universe. Additionally, a quantum advantage has also been demonstrated in other optical devices such as plasmonic sensors and quantum imaging. However, there are still many challenges and opportunities for squeezed light to be adopted to current sensors and other systems. Therefore, the focus of this dissertation is to extend the applicability of squeezed light to atomic sensors and enable a control of quantum noise. To extend the applicability of squeezed light to atomic systems, it must have a frequency close to or on atomic resonance and a narrow linewidth to obtain an efficient interaction with atomic ensembles. Therefore, there is substantial interest in generating narrowband squeezed light on atomic resonance. The successful demonstration of atomic resonance squeezed light and the effective control of the noise properties of squeezed light can enable improved sensitivity of atomic-based sensors and deterministic transfer of the quantum correlation between two distant atomic ensembles.

In the first part of the dissertation, we present three different approaches to generate

two-mode atomic resonant squeezed light with a four-wave mixing (FWM) processes in hot ^{85}Rb. First, we take advantage of the proximity of the energy levels in the D1 line of ^{85}Rb and ^{87}Rb to demonstrate the generation of resonant squeezed light with a non-degenerate FWM in which one mode is on resonance with the D1 $F = 2$ to $F' = 2$ transition and the other mode is on resonance with the $F = 1$ to $F' = 1$ transition in the D1 line of ^{87}Rb. For this configuration, we obtain an intensity difference squeezing level of -3.9 dB. Moreover, the intensity difference squeezing increases to -6.3 dB and -6.2 dB when only one of the modes of the squeezed state is resonant with the D1 $F = 2$ to $F' = 2$ or $F = 1$ to $F' = 1$ transition of ^{87}Rb, respectively.

Another approach used to generate resonant squeezed light is via the coupling with additional pump beam to enhance the atomic processes. We apply an optical beam to transfer population between the ground states, dress the atomic system, or saturate the transition to enhance FWM process. We measure -0.8 dB of intensity difference squeezing when both probe and conjugate are simultaneously on resonance with the D1 $F = 3$ to $F' = 3$ transition of ^{85}Rb and -1 dB of intensity difference squeezing when the probe is resonant with the D2 $F = 2$ to $F' = 3$ transition of ^{87}Rb.

While the first two approaches generate resonant squeezed light for certain transitions, there are still many transitions that we cannot reach with our techniques. To overcome this limitation, we dress the atomic state via an external DC electric field to increase the frequency tunability of the two-mode squeezed light. We design a vacuum chamber with parallel plates to apply large electric fields of up to 110 kV/cm to the atomic vapor source. Our work increases the frequency tunability of the squeezed

light to 600 MHz, demonstrating the generation of squeezed light resonant with the D1 $F = 3$ to $F' = 3$ transition of ^{85}Rb.

In the second part of the dissertation, we discuss two different methods of controlling the properties of two-mode squeezed light to generate single-mode squeezed light and multipartite entangled light. We obtained a single-mode squeezed state with a squeezing level of -2.9 dB by transferring the intensity quantum correlations present in the twin beams to a single beam using a feedforward technique. In the last chapter, we introduce a novel scheme to generate scalable genuine multipartite entanglement. We show configurations of the proposed scheme that can generate genuine quadpartite, hexapartite, and octapartite entanglement, which we verify through a violation of the positive partial transpose (PPT) criterion.

The generation of resonant squeezed light using atomic ensembles overcomes several experimental difficulties associated with other sources and make it possible to study the interaction between atoms and quantum states of light. Thus, our work will be a building block for quantum metrology based on squeezed light, particularly important for atomic sensing and quantum information science.

List of Acronyms

AOM	acousto-optical modulator	**EOM**	electro-optic modulator
BS	beam splitter	**PPKTP**	periodically poled potassium titanyl phosphate
PBS	polarizing beamsplitters	**ND**	neutral density
FWM	four-wave mixing	**EIT**	electromagnetically induced transparency
LIGO	laser interferometer gravitational-wave observatory	**GME**	genuine multipartite entanglement
PPT	positive partial transposition	**CM**	covariance matrix
PA	parametric amplifier	**QNL**	quantum noise limit
OPO	optical parametric oscillator	**UV**	ultraviolet
BEC	Bose-Einstein condensate	**DC**	direct current

Chapter 1

Introduction

> *My thought is me: that's why I can't stop. I exist because I think… and I can't stop myself from thinking. At this very moment - it's frightful - if I exist, it is because I am horrified at existing. I am the one who pulls myself from the nothingness to which I aspire.*
>
> - Jean-Paul Sartre, *Nausea*

Quantum technology is a newly emerging field that relies on quantum mechanical principles such as entanglement, superposition, and quantum coherence. It is becoming the foundation for the fourth industrial revolution [2]. Among the quantum technologies that will emerge from this revolution are quantum computers, quantum communication systems, and quantum sensors [1]. Quantum computers will provide an exponential increase in computational power for specific problems in machine learning, drug development, battery design, and financial analysis [3]. Quantum sensors can enhance the sensitivity of devices that are used in self-driving cars, medical devices, and satellites [4]. Finally, as sensors and devices will become interconnected and exchange data with other systems over the internet, securing the internet of things has become a critical problem to address in order to protect the privacy of individuals. To this end, quantum communications can enable a network that is fundamentally secure against possible attacks from an eavesdropper [5].

To take advantage of quantum technology, it is crucial to generate and control quantum systems such as superconducting circuits, entangled photons, and cold-atomic ensembles. For example, in the case of light, squeezed states are a quantum resource that have gained significant attention. These quantum states of light exhibit noise levels below the shot-noise limit, which represents the fundamental limit that can be achieved with only classical resources. This property makes it possible to enhance the sensitivity of sensors [6], the security of protocols for quantum key distribution [7], and imaging resolution [8]. More recently, squeezed states of light have also been proposed as a way to realize one-way quantum computing [9]. Atomic ensembles offer another powerful system that can take advantage of quantum resources. Their extreme sensitivity to external fields, precise control over individual atoms or atomic clouds, and the fact that all atoms are identical to each other make these systems ideal for sensing and precision measurement applications. For example, atomic ensembles such as cold atomic clouds have been used to implement high precision clocks and sensors that are applicable for GPS and medical devices [10].

Because quantum technology can be based on both light and atomic ensembles, there is considerable interest in combing these two quantum systems in a way that can exploit their unique properties [11]. To do that, an efficient interaction between the quantum light and the atomic ensemble must be implemented. Especially for cold-atom systems, light must be produced in a quantum states that is on atomic resonances and with a bandwidth of the order of 10 MHz.

Previous studies have proposed and demonstrated the techniques to use resonant

Transition	Atom	Squeezing	Method
D1 $F = 1$ to $F' = 1$	^{87}Rb	-6.2 dB	Rubidium Isotopes
D1 $F = 2$ to $F' = 2$	^{87}Rb	-6.3 dB	Rubidium Isotopes
D2 $F = 2$ to $F' = 3$	^{87}Rb	-1.5 dB	Rubidium Isotopes + Pump
D1 $F = 3$ to $F' = 3$	^{85}Rb	-1.0 dB	Degenerate FWM + Pump
D1 $F = 3$ to $F' = 3$	^{85}Rb	≈ -0.1 dB	DC Stark Shift

Table 1.1: Summary of the techniques we use to generate resonant squeezed light with corresponding level of squeezing and resonant transitions.

squeezed light to enhance the sensitivity of atomic interferometers and atomic magnetometers [11]. Unfortunately, the efficient generation of narrowband squeezed light on resonance with atomic transitions has proven to be a challenge. For instance, its generation with an optical parametric oscillator (OPO), which consists of a nonlinear crystal inside a cavity, requires pumping the nonlinear crystal with UV light [12]. At these frequencies, the parametric-down conversion process on which an OPO is based is not efficient for the generation of squeezed light. Besides, crystal-based sources tend to be complicated and require special manufacturing of the nonlinear crystal. On the other hand, while atomic-based sources offer a natural and more direct way to generate narrowband on-resonance quantum states of light that could offer the required efficient interaction, the strong absorption associated with working on resonance is a significant limiting factor.

In this thesis, we first describe the challenges and approaches for overcoming the limitations of current on-resonance sources for squeezed light, then we present three experimental efforts on the use of atomic systems to generate squeezed states of light that are resonant with different atomic transitions. The methods are based on 1) the proximity of energy levels in the two rubidium isotopes, 2) a FWM process enhanced via an additional coupling pump beam, and 3) atomic state dressing with a high voltage.

Given the proximity of the energy levels in the D1 lines of the two rubidium isotopes (^{85}Rb and ^{87}Rb), our first two approaches consist in implementing the FWM in ^{85}Rb in a regime that generates squeezed states in a configuration know as two-mode squeezing, in which the squeezing is contained in two beams, on resonance with transitions in ^{87}Rb. Then we enhance FWM process with additional coupling pump beam to generate squeezed states on resonance with transitions in ^{87}Rb and ^{85}Rb. The amount of the squeezing we have obtained with each technique is summarized in the Table 1.1. While our two approaches can generate squeezed light on resonance with specific transitions in Rb, we must increase the frequency tunability to cover more transitions in ^{87}Rb and ^{85}Rb. To overcome this limitation, we have designed a vacuum chamber with internal electrodes that can be used to apply a large electric field of over 110 kV/cm to a rubidium vapor cloud. This allows us to tune the frequency of the squeezed light using the DC Stark effect. Our work increases the frequency tunability of the squeezed light by 600 MHz while preserving -3.8 dB of squeezing. We show that the squeezed light becomes resonant with the D1 $F = 3$ to $F' = 3$ transition of ^{85}Rb as we increase the electric field.

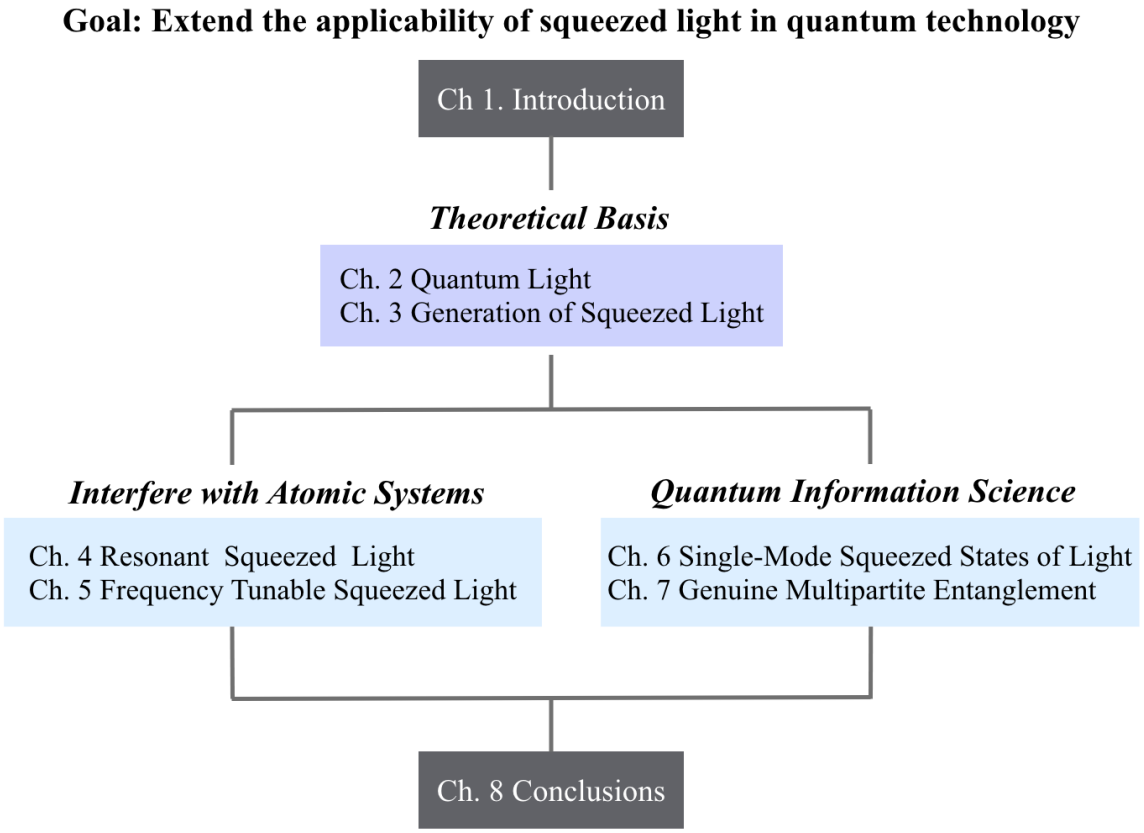

Figure 1.1: Dissertation structure.

The second part of the thesis introduces an experimental technique for transferring the quantum correlations from the two beams configuration we generate with the FWM to a single beam, as well as a novel proposal for distributing the quantum correlations to multiple beams. We show that it is possible to generate single-mode squeezed light which exhibits quantum noise reduction in the amplitude of a single beam, and theoretically describe how to extend our system to generate genuine multipartite entanglement. Our ability to generate quantum correlations in different quantum states of light promises to expand the applicability of light in quantum information science.

This dissertation is organized as shown in Fig. 1.1. In Ch. 1, we introduce the importance of the work performed as part of this dissertation and give an overview of current developments. In Ch. 2, we outline the basic definitions and characterization techniques of quantum states of light by introducing coherent and squeezed states of light and introduce the noise properties and mathematical descriptions of those states. Chapter 3 presents the method that we use for generating squeezed states of light. It discusses the FWM process that we use in our experiments and the techniques required for the characterization of the generated squeezed light.

Chapter 4 presents our first approach to generate resonant two-mode squeezed light. We present two configurations that use ^{85}Rb atomic vapor to generate either singly or doubly resonant two-mode squeezed states of light with transitions in the D1 line of ^{87}Rb and ^{85}Rb. The method presented in Ch. 4 serves as the foundation for several different techniques to generate resonant squeezed light, but its tunability is limited by atomic absorption. To overcome this limitation, we have designed a vacuum chamber with internal electrodes that can be used to apply a large electric field to a rubidium vapor cloud. We describe numerical calculations for the atomic energy levels under such a large electric field along with the detailed design of the chamber and the experimental results in Ch. 5. Chapter 6 describes the technique to generate on-resonant and off-resonant single-mode squeezed light using a feedforward technique. We present a theoretical derivation of the noise spectra after the feedforward and the results of our experimental implementation. Chapter 7 introduces our theoretical proposal to generate scalable genuine multipartite Gaussian entangled light using a

network of FWM processes. We show configurations of the proposed scheme that can generate genuine quadrapartite, hexapartite, and octapartite entanglement, which we verify through a violation of the positive partial transpose (PPT) criterion. We conclude the dissertation by summarizing the work done and providing possible future work on our squeezed light generated with an atomic ensemble in Ch. 8.

Chapter 2

Quantum Light

Man is always prey to his truths. Once he has admitted them, he cannot free himself from them.

- Albert Camus, *The Myth of Sisyphus and Other Essays*

Einstein famously proposed a quantized electromagnetic field to explain the photoelectric effect and received a Nobel Prize in physics in 1921 [13]. Glauber then used bosonic quantum field theory to develop the theory of the coherent state of light [14]. This development led to the proposal of various types of minimum uncertainty states [15] which was then followed by the proposal of a two-photon coherent state [16], which is now called a squeezed state. A few years later, methods to generate and detect squeezed states of light were introduced [17].

Due to the reduced noise property of squeezed light, it has been proposed to improve optical communication [18] and the sensitivity of optical interferometers [19]. After a period of nearly 40 years of development, LIGO incorporated squeezed light to measure gravitational waves from a merging black hole 1.3 billion light-years away [20]. Thus, Einstein's ideas on the quantum nature of light are now becoming an important part of this exciting journey to study the universe.

This chapter introduces the basic concepts of various quantum states of light and, in particular, the properties of squeezed light. After the basic concept, we briefly

introduce how to characterize the entanglement present in two-mode squeezed light, which will be further expanded in Ch. 7.

2.1 Quantum Description of Light

The Heisenberg uncertainty principle states that two conjugate variables, such as momentum and position, cannot be observed precisely at the same time. It shows that the product of the uncertainties of these two variables for a given state must satisfy

$$\langle (\Delta \hat{X})^2 \rangle \ \langle (\Delta \hat{Y})^2 \rangle \geq 1. \tag{2.1}$$

This kind of uncertainty relationship is also true for conjugate variables of electromagnetic (EM) waves, such as the amplitude and phase quadratures.

Let's consider an electromagnetic field of angular frequency ω confined in a cavity of volume of V, which makes it possible to write the field in quantized form as [21]

$$\hat{E}(t) = \frac{E_0}{2} \left(\hat{a} e^{-i\omega t} + \hat{a}^\dagger e^{i\omega t} \right), \tag{2.2}$$

where $E_0 = \sqrt{\hbar\omega/V}$, and $\hat{a}^\dagger$ and $\hat{a}$ are the annihilation and creation operators for the number of photons in the field. We can rewrite this expression as a real and an imaginary part that represent the in-phase and out-of-phase portion of the electric field, respectively, such that

$$\hat{E}(t) = E_0 \left(\hat{X} \cos\omega t + \hat{Y} \sin\omega t \right), \tag{2.3}$$

where $\hat{X}$ and $\hat{Y}$ are the imaginary and real parts of the complex amplitude of the field, such that $\hat{X} = (\hat{a}^\dagger + \hat{a})$ and $\hat{Y} = (\hat{a} - \hat{a}^\dagger)/i$. These quantities are also referred to

as the quadratures. Since the creation and annihilation operators follow the bosonic commutation relation of $[\hat{a}, \hat{a}^\dagger] = 1$, so it is easy to show that

$$[\hat{X}, \hat{Y}] = 2i. \tag{2.4}$$

As a result, the uncertainty relationship for the quadratures takes the form

$$\langle (\Delta \hat{X})^2 \rangle \langle (\Delta \hat{Y})^2 \rangle \geq 1. \tag{2.5}$$

The limit in which both quadratures have the same uncertainty and their product minimizes the uncertainty relation, $\langle (\Delta \hat{X})^2 \rangle = \langle (\Delta \hat{Y})^2 \rangle = 1$, is known as the quantum noise limit (QNL). In this thesis, the QNL refers only the shot noise of the light and does not consider other effects such as measurement back-action. The QNL represents the minimum noise level achievable with a classical source and is the result of randomly distributed photons over time.

2.1.1 Vacuum State

The intensity of electric field is proportional to the number of photons, which can be represented as a number state (also referred as a Fock state), $|n\rangle$, where n is the number of photons in the field. We can obtain the number of photons by applying the number operator $\hat{n} = \hat{a}^\dagger \hat{a}$, such that $\hat{n} |n\rangle = n |n\rangle$ which can be shown by using the properties of the lowering and raising operations $\hat{a} |n\rangle = \sqrt{n} |n-1\rangle$ and $\hat{a}^\dagger |n\rangle = \sqrt{n+1} |n+1\rangle$.

When we remove all photons from the field, such that we get $|0\rangle$, the state is called a vacuum state. In this case, the mean of the quadratures become zero, $\langle \hat{X} \rangle = 0$ and $\langle \hat{Y} \rangle = 0$, but the noise is equal to the QNL. This is a fairly interesting state. Even

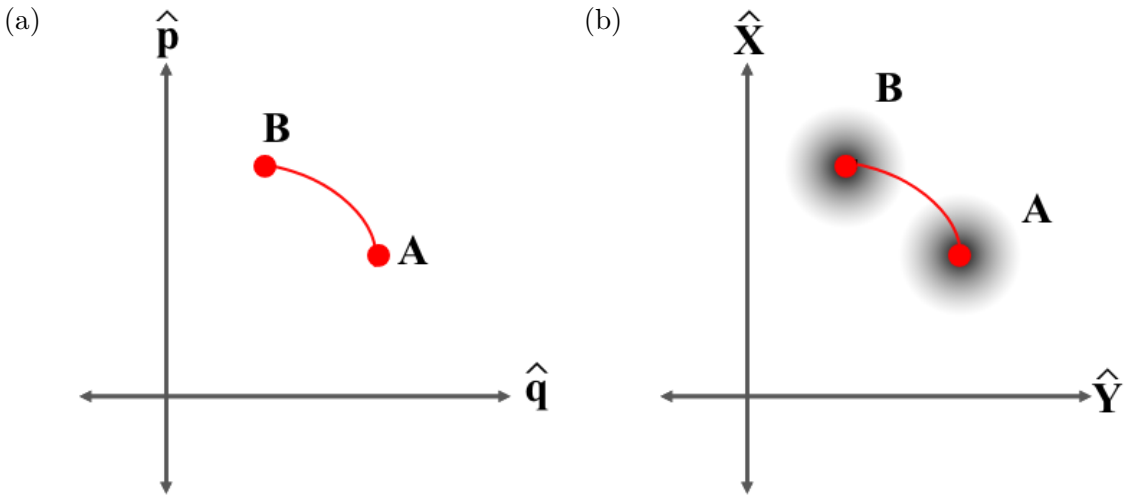

Figure 2.1: Phase-space representation of (a) the classical trajectory of a particle with respect to its position and momentum and (b) the quantum trajectory of the electric field with respect to the real and imaginary parts of the field from initial point A to final point B.

though there are no photons in the field for a vacuum state, the field still has noise. The effect of vacuum noise is important in quantum mechanics [22] and also the main effect we consider in this chapter.

2.1.2 Coherent States of Light

A coherent state is a vacuum state displaced in a phase-space diagram. Phase-space was introduced by Gibbs to represent the classical trajectory of a system with respect to its conjugate coordinates, such as position and momentum [23]. Figure 2.1(a) shows the classical trajectory of a particle from A to B with respect to its position and momentum.

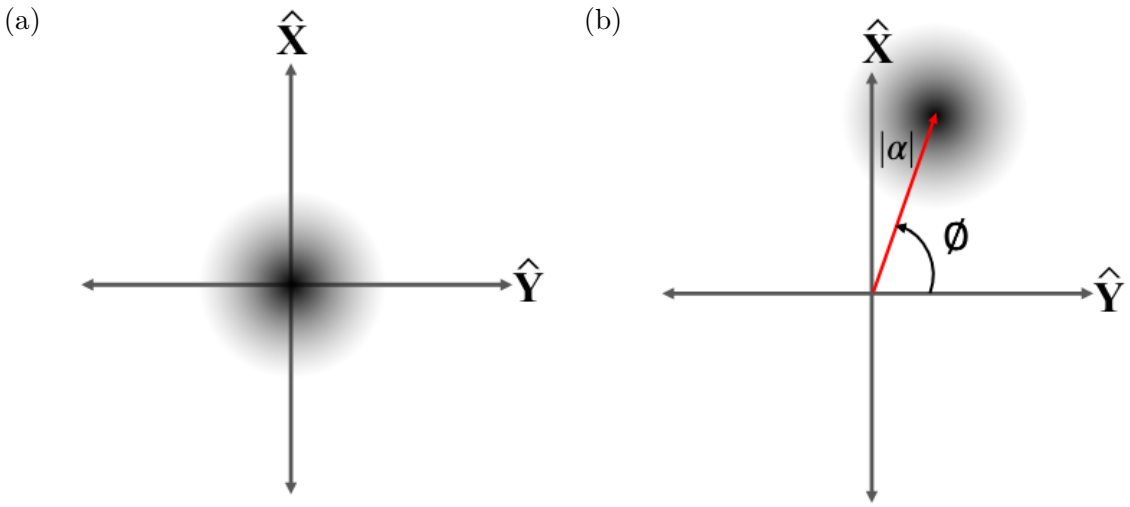

Figure 2.2: Phase-space representation of (a) a vacuum state and (b) a coherent state with a displacement amplitude of $|\alpha|$ and an angle of ϕ.

On the other hand, due to the uncertainty principle, we do not have exact information on the position and momentum of a particle. Therefore, a quantum mechanical system can be represented with a circular region indicating the QNL centered around the mean value on the phase-space diagram, such that the trajectory of the quantum system can be represented as shown in Fig. 2.1(b).

The coherent state of light, denoted as $|\alpha\rangle$, is defined as [14]:

$$|\alpha\rangle = \hat{D}(\alpha)\,|0\rangle = \exp(\alpha\hat{a}^{\dagger} + \alpha^{*}\hat{a})\,|0\rangle\,, \tag{2.6}$$

where $\hat{D}(\alpha)$ is the displacement operator, and $\alpha = |\alpha|\exp(i\phi)$ is its complex amplitude. Figures. 2.2(a) and (b) show phase-space diagram of a vacuum state and a coherent state, which is generated by applying the displacement operator to the vacuum state,

respectively.

By projecting the coherent state into a number state basis, which is composed of the eigenstates of the number operator $\hat{n}$, we can obtain the following expansion for a coherent state $|\alpha\rangle$:

$$|\alpha\rangle = \exp(-\frac{|\alpha|^2}{2}) \sum_{n=0}^{\infty} \frac{\alpha^n}{\sqrt{n!}} |n\rangle \,. \tag{2.7}$$

With this expression, we can get probability distribution of the number of photons in the coherent state to be of the form

$$P(n) = |\langle n|\alpha\rangle|^2 = \exp(-|\alpha|^2)\frac{|\alpha|^{2n}}{n!}, \tag{2.8}$$

which follows a Poissonian distribution. This provides physical insight into the statistics of this state. The Poisson distribution occurs when events are independent and random. For example, if we count the number of customers at a busy convenience store, it follows a Poissonian distribution, because the arrival times of customers are random and independent. Therefore, the coherent state of light is the quantum mechanical representation of classical light, as it comes from a classical source, such as a laser that exhibits a randomly and independently photon emission distribution.

This distribution has unique properties, such as having a the mean and variance of the number of photons are equal to each other and have a value with $|\alpha|^2$. This noise is called the shot noise, in analogy to the random noise that particles such as marbles in a bucket would make, if marbles poured out of the bucket, as they hit the ground. Therefore, the intensity noise, or photon number distribution of the coherent state is also called the shot noise [24].

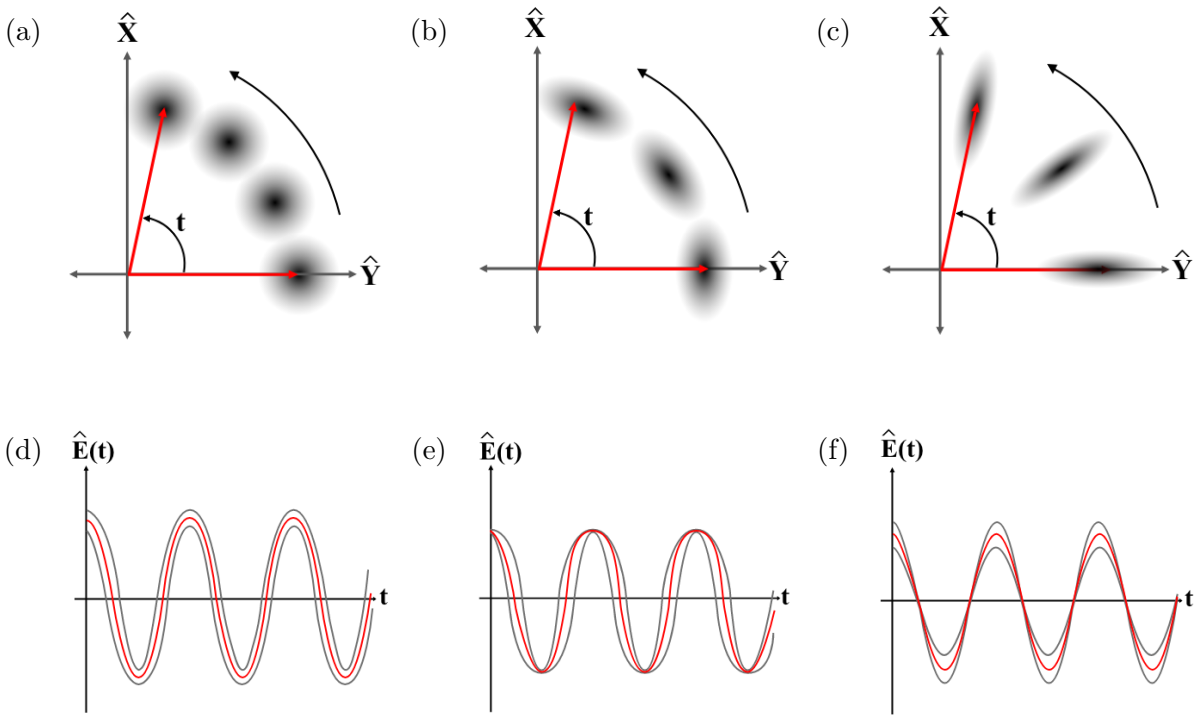

Figure 2.3: Phase-space diagram for the trajectory of (a) a coherent state (b) an amplitude squeezed state, and (c) a phase squeezed state with the corresponding electric field as a function of time for (d) the coherent light, (e) the amplitude squeezed state, and (f) the phase squeezed state. These diagrams were first introduced by Caves [19].

2.1.3 Squeezed States of Light

The phase-space distribution of the coherent state, shown in Fig. 2.3(a), shows that its variance is symmetric along both quadratures. A state in which the uncertainty of one of the quadratures is less than that of the coherent state is called a squeezed state of light. To satisfy the uncertainty principle, if one of the quadratures has less noise than the QNL, the noise of the conjugate quadrature must be noisier than the QNL.

As shown in Figs. 2.3(b) and (c), a squeezed state can be either an amplitude squeezed state or a phase squeezed state depending on the axis that has reduced noise.

If we look at the electromagnetic field as a function of time, for the coherent state, shown in Fig. 2.3(d), the noise in the phase and amplitude of the field is uniform over the entire oscillation period. On the other hand, the amplitude squeezed state has suppressed amplitude noise, as shown in Fig. 2.3(e). As a result, there is less noise at the peak of the electric field oscillation, but more noise at the zero crossing. Similarly, for the case of phase squeezing, shown in Fig. 2.3(f), the noise is greatest at the peak of the electric field oscillation, but smallest at the zero crossing [19].

The squeezed state can be generated with a unitary transformation of the vacuum state according to

$$|\alpha, \xi\rangle = \hat{D}(\alpha)\hat{S}(\xi)\,|0\rangle = \hat{D}(\alpha)\,\exp\left(\frac{1}{2}\xi^*\hat{a}^2 - \frac{1}{2}\xi\hat{a}^{\dagger 2}\right)|0\rangle\,, \tag{2.9}$$

where $\hat{S}(\xi)$ is the squeezing operator with $\xi = s\,\exp(i\theta)$, and s and θ represent the degree of squeezing and squeezing angle, respectively. We can see from the form of the squeezing operator that the simultaneous creation or annihilation of two photons squeezes the noise of the field in phase-space.

As shown in Fig. 2.4, the generation of a squeezed state according to Eq. (2.9) first applies the squeezing operator $\hat{S}(\xi)$ to a vacuum state to squeeze the noise in one direction. ξ determines the angle and amount of squeezing. The noise distribution of the squeezed vacuum is then displaced to obtain the final state $|\alpha, \xi\rangle$ with complex amplitude α.

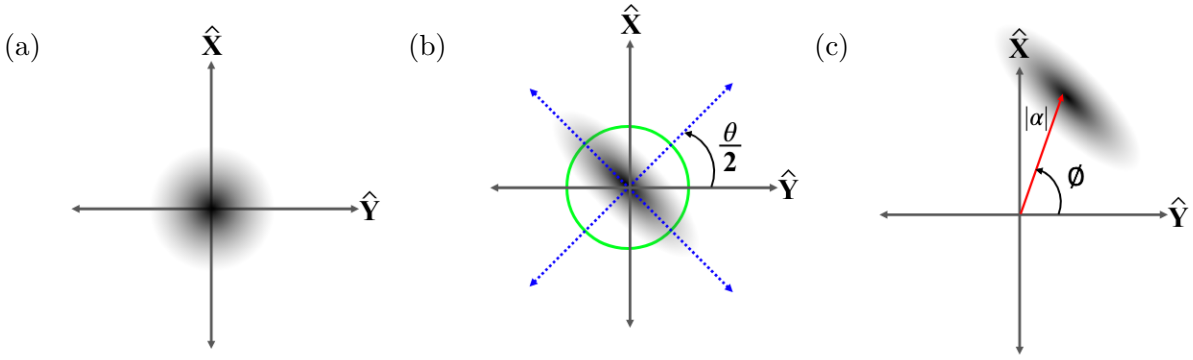

Figure 2.4: Generation of a displaced squeezed state. (a) Phase-space distribution of the initial vacuum state. (b) The squeezing operator transforms the vacuum state into a squeezed vacuum state with squeezing angle θ and level of squeezing s. (c) The squeezed vacuum is then displaced with phase ϕ and amplitude α. This figure is recreated from Ref. [25].

The annihilation and creation operators are transformed by the squeezing and displacement operator according to $\hat{S}^\dagger(\xi)\hat{a}\hat{S}(\xi) = \hat{a}\cosh s - \hat{a}^\dagger e^{i\theta}\sinh s$, $\hat{S}^\dagger(\xi)\hat{a}^\dagger\hat{S}(\xi) = \hat{a}^\dagger\cosh s - \hat{a}e^{-i\theta}\sinh s$, $\hat{D}^\dagger(\alpha)\hat{a}\hat{D}(\alpha) = \hat{a}+\alpha$, and $\hat{D}^\dagger(\alpha)\hat{a}^\dagger\hat{D}(\alpha) = \hat{a}^\dagger+\alpha^\star$, respectively. Taking advantage of these transformation and, assuming that the phases of the squeezing and displacement operators ϕ and θ are zero, the noise of each quadrature is given by,

$$\langle(\Delta\hat{X})^2\rangle = \exp(-2s) \quad \text{and} \quad \langle(\Delta\hat{Y})^2\rangle = \exp(2s). \tag{2.10}$$

We can see that the amplitude noise decreases below 1, which corresponds to the QNL, while the phase noise increases above 1.

2.2 Two-Mode Squeezed States of Light

Instead of generating two photons simultaneously into one optical mode as needed to generate single-mode squeezing, they can be generated in two different optical modes. The resulting state is called a two-mode squeezed state.

2.2.1 Properties of Two-Mode Squeezed States

Let's consider two different optical modes a and b. The two-mode squeezed state can be written as,

$$|\alpha, \beta, \xi\rangle = \hat{D}(\alpha)_a \hat{D}(\beta)_b \hat{S}_{ab}(\xi) \, |0,0\rangle = \hat{D}(\alpha)_a \hat{D}(\beta)_b \, \exp\left(\xi^* \hat{a}\hat{b} - \xi \hat{a}^\dagger \hat{b}^\dagger\right) |0,0\rangle \,, \quad (2.11)$$

where $\hat{a}$, $\hat{a}^\dagger$, $\hat{b}$, and $\hat{b}^\dagger$ are the corresponding annihilation and creation operators for each mode, $\hat{S}_{ab}(\xi) = \exp\left(\xi^* \hat{a}\hat{b} - \xi \hat{a}^\dagger \hat{b}^\dagger\right)$ is the two-mode squeezing operator with squeezing parameter $\xi = se^{i\theta}$, and $\alpha = |\alpha| e^{i\phi_a}$ and $\beta = |\beta| e^{i\phi_b}$ are the complex amplitudes of the displacement operations. The creation and annihilation operators are transformed by the two-mode squeezing operator as $\hat{S}^\dagger_{ab}(\xi) \hat{a} \hat{S}_{ab}(\xi) = \hat{a} \cosh s - \hat{b}^\dagger e^{i\theta} \sinh s$ and $\hat{S}^\dagger_{ab}(\xi) \hat{b} \hat{S}_{ab}(\xi) = \hat{b} \cosh s - \hat{a}^\dagger e^{i\theta} \sinh s$, respectively.

Unlike single-mode squeezing, there is no squeezing in each individual mode. As can be seen in Figs. 2.5(a) and (b), each mode actually has more noise than the QNL ($\langle (\Delta \hat{X}_a)^2 \rangle > 1$, $\langle (\Delta \hat{X}_b)^2 \rangle > 1$, $\langle (\Delta \hat{Y}_a)^2 \rangle > 1$, and $\langle (\Delta \hat{Y}_b)^2 \rangle > 1$) because active amplification leads to excess noise of the amplified beam with thermal statistics.

However, there are quantum correlations between the two modes. To observe these correlations, we define joint quadratures as follows:

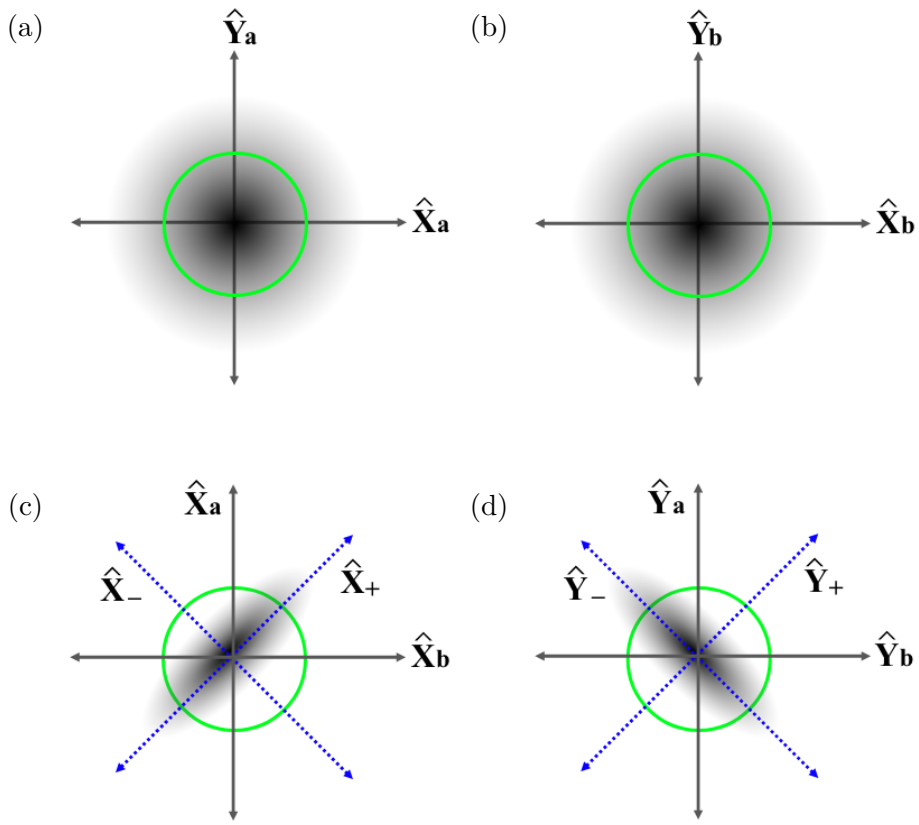

Figure 2.5: Phase-space distribution of two-mode squeeze state. The quadratures of (a) mode a and (b) mode b have more noise than a coherent state (green line), and the combined quadratures of (c) X_a and X_b, and (d) Y_a and Y_b indicate the noise reduction.

$$\hat{X_\pm} = (\hat{X_a} \pm \hat{X_b})/\sqrt{2} \quad \text{and} \quad \hat{Y_\pm} = (\hat{Y_a} \pm \hat{Y_b})/\sqrt{2}. \tag{2.12}$$

Assuming ϕ_a, ϕ_b and θ are zero, the noise of the joint quadrature is given by,

$$\langle(\Delta\hat{X_\pm})^2\rangle = \exp(\pm 2s) \quad \text{and} \quad \langle(\Delta\hat{Y_\pm})^2\rangle = \exp(\mp 2s), \tag{2.13}$$

This indicates that the combination of the quadratures of modes a and b can have

reduced noise properties as shown in Figs. 2.5(c) and (d).

2.2.2 Characterization of Entanglement

Quantum entanglement is a property of a system in which subsystems (two or more) cannot be described independently of each other. For example, if we consider two independent quantum systems, such as Alice and Bob, then the state of the combined system can be written as

$$|\psi\rangle_{ab} = |\psi\rangle_a \otimes |\psi\rangle_b \,, \tag{2.14}$$

where $|\psi\rangle_a$ and $|\psi\rangle_b$ are states in Hilbert space H_a and H_b, respectively. This state is called a separable state. If the state cannot be written as $|\psi\rangle_a \otimes |\psi\rangle_b$, then $|\psi\rangle_{ab}$ is called an inseparable state or an entangled state [26]. Therefore, by checking if a system is separable or not, we can verify it is entangled. There are several ways to characterize entanglement. One common method is the positive partial transposition (PPT) criteria, which provides a necessary condition to verify if a system is separable. We are interested in verifying entanglement between physical observables such as electromagnetic field quadratures. We can describe the system by constructing the covariance matrix (CM), σ, which can completely characterizes a system if it is in a Gaussian state. The CM is defined such that $\sigma = \left\langle \xi \xi^T \right\rangle$, where ξ represents the quadrature element vector $\xi = [\hat{X}_a, \hat{Y}_a, \hat{X}_b, \hat{Y}_b]$ and the elements of the CM are defined as $\left\langle \hat{X}_i \hat{X}_j \right\rangle = \left\langle \hat{X}_i \hat{X}_j + \hat{X}_j \hat{X}_i \right\rangle /2 - \left\langle \hat{X}_i \right\rangle \left\langle \hat{X}_j \right\rangle$.

Due to the uncertainty principle in Eq. (2.5), a physical CM must satisfy the in-

equality $\sigma + i\Omega \geq 0$ [27, 28], where the symplectic matrix Ω takes the form

$$\Omega = \bigoplus_{j=0}^{2} J, \quad J = \begin{pmatrix} 0 & -1 \\ 1 & 0 \end{pmatrix}. \tag{2.15}$$

For a Gaussian state, to check for entanglement based on the CM, the system must be tested to see if it is separable. This means that we need to see if it can be written as two independent subsystems, such that $\sigma = \sigma_1 \oplus \sigma_2$. The PPT criteria states that if

$$\widetilde{\sigma} + i\Omega \geq 0, \tag{2.16}$$

where $\widetilde{\sigma}$ is the partial transposed CM, then the system is separable. Physically, the partial transposition can be interpreted as a time reversal of the system in mode 1. If the total system is separable then the subsystems are independent of each other, which means that time reversal of one of the subsystem should not violate the uncertainty principle. However, if the partial transposition leads to a negative eigenvalue, which corresponds to an unphysical system, we can conclude that the system is inseparable.

For example, consider the CM for a two-mode squeezed state

$$\sigma_{TM} = \begin{pmatrix} \left\langle \hat{X}_a^2 \right\rangle & \left\langle \hat{X}_a \hat{Y}_a \right\rangle & \left\langle \hat{X}_a \hat{X}_b \right\rangle & \left\langle \hat{X}_a \hat{Y}_b \right\rangle \\ \left\langle \hat{Y}_a \hat{X}_a \right\rangle & \left\langle \hat{Y}_a^2 \right\rangle & \left\langle \hat{Y}_a \hat{X}_b \right\rangle & \left\langle \hat{Y}_a \hat{Y}_b \right\rangle \\ \left\langle \hat{X}_b \hat{X}_a \right\rangle & \left\langle \hat{X}_b \hat{Y}_a \right\rangle & \left\langle \hat{X}_b^2 \right\rangle & \left\langle \hat{X}_b \hat{Y}_b \right\rangle \\ \left\langle \hat{Y}_b \hat{X}_a \right\rangle & \left\langle \hat{Y}_b \hat{Y}_a \right\rangle & \left\langle \hat{Y}_b \hat{X}_b \right\rangle & \left\langle \hat{Y}_b^2 \right\rangle \end{pmatrix} \tag{2.17}$$

$$= \frac{1}{2} \begin{pmatrix} (e^{-2s} + e^{2s}) & 0 & (e^{2s} - e^{-2s}) & 0 \\ 0 & (e^{-2s} + e^{2s}) & 0 & (e^{-2s} - e^{2s}) \\ (e^{2s} - e^{-2s}) & 0 & (e^{-2s} + e^{2s}) & 0 \\ 0 & (e^{-2s} - e^{2s}) & 0 & (e^{-2s} + e^{2s}) \end{pmatrix}. \tag{2.18}$$

For a pure state, the PPT criteria can be conveniently restated as $\Delta \equiv -(\widetilde{\Omega}\sigma)^2 \geq 1$ [28], where Δ can be written as

$$\Delta = - \begin{pmatrix} \cosh(4s) & 0 & \sinh(4s) & 0 \\ 0 & \cosh(4s) & 0 & -\sinh(4s) \\ \sinh(4s) & 0 & \cosh(4s) & 0 \\ 0 & -\sinh(4s) & 0 & \cosh(4s) \end{pmatrix}, \tag{2.19}$$

with the smallest eigenvalue of Δ equal to e^{-4s}. Therefore, we have that the eigenvalue of $\Delta < 1$ for $s > 0$ and can conclude that a pure two-mode squeezed state is always inseparable. A stronger violation indicates a stronger degree of entanglement. Thus, we can use PPT criteria to characterize the entanglement in a two-mode squeezed state of light [29].

2.3 Conclusion

In this chapter, we explain the QNL of light and discuss how to characterize squeezed light and its noise properties in terms of entanglement. We introduce the displacement operator a squeezing operators to show coherent and squeezed states of light. From two-mode squeezed light, we further discuss a method to characterize the entanglement.

The following chapter describes different methods for generating squeezed light in two modes and measuring its noise property. In Ch. 7, we will expand from a two-mode squeezed state of light to a multipartite Gaussian entangled state, and show how to characterize entanglement using the PPT criteria.

Chapter 3

Generation of Squeezed States of Light

"Let's go." "We can't." "Why not?" "We're waiting for Godot."

- Samuel Beckett, *Waiting for Godot 221*

In Eq. (2.9), we can see that two-photon emission is required to produce squeezed light, which is only possible through a material's nonlinear response. The first signature of squeezed light was demonstrated with a third order nonlinear process called four-wave mixing (FWM). The FWM process was first introduced by Yariv and Pepper from Caltech in 1977 [30]. Using two non-depleting pump waves inside of a nonlinear medium, they show that the FWM process can control the transmission and phase of reflections. Two years later, Yuen and Shapiro from MIT theoretically proposed that squeezed light could be generated with a FWM source via two-photon emission [31].

At the AT&T lab in 1985, Slusher and his colleagues for the first time obtained squeezed light using FWM via a sodium beam in a cavity [32]. As absorption and spontaneous emission decrease the amount of correlation and squeezing, their work relied on off-resonance operation to avoid those effects. Only -3 dB of squeezing could be obtained. To improve the amount of squeezing, Shahriar and Hemmer from MIT proposed a new scheme [33]. They proposed to use the atomic coherence of two ground states in a lambda configuration. Ten years later at NIST, a large amount of squeezing was measured with FWM by McCormick, Marino, Boyer, and Lett [34]. This approach

based on atomic coherence in Rubidium atoms showed a squeezing level of -8 dB and later improved to -9.2 dB [35].

This chapter describes the properties of the required nonlinear medium to produce squeezed light, and in particular the FWM process. We then introduce the necessary noise measurements and calculations for two-mode squeezed light to take into account the effect of losses.

3.1 Generation of Squeezed Light

In optics we generally only consider the linear response of the medium, which is proportional to the electric field, such that

$$\mathbf{P}(\mathbf{r},t) = \epsilon_0 \chi^{(1)} \mathbf{E}(\mathbf{r},t), \tag{3.1}$$

where $\mathbf{P}(\mathbf{r},t)$ is the polarization of the medium, $\mathbf{E}(\mathbf{r},t)$ is the applied electric field that depends on time t and medium coordinate $\mathbf{r}$, ϵ_0 is the vacuum permittivity, and $\chi^{(1)}$ is the linear response of the material. After lasers were invented, strong fields could be used to modify the optical properties of a medium, which requires expressing $\mathbf{P}(\mathbf{r},t)$ as a power series expansion in terms of fields [36], such that

$$\begin{aligned} \mathbf{P}(\mathbf{r},t) &= \mathbf{P}^{(1)}(\mathbf{r},t) + \mathbf{P}^{(2)}(\mathbf{r},t) + \mathbf{P}^{(3)}(\mathbf{r},t) + \mathbf{P}^{(4)}(\mathbf{r},t) + ... \\ &= \epsilon_0 \left[\chi^{(1)} \mathbf{E}(\mathbf{r},t) + \chi^{(2)} \mathbf{E}^2(\mathbf{r},t) + \chi^{(3)} \mathbf{E}^3(\mathbf{r},t) + \chi^{(4)} \mathbf{E}^4(\mathbf{r},t) + ... \right], \end{aligned} \tag{3.2}$$

where $\chi^{(n)}$ is the n^{th} order susceptibility of the medium. Higher-order susceptibility allows for multi-photon interactions, such that the nonlinear response of the medium can be used to generate new fields or fields with different frequencies.

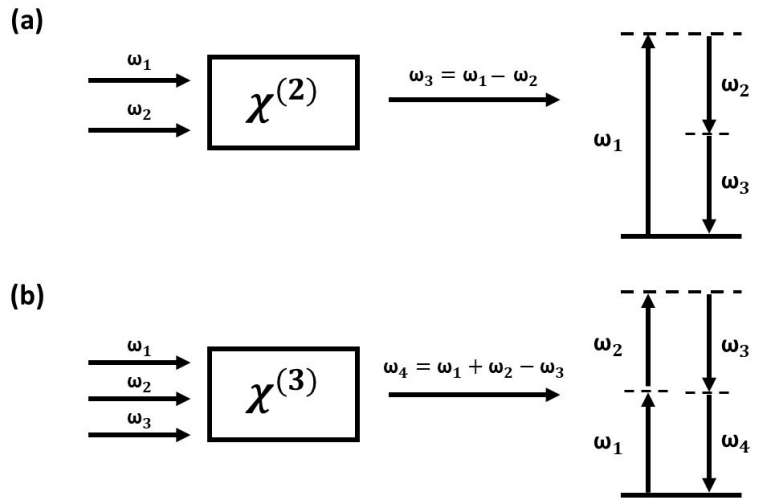

Figure 3.1: Two examples of wave mixing inside a nonlinear medium: (a) frequency difference generation in a medium with a second order susceptibility and (b) FWM in a medium with a third order susceptibility.

The wave equation for the **E** field in a medium is of the form:

$$\nabla^2\mathbf{E} - \frac{1}{c^2}\frac{\partial^2\mathbf{E}}{\partial t^2} = \frac{1}{\epsilon_0 c^2}\frac{\partial^2\mathbf{P}}{\partial t^2}, \tag{3.3}$$

where c is speed of light in vacuum. By splitting the polarization into first order and higher order responses, $\mathbf{P} = \mathbf{P}^{(1)} + \mathbf{P}^{NL}$, and assuming that the medium is isotropic and dispersionless, the wave equation can be written as:

$$\nabla^2\mathbf{E} - \frac{n^2}{c^2}\frac{\partial^2\mathbf{E}}{\partial t^2} = \frac{1}{\epsilon_0 c^2}\frac{\partial^2\mathbf{P}^{NL}}{\partial t^2}, \tag{3.4}$$

where n is the linear refractive index of the medium.

Let's consider the simple case of a medium with a second-order susceptibility ($\chi^{(2)}$), such as a nonlinear crystal. If we ignore the position dependence of the electric field, the most general form of the input electric field to illustrate all possible processes is

given by,

$$\mathbf{E}(t) = E_1 e^{-i\omega_1 t} + E_2 e^{-i\omega_2 t} + c.c., \tag{3.5}$$

where ω_1 and ω_2 are the angular frequencies of the electric fields with amplitudes E_1 and E_2. The response of the medium take the form:

$$\begin{aligned}
\mathbf{P}^{(2)}(t) &= \epsilon_0 \chi^{(2)} \mathbf{E}(t)^2 \\
&= \epsilon_0 \chi^{(2)} \Big[E_1^2 e^{-2i\omega_1 t} + E_2^2 e^{-2i\omega_2 t} + 2\ E_1 E_2 e^{-i(\omega_1+\omega_2)t} \\
&+ 2\ E_1 E_2^* e^{-i(\omega_1-\omega_2)t} + c.c \Big] + \epsilon_0 \chi^{(2)} \big[E_1 E_1^* + E_2^* E_2 \big].
\end{aligned} \tag{3.6}$$

As can be seen from Eq. (3.6), various frequency components exist due to the nonlinear interaction between the field and the medium. All terms have a physical meaning in terms of specific processes. For example, as light propagates through the $\chi^{(2)}$ medium, the frequency of the input field can be doubled (second harmonic generation), combined (sum frequency generation), subtracted (difference frequency generation), or cancel to generate a DC term (electro-optic effect) as shown in Eq. (3.6).

The specific case shown in Fig. 3.1(a), in which the nonlinear interaction generates a new photon with frequency $\omega_3 = \omega_1 - \omega_2$ is called difference frequency generation. According to the energy level diagram, the nonlinear medium first absorbs a photon at frequency ω_1 and is excited to a higher energy level. A seed photon at frequency ω_2 stimulates the nonlinear process. This leads to the stimulated emission of a two-photon process involving the emission of two photons at frequencies ω_2 and ω_3. This difference frequency generation process is also known as parametric down conversion, and it does not need to be stimulated with a seed at ω_2, as it can grow from spontaneous emission.

In this case, the process is called spontaneous parametric down conversion. As this process generates pairs of photons, it can be used to produce squeezed light. It can be implemented with a nonlinear crystal with a large second order susceptibility, such as PPKTP (periodically poled potassium titanyl phosphate) ot BBO (beta barium borate).

Unlike crystals, an atomic medium has inversion symmetry. This symmetry removes all even terms of the susceptibility $\chi^{(2n)}$. Therefore, the generation of squeezed light with an atomic ensemble is only possible through a $\chi^{(3)}$ or higher odd response. For generation of squeezed light, we are interested in the FWM process as the one shown in Fig. 3.1(b). Here, three photons produce a fourth photon with a new frequency determined by the frequency of the other three photons. Similar to the $\chi^{(2)}$ process, the atom is excited to a higher energy level via a two-photon process (absorption of photons at frequencies ω_1 and ω_2) and undergoes a stimulated decay with the emission of two photons at frequencies ω_3 and ω_4. The generated photons with frequencies ω_3 and ω_4 are quantum correlated due to their generation in pairs.

3.2 Four-Wave Mixing

In Fig. 3.2 we show the approach we use for the generation of two-mode squeezed light with a non-degenerate FWM process in the D1 line of ^{85}Rb vapor. Figure 3.2(a) show the FWM in the double-lambda configuration. In this configuration, the process relies on the two hyperfine levels to complete the parametric process. The initial proposal

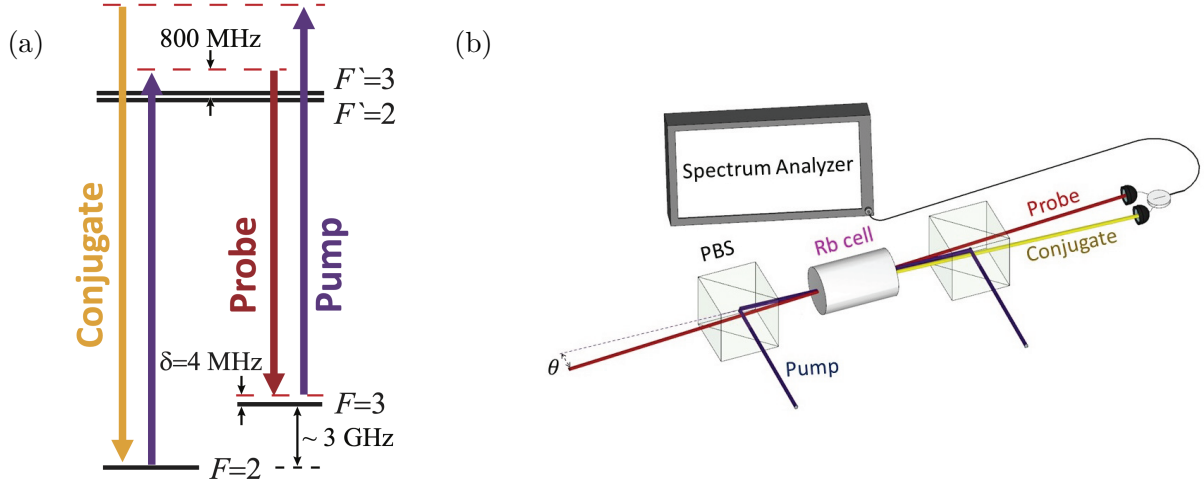

Figure 3.2: (a) Energy level diagram for the non-degenerate FWM configuration in a double-lambda system in the D1 line of ^{85}Rb. Two pump photons interact with the atomic ensemble, such that an input probe stimulates the $\chi^{(3)}$ process, which generates a pairs of photons, probe and conjugate. (b) Experimental setup for the FWM process. Orthogonally polarized probe and pump beams propagate through the rubidium vapor cell. As a result of the FWM process probe and conjugate are generated. Photodiodes measure the intensity, and resulting photocurrents are subtracted. The noise in the difference signal is then measured with a spectrum analyzer.

on double-lambda configuration [37] suggests operating the process on resonance to leverage the atomic coherence. In the resonant double-lambda configuration, two Raman processes can drive the medium and create a perfect transparent window, which reverses the absorption from an atomic medium. In theory, this can create an efficient nonlinear amplification to create squeezed light; however, the optimum configuration of the FWM process requires a high vapor pressure, and since EIT is dominated by

strong absorption even with higher atomic coherence [38], it is experimentally difficult to generate a large degree of squeezing.

Therefore, the later experiment operates the FWM in the double-lambda configuration operating off-resonance with the atomic transition without using EIT from strong atomic coherence [39]. In this process in Fig. 3.2(b), two photons from a single pump beam are converted into a pair of photons that we call probe and conjugate. This leads to the amplification of the input probe beam and the creation of the conjugate inside of the rubidium vapor cell. The reverse process can also occur, such that two photons, one from the probe and one from the conjugate, are absorbed, and two pump photons are emitted simultaneously.

3.2.1 Phase Matching Condition

We can see how the field evolves as they propagate through the medium by considering the response of the FWM process, $\mathbf{P}^{\mathrm{FWM}}(\mathbf{r},t)$, in the wave equation shown in Eq. (3.3) and writing the electric field components as $\mathbf{E}(\mathbf{r},t) = \mathbf{A}(\mathbf{r},t)e^{-i\mathbf{k}\cdot\mathbf{r}-wt}$, where $\mathbf{A}(\mathbf{r},t)$ is the slowly-varying amplitude of the field. For a FWM process $\mathbf{P}^{\mathrm{FWM}}(\mathbf{r},t)$ is given by:

$$\mathbf{P}^{\mathrm{FWM}}(\mathbf{r},t) \propto \chi^{(3)}\mathbf{A}_1\mathbf{A}_2\mathbf{A}_3^* e^{-i(\mathbf{k_1}+\mathbf{k_2}-\mathbf{k_3})\cdot\mathbf{z}}, \tag{3.7}$$

where $\mathbf{k}$ is the wavevector of the corresponding field. In the case of the FWM shown in Fig. 3.2(a), we can calculate the propagation equation for the conjugate mode as

$$\frac{\partial}{\partial z}\mathbf{A}_{conj} \propto i\chi^{(3)}\mathbf{A}_{pump}^2\mathbf{A}_{prob}^* e^{i\Delta\mathbf{k}\cdot\mathbf{z}}, \tag{3.8}$$

where $\Delta\mathbf{k}$ is the phase-matching condition which shows the relation between the momentum components of the four field wavevectors, such that $\Delta\mathbf{k} = 2\mathbf{k}_{pump} - (\mathbf{k}_{prob} + \mathbf{k}_{conj})$.

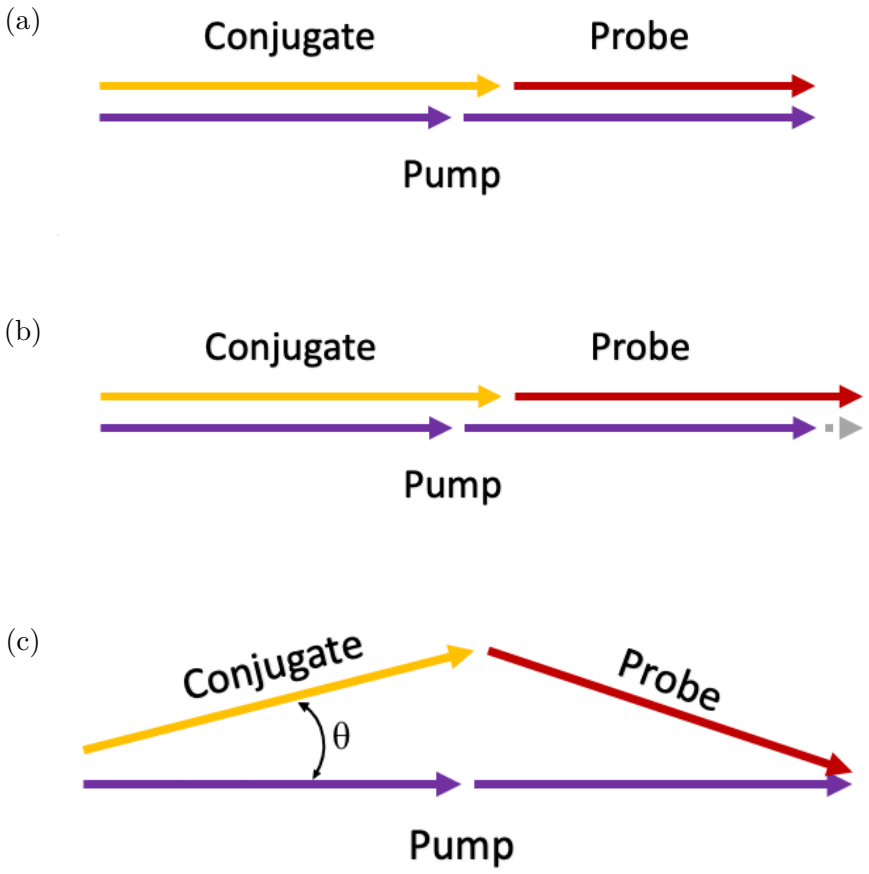

Figure 3.3: Phase-matching condition in (a) free space, (b) in a dispersive medium, and (c) when tuning the angle between the beams to compensate for the dispersive medium.

When the phase matching condition is not satisfied, $\Delta\mathbf{k} \neq 0$, the mismatch can limit the efficiency of the FWM process. Without phase matching, destructive interference

between beams leads low conversion efficiency. Efficient FWM occurs when $\Delta\mathbf{k} = 0$. In free space, this means that the four beams co-propagate together as shown in Fig. 3.3(a). However, in a dispersive medium, the refractive index changes with the frequency of light. This leads to a change of the wavevector according to $k = n(\omega)\omega/c$. In our non-degenerate FWM process, the dispersive medium has a dominant influence on the wavevector of probe beam as shown in Fig. 3.3(b), as it is close to a resonant transition in rubidium. This leads the phase matching condition in terms of wavevectors in vacuum, such that [38]

$$2\mathbf{k}_{pump}^{vac} - (n_{prob}\mathbf{k}_{prob}^{vac} + \mathbf{k}_{conj}^{vac}) = 0, \tag{3.9}$$

where n_{prob} is the refractive index of the medium at the probe frequency. By setting the direction of the $\mathbf{k}$ vector of the two pump beams in the z-direction, we get the phase matching condition with the angle between the pump and probe beams θ, $2k_{pump} - (n_{prob}k_{prob}cos(\theta) + k_{conj}cos(-\theta)) = 0$. This causes the correlated photon to be generated in two spatially different modes with an angle as shown in Fig. 3.3(c).

3.2.2 Atomic Density

Another important parameters of the FWM is the atomic density, $\mathcal{N}$. Since the susceptibility is proportional to the atomic density, $\chi \propto \mathcal{N}$, and index of refraction depends on susceptibility, atomic density can contribute to the efficiency of the FWM through phase matching condition given in Eq. (3.10) and the strength of the process in according to Eq. (3.8).

In the actual experiment, the atomic density can be controlled by the temperature of the rubidium vapor cell [40]. The optimum temperature for the FWM in a 2.54 cm long cell is about 110°C which corresponding to 10^{-4} torr with an angle of 0.5° between the probe and the pump fields. Increasing the temperature usually helps to increase the gain of the FWM process, but it also increases the vapor pressure, which causes more interatomic collisions and may activate other higher order nonlinear process in rubidium vapor. These unwanted effects compete with the FWM process to reduce the efficiency of the FWM process.

Additionally, since the probe transition is close to the the D1 $F = 3$ to $F' = 3$ transition, the width of the absorption transition starts to widen with increasing temperature, which results in additional losses of probe photons. This will lead to loss of squeezing, which we will discuss at the end of this chapter. Therefore, while it is important to increase the FWM gain, it is necessary to find the optimal gain by minimizing the losses due to absorption and competition with other nonlinear processes.

3.2.3 Energy Level

As the FWM converts two pump photons into a probe and a conjugate photon in double-lambda system, energy conservation leads the frequencies of the photons in the process to follow the relationship

$$2\omega_{pump} = \omega_{prob} + \omega_{conj}. \tag{3.10}$$

Ideally, it would be beneficial to operate the FWM on resonance with the probe beam resonant with the $F = 2$ to $F' = 2$ transition of ^{85}Rb to have an efficient FWM process. However, strong absorption dominates the process, so it is necessary to detune the process to reduce absorption.

We define two different types of detuning called one-photon and two-photon detuning. The one-photon detuning is defined with respect to the pump beam as $\Delta = \omega_{probe} - \omega_{33}$ and the two-photon detuning as $\delta = \omega_{23} - \omega_{prob} + \omega_{conj}$, where ω_{33} is the transition frequency between energy levels $F = 3$ to $F' = 3$ and ω_{23} is the ground state frequency difference between the hyperfine energy levels $F = 2$ and $F = 3$.

On the one-photon resonance ($\Delta = 0$), unwanted effects such as absorption and spontaneous emission dominate the FWM process. Since the effect of the $\chi^{(3)}$ nonlinearity has a wider bandwidth than the $\chi^{(1)}$ linear response [38], we can adjust the one-photon detuning to reduce the unwanted effects. We found the best one-photon detuning to be $\Delta = 800$ MHz. On the other hand, on the two-photon resonance, we also do not obtain the optimal FWM process due to the light shift introduced by the pump field. Therefore, the light shift must also be compensated for by changing the two-photon detuning to be slightly away from the two-photon resonance $\delta = 0$ to increase the efficiency of the FWM process.

3.3 Intensity Difference Measurement of Two-Mode Squeezed Light

The quantum correlations in two-mode squeezed light can be characterized by many detection techniques. The simplest way to measure them by directly looking at the intensity difference of the two modes. The probe and the conjugate can be detected with photodiodes to measure their intensities. The intensity measurements provide information about the number of photons and the fluctuations in the number of photons. Theoretically, to calculate the mean and the variance of the number of photons, we need to consider the number operator $\hat{n}$.

If we only seed the probe field and not the conjugate field, the average value of the intensities of the output fields can be calculated by using Eq. (2.11) for the two-mode squeezed state, such that [25]

$$\begin{aligned} \langle \hat{n}_a \rangle &= |\alpha|^2 \mathrm{cosh(s)}^2 = |\alpha|^2 G, \\ \langle \hat{n}_b \rangle &= |\alpha|^2 \mathrm{sinh(s)}^2 = |\alpha|^2 (G-1), \end{aligned} \tag{3.11}$$

where modes a and b are optical modes associated with probe and conjugate, respectively, α ($|\alpha|^2 >> 1$) is the displacement amplitude of the seed probe. Since the conjugate is not seeded ($|\beta| = 0$), and G is the gain of the FWM, defined as $G = \cosh^2(s)$.

The gain of the FWM is related to the amount of squeezing. To see this, we first

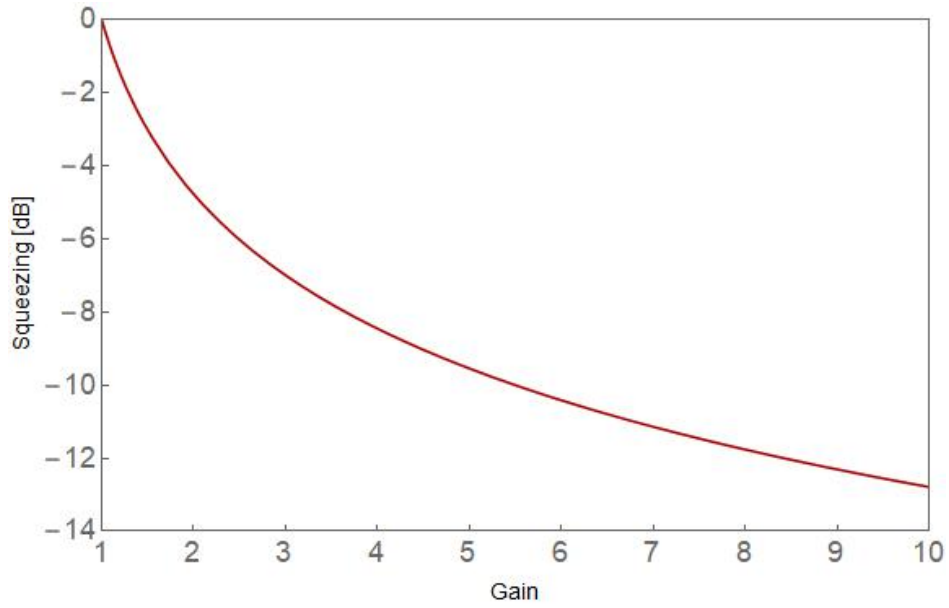

Figure 3.4: Theoretical calculation of the ideal intensity difference squeezing after the FWM process as a function of the gain.

calculate the variances of the output fields, which can be shown to be

$$\begin{aligned} \langle(\Delta\hat{n}_a)^2\rangle &= |\alpha|^2 G(2G-1) \\ \langle(\Delta\hat{n}_a)^2\rangle &= |\alpha|^2 (G-1)(2G-1). \end{aligned} \tag{3.12}$$

and the noise of the difference signal, $\langle\Delta(\hat{n_a} - \hat{n_b})^2\rangle = \langle(\Delta\hat{n_a})^2\rangle + \langle(\Delta\hat{n_b})^2\rangle - 2(\langle\hat{n_a}\hat{n_b}\rangle - \langle\hat{n_a}\rangle\langle\hat{n_b}\rangle)$, which is given by $\langle\Delta(\hat{n}_a - \hat{n}_b)^2\rangle = |\alpha|^2$. This shows that the noise of the difference signal after the FWM is equal to the noise of the input probe field. The correlations between the generated photon pairs is such that they have the same noise properties, so that subtracting the two generated signals results in only the initial input noise of the probe beam remaining.

To measure the squeezing of the output beams, we need to compare the noise to the one of coherent light at the same power level. If we define R_{FWM} as the noise ratio

between the output of the FWM and the coherent light with the same total power level, then we can show that it takes the form:

$$R_{\mathrm{FWM}} = \frac{\langle \Delta(\hat{n}_a - \hat{n}_b)^2 \rangle}{\langle \hat{n}_a \rangle + \langle \hat{n}_b \rangle} = \frac{1}{2G - 1}. \tag{3.13}$$

If $R_{\mathrm{FWM}} < 1$, we can conclude that there are quantum correlations between the two beams as characterized by intensity difference noise below the shot noise limit. Figure 3.4 shows the intensity difference squeezing as a function of the gain of the FWM process. It shows that as we increase the gain of the FWM process, the squeezing increases. However in the actual implementation of the FWM process, the probe has more losses than the conjugates because it is closer to resonance. This imbalance in losses limits the amount of squeezing that can be obtained as the gain increases. As a result, a physical system always has an optimum FWM gain, as we discussed in the next section.

We want to note that we used this intensity difference measurement technique for all the experiments in this thesis. However, this technique does not allow us measuring individual quadratures such as amplitude or phase, as would be needed to measure entanglement. To do that, we need another detection technique called homodyne detection. This technique makes it possible to extract information of the amplitude and the phase of the light by interfering the beam to be measured with a reference beam. Using this technique, we can measure the covariance between the modes to construct the covariance matrix.

3.4 Effect of Losses on Two-Mode Squeezed Light

The effect of losses can be modeled as a beam splitter (BS) operation with power transmission η and reflection $1-\eta$ as follows [41],

$$\hat{a} \rightarrow \sqrt{\eta_a}\,\hat{a} + \sqrt{1-\eta_a}\,\hat{a}_v \quad \hat{b} \rightarrow \sqrt{\eta_b}\,\hat{b} + \sqrt{1-\eta_b}\,\hat{b}_v \tag{3.14}$$

where η_a and η_b are the transmissions for mode a and b, respectively, and $\hat{a}_v$ and $\hat{b}_v$ are the vacuum modes coupled via the BS operation. This transformation can be used to derive the effect of the loss on two-mode squeezed light.

Under the same assumption of only seeding the probe mode ($|\beta| = 0$ and $|\alpha|^2 >> 1$) and taking into account the effect of losses, the ratio of the noise of the twin beams to the noise of the corresponding coherent state can be shown to be [25]

$$R_{\text{FWM+Loss}} = 1 + \frac{2\eta_a^2 G(G-1) + 2\eta_b^2 (G-1)^2 - 4\eta_a\eta_b G(G-1)}{\eta_a G + \eta_b (G-1)}. \tag{3.15}$$

Figure 3.5 shows the effect of imbalanced losses of the twin beams. By fixing $\eta_b = 1$, we can see that we need some loss in the probe beam to maximize the squeezing. However, if we have imbalance loss, squeezing decrease as we increase the gain of the FWM process. For the same loss in both twin beams $\eta = \eta_b = \eta_a$, the equation can be simplified to,

$$R_{\text{FWM+Loss}} = \eta \frac{1}{2G-1} + (1-\eta) = \eta R_{\text{FWM}} + (1-\eta). \tag{3.16}$$

In this equation, we can see that squeezing decrease with losses, and in the limit of large loss, the noise reaches the QNL. However, squeezing is always observed regardless of the level of loss [42].

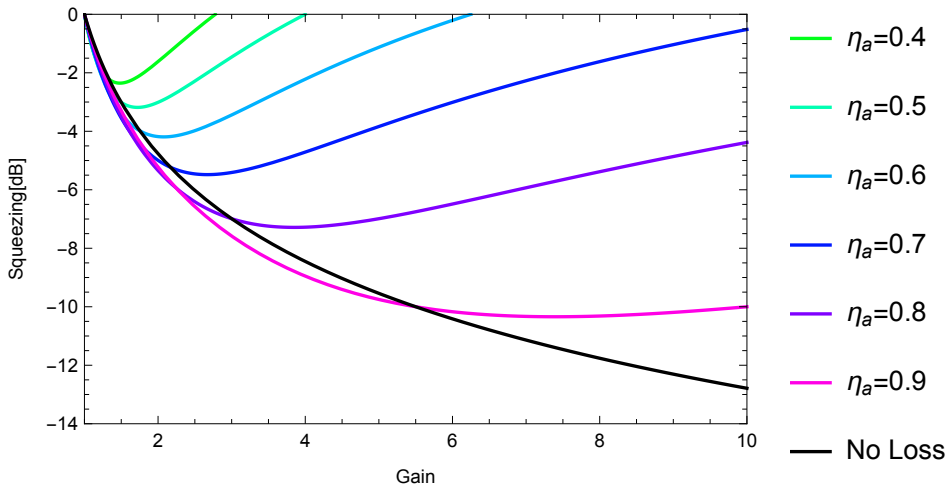

Figure 3.5: Theoretical calculation of the ideal intensity difference squeezing after the FWM process as a function of the gain. With an imbalance in losses, we can see that the squeezing decreases as the FWM gain increases.

3.5 Experimental Setup

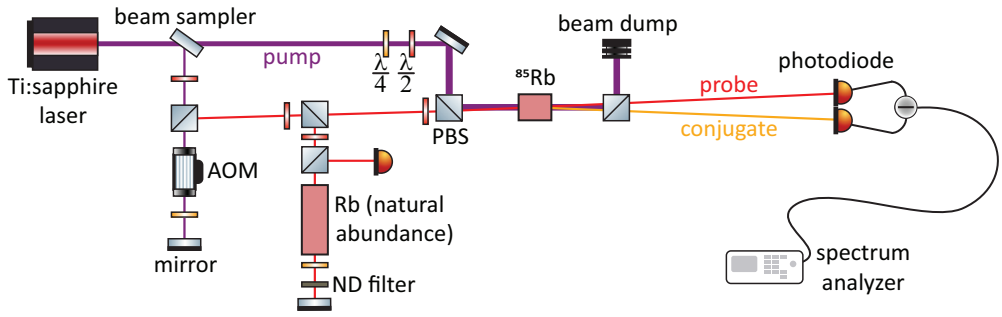

Figure 3.6: Simplified schematic of the experimental setup. AOM: acousto-optic modulator, ND filter: neutral density filter, PBS: polarizing beam splitter. Copyright (2018) by Optica Publishing Group. Reprinted with permission [12].

In the experiment, we used a non-degenerate FWM process in a double-lambda configuration on the D1 line of ^{85}Rb as shown in Fig. 3.2(a). We generate near-atomic

resonant squeezed light with an intensity difference squeezing of −9 dB, as shown in Fig. 3.7. In this configuration, the probe and conjugate are approximately 800 MHz and 3.8 GHz blue detuned from their respective transitions in the D1 line of ^{85}Rb. We have used a $1/e^2$ diameter for the pump and the probe of 1.0 mm and 0.7 mm, respectively, angle θ of 0.5°, pump power of ≈550 mW, and a two-photon detuning δ of 5 MHz [43].

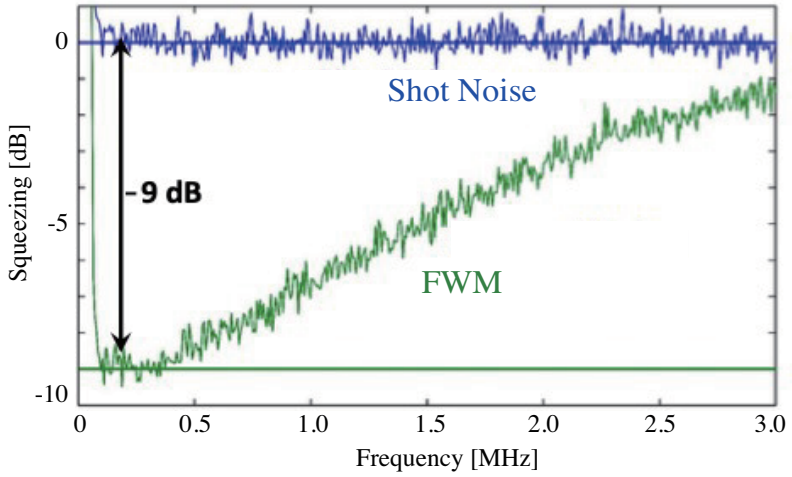

Figure 3.7: Intensity difference squeezing spectra. The blue trace shows the shot noise limit while the green trace shows the intensity difference squeezing. For these measurements the electronic noise has been subtracted and the spectrum analyzer was set to a resolution bandwidth of 30 kHz and a video bandwidth of 100 Hz.

The experimental setup is shown in Fig. 3.6. A continuous wave (CW) Ti:Sapphire laser is used to generate the pump beam required for the FWM. To generate the probe beam, a beam sampler is used to select a small portion of the pump before the Rb cell which is double-passed this beam through an acousto-optical modulator

(AOM) to generate the required frequency for the probe. Both the pump and probe are transmitted through single-mode optical fibers to clean up their spatial modes. After the fibers, the perpendicularly polarized pump and probe beams intersect at the center of a 25.4 mm ^{85}Rb vapor cell that has anti-reflection coated windows. After the FWM process, the pump beam is blocked with a polarizing filter and the probe and conjugate beam are measured using a balanced detecter with 95% quantum efficiency photodiodes. With this setup, we generate squeezed light 800 MHz away from the rubidium resonance.

3.6 Conclusion

In this chapter, we discussed the generation of squeezed light and the required properties of the nonlinear medium used to generate the light. To generate squeezed light, a nonlinear medium must generate two photons at the same time. We introduced the second-order nonlinearity in a crystal and the third-order nonlinearity in an atomic system. We then discussed the FWM process in an atomic source to generate of two-mode squeezed light. We show that efficient FWM requires the phase-matching condition to be fulfilled and optimum gain, which is determined by the angle of the probe and the pump beams, temperature of the rubidium vapor, and laser detuning. We also calculated the effect of losses and noise characteristics of the squeezed light, and found that imbalanced losses of the twin beams generally decrease the amount of squeezing as the gain increases that it can be optimized to improve the squeezing for a specific

gain.

In the next chapter, we will further discuss the generation of squeezed light with the FWM process and show how to generate atomic resonant squeezed light with the FWM process in a double-lambda configuration. We will revisit some of the noise characterization to justify our squeezing measurements and discuss the limitations of our approach.

Chapter 4

Generation of Resonant Two-Mode Squeezed States of Light

Boredom is the root of all evil - the despairing refusal to be oneself.

- Søren Kierkegaard , *Either/Or*

We have discussed the basic concepts of squeezed state of lights in last two chapters. Since it was first generated, squeezed light has received substantial attention for exhibiting reduced noise properties below the QNL. This can be used to improve the sensitivity of optical sensors such as fiber sensors [44], plasmonic sensor [45], and interferometers such as LIGO [20, 46]; enhance the security of protocols for quantum communication [47, 48, 49]; and improve imaging resolution [8, 50]. More recently, squeezed states of light have been proposed to realize one-way quantum computing [9, 51, 52].

The ability to enhance optical devices with squeezed light can be extended to devices based on atomic systems. Realizing an efficient interaction between atomic ensembles and squeezed light is necessary to take advantages of both systems for quantum sensors based on atoms and light. For example, previous studies have suggested and experimentally demonstrated that resonant squeezed light can enhance the sensitivity of atomic interferometers [53, 54], atomic magnetometers [11, 55], and atomic clocks [56].

In addition to the enhancements to atomic sensors, interactions between nonclassical light and atomic ensembles allow a way to store quantum information in atomic ensembles. Theoretical studies have shown that EIT preserves the quantum properties

of squeezed light [57, 58] and can be used to implement a quantum memory [59, 60]. Furthermore, the ability to generate quantum states of light on atomic resonance opens the possibility of deterministically transferring the entanglement from the light to two remote atomic ensembles and of generating entangled atom laser beams [61].

4.1 Previous Work

The enhancements of an atomic sensor using squeezed light requires efficient interactions between atomic ensembles and squeezed light which requires the light to be narrowband and on atomic resonance. Therefore, there have been many approaches for generating atomic resonant squeezed light. However, generating resonant squeezed light has proven to be challenging. For example, a common way to generate squeezed light is through the use of an OPO, which is based on parametric down conversion in nonlinear crystal inside a cavity. However, the parametric down conversion process is not efficient for the generation of squeezed light on atomic resonance [62] because it must be pumped with UV light, which has high losses in the nonlinear crystal. Furthermore, to interact with atomic systems based on cold atoms, which have linewidths of 10 MHz, requires a cavity and locking system.

On the other hand, an atomic based squeezed light source offers a natural and more direct way to generate squeezed light that is narrowband and resonant with other atomic systems. Especially, an atomic system offers identical energy levels for every source, which can be applicable for building multi-mode squeezed system for

distributed quantum sensing and networking [63]. However, it is difficult to generate atomic resonance squeezed light with atoms due to the strong absorption when it operating close to resonance.

Despite these challenges, many experiments have produced narrowband atomic resonant squeezing light. For example, single-mode vacuum squeezed light resonant with the Rb D1 line has been generated with a periodically poled KTP crystal. With this system -4 dB of squeezing with bandwidths of 150 kHz to 500 kHz was initially obtained and improved to -5.6 dB of squeezing [64, 65, 62]. Similar systems have also been used to generate -3 dB of vacuum single-mode squeezed light on resonance with the D2 lines of Cs [66]. In terms of atomic-based sources, polarization self-rotation (PSR) in a rubidium vapor cell [67] has been used to generate vacuum single-mode squeezing on resonance with the D1 lines (-3 dB of squeezing) and the D2 lines (-1 dB of squeezing) of Rb [68, 69].

Here, we show the generation of bright two-mode squeezed states of light on resonance with ^{87}Rb and ^{85}Rb through the use of a FWM process in a ^{85}Rb vapor cell. First, we take advantage of the proximity of the D1 energy levels of the two rubidium isotopes to generate two-mode squeezed light where the beams can be on resonance with different transitions in the D1 line of ^{87}Rb. We measure -6.3 dB and -6.2 dB of squeezing when only one of the modes of the squeezed state is on resonance with the D1 line of ^{87}Rb. For a configuration in which each of the modes is on resonance with a different transition, we observe -3.9 dB of squeezing [70]

To increase the efficiency of the FWM process and generate squeezed light on

resonance with other atomic system, we combine the FWM with an additional optical beam. We first demonstrate an enhancement of the FWM to generate squeezed light on resonance with the D2 line of ^{87}Rb and the D1 line of ^{85}Rb. We then briefly discuss preliminary work on the generation of squeezed light resonant with the D1 line of sodium.

4.2 Resonant Squeezed Light using Rubidium Isotopes

In previous experiments, where we focused on maximizing squeezing, we used a non-degenerate FWM process in a double-lambda configuration in the D1 line of ^{85}Rb to generate near-atomic resonant squeezed light with an intensity difference squeezing of -9 dB. This setup generated squeezed light 800 MHz away from the rubidium resonant transition.

To generate resonant squeezed light, in principle we need to operate the FWM on resonance with a transition in rubidium. This is the original proposal for the double-lambda configuration [37, 33, 71]. Previous papers suggested that EIT can eliminate absorption when operating on resonance. However, the absorption still dominates over the FWM process when the probe frequency is close to resonance because EIT requires a high degree of atomic coherence, which is hard to achieve for the conditions needed for FWM, such as a hot vapor. To overcome this limitation, we take advantage of the proximity of energy levels in the D1 lines of ^{85}Rb and ^{87}Rb, as shown in Fig. 4.1(b), to generate squeezed light with ^{85}Rb that is resonant with ^{87}Rb.

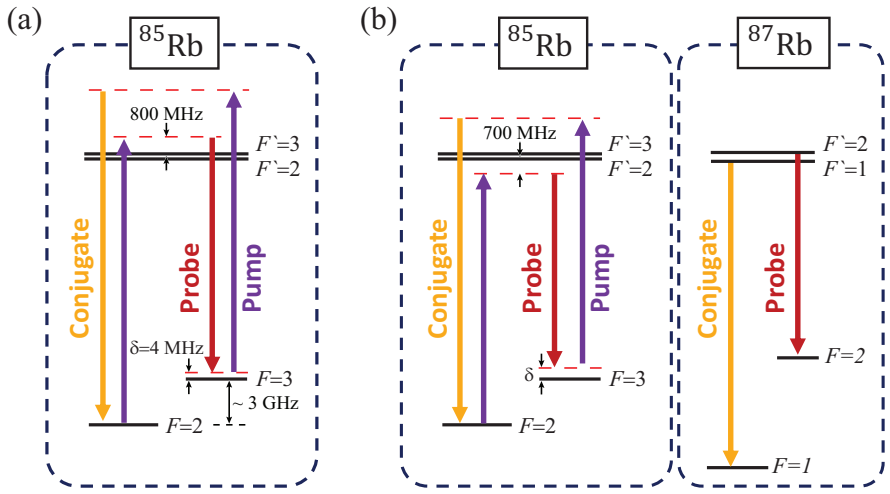

Figure 4.1: Energy level diagram of the double-lambda system in the D1 line of ^{85}Rb. (a) Optimized FWM configuration for the generation of off-resonance two-mode squeezed states with -9 dB of squeezing. (b) When the one-photon detuning of the pump is tuned $\sim$700 MHz to the red of the D1 $F = 2$ to F' transition of ^{85}Rb (figure on left), the generated probe and conjugate can be resonant with the D1 $F = 2$ to $F' = 2$ and $F = 1$ to $F' = 1$ transitions in ^{87}Rb, respectively (figure on right). Copyright (2018) by Optica Publishing Group. Reprinted with permission [12].

The D1 line of rubidium has a frequency difference between the fine structure of the two isotopes that is relatively small ($\approx$78 MHz), but a frequency difference between the hyperfine transitions that is large with the largest separation of 3.8 GHz between the transitions $F = 2$ to $F' = 3$ in ^{85}Rb and $F = 1$ to $F' = 2$ in ^{87}Rb. This energy level difference makes it possible to tune the frequency of the pump field required for the FWM in ^{85}Rb to generate two-mode squeezed light, such that either one or both of the twin beams are resonant with a transition in the D1 line of ^{87}Rb. We found that

red detuning the pump by around 700 MHz from the $F = 2$ to F' transition in ^{85}Rb, as shown in Fig. 4.1(b), can generate probe or conjugate resonant with the $F = 2$ to $F' = 2$ or $F = 1$ to $F' = 1$ transitions in the D1 line of ^{87}Rb, respectively.

The experimental setup is same as for the previous experiment. However, to verify that the squeezed light is on resonance, we take a portion of the probe beam before the FWM process and send it to a saturated absorption spectroscopy setup to obtain an absolute measurement of the probe frequency, as shown in Fig. 3.6. After the FWM process, we measure the beat note between the probe and the conjugate beams to get the frequency difference between them. This allows us to precisely determine the transitions to which the probe and conjugate are tuned to.

4.2.1 Singly-Resonant Configuration

Let us first consider the case where either the probe or conjugate is exactly on resonance with one of the transitions of ^{87}Rb. In this configuration, the one-photon detuning of the pump is set by the resonance frequency of the ^{87}Rb transition; however, the two-photon detuning can be optimized to achieve the maximum level of squeezing. The optimum level of squeezing is obtained using an angle of $\theta \approx 0.45^\circ$ between the pump and probe, pump power and $1/e^2$ diameter of 1 W and 1.9 mm, respectively, $1/e^2$ probe diameter of 0.6 mm, temperature of the vapor cell of 89°C, and two-photon detuning δ of 16 MHz.

We tune the frequency of the probe or the conjugate to be on resonance by changing the frequency of the laser. In Fig. 4.2(a), we show the probe and the conjugate as the

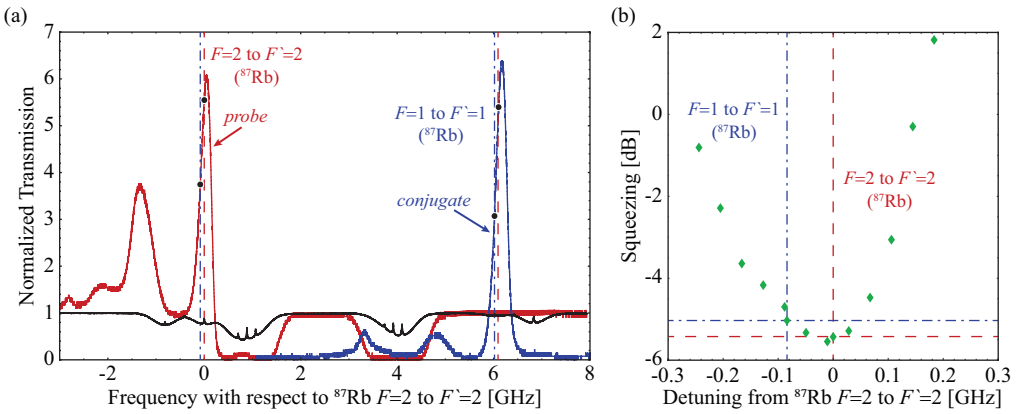

Figure 4.2: (a) Transmission spectra for the probe (red trace), the conjugate (blue trace), and saturated absorption spectroscopy spectrum (black trace) for a natural abundance Rb cell. The vertical red dashed (blue dashed-dotted) lines indicate the frequencies for the probe and the conjugate for the configuration in which the probe (conjugate) is on resonance with the D1 $F = 2$ to $F' = 2$ ($F = 1$ to $F' = 1$) transition of ^{87}Rb. The black dots indicate the normalized transmission for the probe and the conjugate for each of these frequencies. (b) Intensity difference squeezing as a function of the detuning of the probe from the D1 $F = 2$ to $F' = 2$ transition in ^{87}Rb. The vertical and horizontal red dashed (blue dashed-dotted) lines indicate the frequency at which the probe (conjugate) is on resonance and the corresponding level of squeezing, respectively. The spectrum analyzer was set to a resolution bandwidth of 30 kHz and a video bandwidth of 100 Hz. Copyright (2018) by Optica Publishing Group. Reprinted with permission [12].

one-photon detuning of the pump is scanned while the two-photon detuning is kept fixed at $\delta = 16$ MHz. With a one-photon detuning for the pump of 687 MHz to the

red of the D1 $F = 2$ to $F' = 2$ transition of ^{85}Rb the probe becomes resonant with the D1 $F = 2$ to $F' = 2$ transition of ^{87}Rb with a measured level of intensity difference squeezing of -5.4 dB. While for a one-photon detuning of 771 MHz, the conjugate becomes resonant with the D1 $F = 1$ to $F' = 1$ transition of ^{87}Rb with a measured level of squeezing of -5.0 dB. After subtracting the electronic noise, the squeezing level for the case of resonant probe or resonant conjugate increases to -6.3 dB and -6.2 dB, respectively, as shown in Fig. 4.3. Figure 4.2(b) shows the measured level of squeezing as we tune the laser frequency. As shown in the figure, we can obtain squeezing over a region of the order of 500 MHz around resonance for either of the transition in ^{87}Rb.

The measured levels of squeezing was significantly reduced from the previously obtained -9 dB with the off-resonance configuration. This is because the one-photon detuning is determined by the frequency of the transition. This brings the conjugate frequency closer to resonance with the D1 $F = 2$ to F' transition of ^{85}Rb. Therefore, the atomic system causes additional residual absorption, limiting the level of squeezing that can be achieved.

As discussed in Ch. 3, taking into account the detection efficiency of the system, the measured squeezing level can be compared to the ideal lossless limit. For our experimental setup, we have 98% to 99% transmission through the output anti-reflection coated window of the Rb cell. For the optical system before the detector, we estimate a transmission of 96% with 95% quantum efficient photodiodes. We obtain a total detection efficiency of $\sim$90%. Taking all losses into account using Eq. (3.16), the intensity differential squeezing level produced by the source is estimated to be -8.3 dB

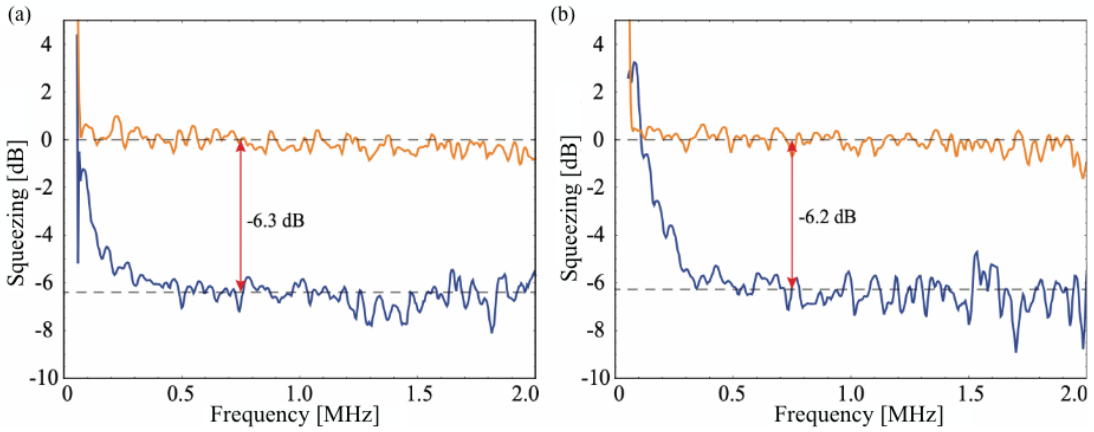

Figure 4.3: Intensity difference squeezing spectra. The orange traces show the shot noise limit while the blue traces show the intensity difference squeezing when the FWM is tuned to have (a) the probe on resonance with the D1 $F = 2$ to $F' = 2$ transition of ^{87}Rb and (b) the conjugate on resonance with the D1 $F = 1$ to $F' = 1$ transition of ^{87}Rb. For these measurements the electronic noise has been subtracted and the spectrum analyzer was set to a resolution bandwidth of 30 kHz and a video bandwidth of 100 Hz. Copyright (2018) by Optica Publishing Group. Reprinted with permission [12].

and -8.1 dB for the resonant probe and conjugate configurations, respectively.

We can estimate the intensity difference squeezing for the ideal lossless FWM process, through Eq. (3.13) given by $1/(2G-1)$. Experimentally, we have measured gains by comparing the ratio of the input probe to output probe after FWM and found gains of 5.6 and 3.8 for a resonant probe or conjugate, respectively. With the measured gain and ideal lossless equation, we calculate the levels of squeezing for the ideal limit to be -10 dB and -8.2 dB, respectively. The difference between the inferred and ideal

levels of squeezing for the resonant configuration is due to absorption of the probe in the atomic medium [43]. Given that the probe is further away from one-photon resonance, there is a better estimate between the inferred and ideal squeezing levels for the resonance conjugate configuration compare to resonance probe configuration.

The frequency difference between the probe and the conjugate is determined by the ground state hyperfine splitting of ^{85}Rb and the two-photon detuning. The measured beat note is 6.104 GHz, which is consistent with a two-photon detuning δ of 16 MHz. When compared to the optimum off-resonance configuration, δ is larger by a factor of four (4 MHz for off-resonance configuration). This is consistent with the frequency shift due to the AC Stark shift, or light shift [72],

$$\Delta E \propto \Omega^2/\delta \tag{4.1}$$

where ΔE is the light shift and Ω is the Rabi-frequency of the pump. Since the detuning of the pump coupling the D1 $F = 3$ to F' transition of ^{85}Rb is reduced from $\sim$4 GHz to $\sim$2 GHz, while the pump power required for the FWM is increased from $\sim$500 mW to 1 W, the light shift is increased by a factor of 4, consistent with the increase in the two-photon detuning.

Unfortunately, it is not possible to generate resonant squeezed light for other rubidium transitions, such as the D1 $F = 1$ to $F' = 2$ and $F = 2$ to $F' = 1$ transitions. The generation of squeezed light on resonance with the $F = 1$ to $F' = 2$ transition would require a one-photon detuning for the pump of 42 MHz to the blue of the $F = 2$ to $F' = 2$ transition in ^{85}Rb. This leads to a probe frequency too close to the $F = 3$ to F'

transition of ^{85}Rb, which results in absorption dominating over the FWM process. On the other hand, the generation of squeezed light on resonance with $F = 2$ to $F' = 1$ is also challenging. This case requires a "symmetric" configuration in which one of the Lambda transitions of the double-lambda configuration is detuned to the red of the D1 transition in ^{85}Rb by 1.86 GHz while the other is detuned to the blue by 1.17 GHz. Under these conditions, the responses from the two lambda systems interfere destructively and no gain is obtained for the FWM process [73].

4.2.2 Doubly-Resonant Configuration

Next, we examine the possibility of having both the probe and conjugate simultaneously resonant with the D1 $F = 2$ to $F' = 2$ and $F = 1$ to $F' = 1$ transitions in ^{87}Rb, respectively. In addition to fixing the one-photon detuning of the pump to 687 MHz to the red of the D1 $F = 2$ to $F' = 2$ transition of ^{85}Rb, this requires the frequency difference between the probe and the conjugate to be 6.02 GHz. Such a configuration is possible by setting the two-photon detuning δ to -26 MHz, which corresponds to a frequency difference between the probe and pump of 3.01 GHz. Given these constraints, the optimum level of squeezing is obtained for an angle θ of 0.5°, pump power and $1/e^2$ diameter of 1 W and 1.9 mm, respectively, $1/e^2$ probe diameter of 0.6 mm, and temperature of the vapor cell of 91°C.

Figure 4.4(a) shows the transmission spectra for the probe and the conjugate for the doubly-resonant configuration. With this setup, we measure intensity difference squeezing of -3.5 dB. After subtracting the electronic noise, the level of measured

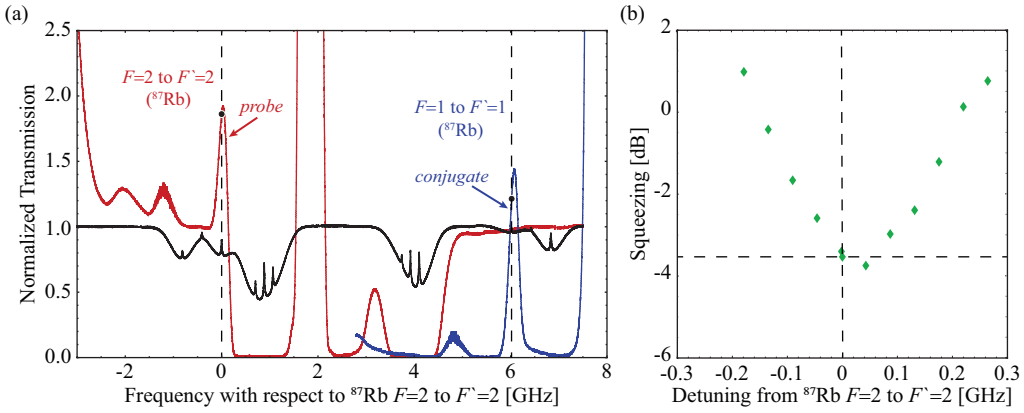

Figure 4.4: FWM configuration for probe and conjugate simultaneously on resonance. (a) Transmission spectra for the probe (red trace) and the conjugate (blue trace) generated with the FWM process in the D1 line of ^{85}Rb as the one-photon detuning of the pump is scanned while the two-photon detuning is kept fixed at $\delta = -26$ MHz. The black trace shows the saturated absorption spectroscopy spectrum for a natural abundance Rb cell. The vertical dashed lines indicate the resonance frequencies for the probe and the conjugate with the D1 $F = 2$ to $F' = 2$ and $F = 1$ to $F' = 1$ transitions of ^{87}Rb, respectively. The black dots indicate the normalized transmission for the probe and the conjugate for each of these frequencies. (b) Intensity difference squeezing as a function of the detuning of the probe from the D1 $F = 2$ to $F' = 2$ transition in ^{87}Rb. The vertical and horizontal dashed lines indicate the resonance frequency for the probe and conjugate and the corresponding level of squeezing, respectively. The spectrum analyzer was set to a resolution bandwidth of 30 kHz and a video bandwidth of 100 Hz. Copyright (2018) by Optica Publishing Group. Reprinted with permission [12].

squeezing increases to -3.9 dB. Considering the detection efficiency, we can infer the level of intensity differential squeezing generated by the source to be -4.7 dB, which is consistent with the predicted level of squeezing of -4.5 dB for the ideal lossless case with a measured gain of 1.9.

To check whether both modes are simultaneously on resonance, we first fix the frequency of the probe to the D1 $F = 2$ to $F' = 2$ transition peak of the saturated absorption spectrum in ^{87}Rb, as shown in Fig. 4.4(a). After fixing the probe frequency to the resonance transition, we measure the beat note between the probe and the conjugate to determine the frequency of the conjugate. Since we fixed the two-photon detuning, the beat-note frequency was measured to be 6.02 GHz, as expected. It is important to note that squeezing is still present when the laser detuning is tuned over a range of 300 MHz around the resonance, as shown in Fig. 4.4(b).

Both the level of squeezing and the tunability are significantly reduced with respect to the singly-resonant and off-resonant configurations. This is a result of having to fix the two-photon detuning in addition to the one-photon detuning. In this configuration, the FWM is no longer on two-photon resonance, as required for an efficient FWM process.

4.3 Resonant Squeezed Light using an Additional Laser Beam

Another approach used to generate resonant squeezed light from an atomic source is to use an additional laser beam. The additional laser can be used to excite the

electron from the lower energy level typically a ground state to a higher state to transfer population from one to the other energy level, which is called optical pumping [74]. The interaction of the laser with the atom can introduce an energy level shift called the light shift, as given by Eq. (4.1). As the laser interacts with an atomic structure, the interaction between them can create a new eigenstates of the combined system with field and atom, which is referred as atomic dressing. Additional laser beams can dress the atomic system and mix the energy levels and change the efficiency of FWM. Finally, the laser can saturate the atomic transition to decrease absorption [75]. An inefficient interaction and absorption, which are major limiting factors for generating resonant squeezed light, can be overcome with additional laser beams. Here, we describe our efforts in generating resonant squeezed light with an additional laser beam to obtain squeezed light on resonance with the D1 line and the D2 line of rubidium, and the D1 line of sodium.

4.3.1 Degenerate Four-Wave Mixing in the D1 Line of Rubidium

We first enhance the FWM process with an additional laser beam as an optical pump beam in a degenerate system. This is called degenerate FWM process. Unlike the non-degenerate FWM, which uses the two hyperfine ground state levels ($F = 3$ and $F = 2$), the degenerate FWM relies on magnetic sub-levels in $F = 3$ hyperfine ground level, as shown in Fig. 4.5(a). This means that the pump (π transition), probe (σ^- transition) and conjugate (σ^+ transition) beams all have the same frequency. Thus, the two-mode squeezed light generated by this process is doubly-resonant with the

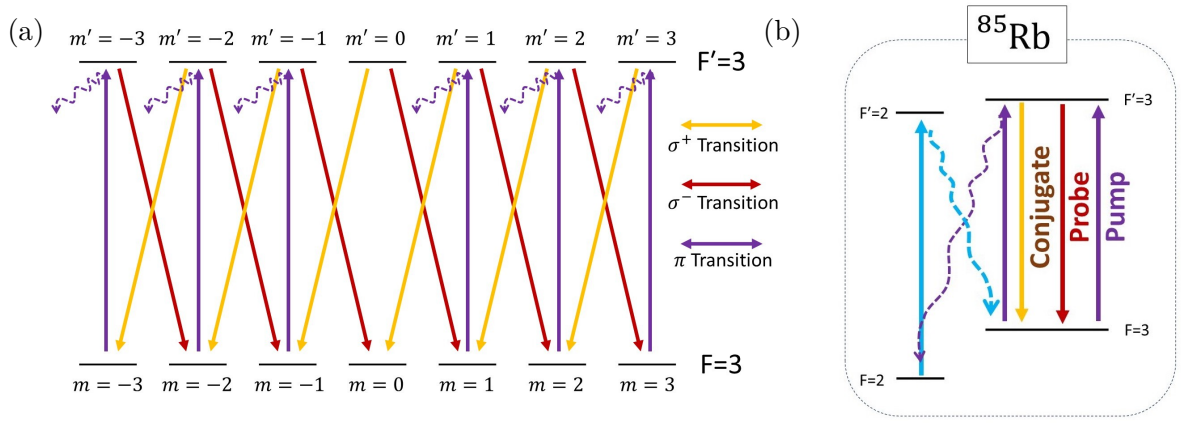

Figure 4.5: (a) Degenerate FWM process in the D1 $F = 3$ to $F' = 3$ transition in ^{85}Rb. The π transition (purple) is due to linearly polarized light, and $\sigma^{\pm}$ transition (yellow and red) by right and left circularly polarized light. (b) The optical pump beam (cyan) transfers population from the $F = 2$ to $F = 3$ state by coupling the $F = 2$ to $F' = 3$ transition to increase population of the $F = 3$ level.

corresponding atomic transition. This configuration was previously used with sodium to generate two-mode squeezed light with a squeezing of -0.2 dB [76].

Since the degenerate FWM process relies on near resonance, previous work only showed small amount of squeezing due to strong absorption and spontaneous emission, resulting in losses and excessive noise. Despite these limitations, a recent theoretical study showed that more than -3 dB of squeezing can be generated with low pump powers [77], which can be beneficial for a compact and low cost source of quantum light.

Figure 4.5(a) shows the energy level of the degenerate FWM using the D1 $F = 3$

to $F' = 3$ transition ($5^2S_{1/2}$ to $5^2P_{1/2}$). We choose this particular transition because it allows the most efficient process, as characterized by the gain. We suspect that this is a result of this transition having the highest number of possible parametric processes in the D1 line of ^{85}Rb. As can be seen from Fig. 4.5(a), the ground state $F = 3$ and the excited state $F' = 3$ have seven magnetic sub-levels $[m = -3, -2, -1, 0, 1, 2, 3]$ that can be coupled with π transitions and σ transitions such that $\Delta m = 0$ and $\Delta m = \pm 1$, respectively.

The degenerate FWM process in this configuration has four parametric processes with only two transitions that do not participate due to selection rules ($m = 0 \rightarrow m' = 0 \rightarrow m = 1 \rightarrow m' = 1 \rightarrow m = 0$ and $m = 0 \rightarrow m' = 0 \rightarrow m = -1 \rightarrow m' = -1 \rightarrow m = 0$). The π transition, which is forbidden for the transition $m = 0 \rightarrow m' = 0$ in $F = 3$ to $F' = 3$, acts as one of the loss mechanism for the degenerate FWM; as was shown previously [77]. However, they concluded that squeezing can occur despite the losses.

In addition to this losses mechanism, we found that there is another limiting process besides the forbidden π transition. For all alkali-atoms, there is always an extra ground state to which atoms can spontaneously decay to. This effect also limits the gain of the degenerate FWM process; however, this can be compensated for by using optical pumping to transfer the population back to the $F = 3$ ground state, as shown in Fig. 4.5(b).

The experimental setup is shown in Fig. 4.6. A CW Ti:Sapphire laser is used to generate the pump beam required for the FWM. A small portion of the pump is picked off before the Rb cell using a beam sampler to generate the probe beam. Both the

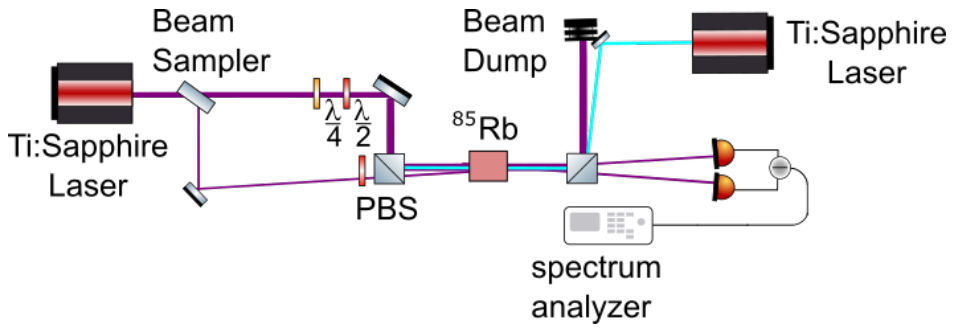

Figure 4.6: Simplified schematic of the experimental setup. The optical pump beam is counter propagating with respect to the FWM beams.

pump and probe are at the same frequency and delivered via optical fibers to clean up their spatial modes. After the fibers, perpendicularly polarized pump and probe beams intersect at an angle θ at the center of a 35.4 mm ^{85}Rb vapor cell with anti-reflection coated windows. After the FWM process, the pump beam is blocked by a polarization filter and the probe and conjugate beams are measured with a balanced detection system with 95% quantum efficient photodiodes. The optical pumping beam is taken from an independent CW Ti:Sapphire laser and counter propagated with respect to the pump through the vapor cell.

We first optimize the degenerate FWM process and find an optimal angle of 0.23° without an optical pumping beam. The pump and the probe power are 53 mW and 3.5 μW with $1/e^2$ diameters of 1 mm and 0.56 mm, respectively. The vapor cell is heated to 76°C and is enclosed by a magnetic shield. The magnetic shield is critical for this process because a magnetic field can introduce an energy level shift of the magnetic sub-levels in the $F = 3$ energy level, which can decrease the coherence of the atom and move some processes away from resonance. Figure 4.7(a) shows the transmission

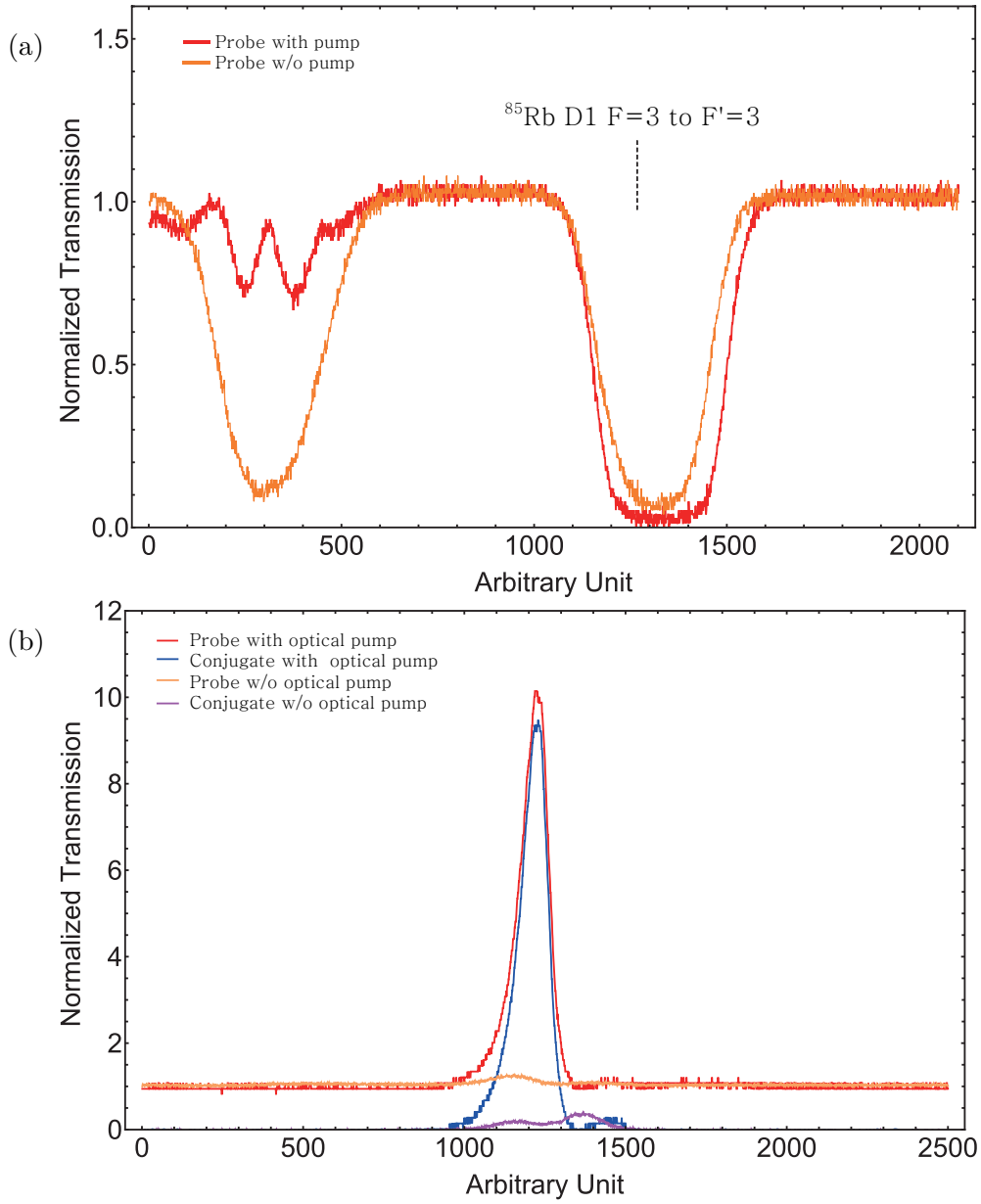

Figure 4.7: (a) Transmission spectra for the probe (orange trace) and the probe with optical pump beam (red trace) in the D1 line of ^{85}Rb and (b) Transmission spectra for the probe (red/yellow trace) and the conjugate (blue/purple trace) generated with the degenerate FWM process with/without the optical pump beam.

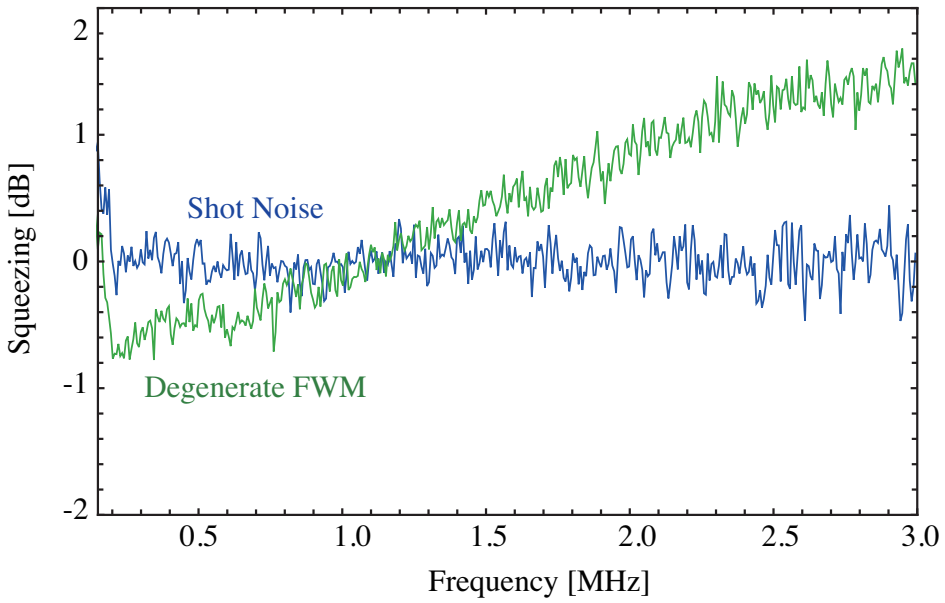

Figure 4.8: Intensity difference squeezing spectra. The blue traces show the shot noise limit while the green traces show the intensity difference squeezing via degenerate FWM process. For these measurements the electronic noise has been subtracted and the spectrum analyzer was set to a resolution bandwidth of 30 kHz and a video bandwidth of 100 Hz.

spectrum in ^{85}Rb for a weak probe beam (orange trace), and the spectrum with an addition optical pump beam (red trace). We want to note that in this preliminary data, we did not operate the experiment with saturation absorption spectroscopy, so we do not have frequency reference. Therefore, we could not show the probe and conjugate with the reference frequency. As can be seen, the presence of an optical pumping beam resonant with the D1 $F = 2$ to $F' = 2$ enhances the absorption of the D1 $F = 3$ to $F' = 3$ while decreasing the absorption of the D1 $F = 2$ to $F' = 2$ of ^{85}Rb.

Figure 4.7(b) shows the transmission spectrum of the probe (orange trace) and the

conjugate (purple trace) for the degenerate FWM. In this configuration we could not get any squeezing between the two beams, rather there was excess noise of 3.5 dB at the peak of the gain. We note that we observed an interesting phenomenon with the degenerate FWM process. In a typical non-degenerate FWM process, we can assume that the gain of the FWM process is dominated by the strong pump field, and the power of the seed probe does not play a role. However, the gain for the degenerate FWM depends on both the probe and the pump powers. Since the probe and the pump beams has relatively similar intensity due to the efficient degenerate process, high probe beam can switch the role of the probe and pump and generate another FWM process. For this reason, there are the dependence of the probe power for degenerate FWM process.

As we couple an optical pump beam with the degenerate FWM process, we lowered the temperature of the cell to 52°C and coupled a counter-propagating optical pump beam to enhance the degenerate FWM process. We used a 30 mW optical pump beam with a $1/e^2$ diameter of 1.5 mm at the center of the cell. We found that the least amount of noise was obtained for a pump and probe power of 75 mW and 12 μW, respectively. Figure 4.7(b) shows the enhanced gain of the probe (red trace) and conjugate (blue trace) for the degenerate FWM due to the optical pump beam. It can be seen that the gain is significantly improved due to the population transfer back to level $F = 3$.

With this setup, we measured an intensity difference squeezing of -0.8 dB when the probe and the conjugate are simultaneously on resonance with the D1 $F = 3$ to $F' = 3$ transition of ^{85}Rb. After subtraction of the electronic noise, the level of squeezing

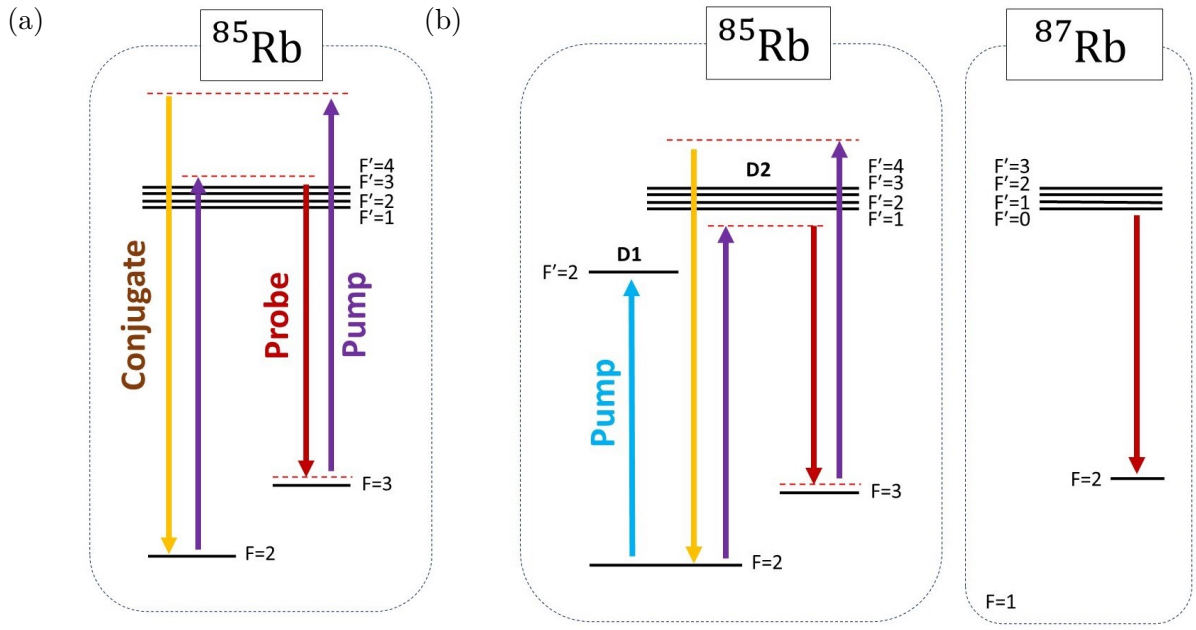

Figure 4.9: Energy level diagram of the double-lambda system in the D2 line of ^{85}Rb. (a) Optimized FWM configuration for the generation of off-resonance two-mode squeezed states with -3 dB of squeezing [78]. (b) Proposed diagram with the one-photon detuning of the pump tuned red of the D2 $F = 2$ to F' transition of ^{85}Rb to generate the probe on resonance with the D2 $F = 2$ to $F' = 0$ transitions in ^{87}Rb.

increases to -1 dB as shown in Fig. 4.8. The level of squeezing is significantly decreased because of the strong absorption due to operation on resonance.

4.3.2 Non-Degenerate Four-Wave Mixing in the D2 Line of Rubidium

Next, we use an additional laser beam to enhance the non-degenerate FWM on the D2 line of ^{85}Rb [79]. This was done in collaboration with my colleague, Christopher

Leonard, who led the effort. Since many experiments with cold atoms are performed in the D2 line of rubidium, generating atomic resonant squeezed light on the D2 transition will be useful for future integration of squeezed light and cold atomic systems. However, the D2 line is more complex than the D1 line, which leads to competing FWM processes between the different additional energy levels. Therefore, the non-degenerate FWM process on the D2 line usually exhibits less squeezing than on the D1 line [78].

To enhance the efficiency of the FWM process in the D2 line, there has been recent experimental work to improve off-resonance squeezing on the D2 line from -3.6 dB to -9 dB through the use of two additional laser beams [80]. This technique offers a viable way to extend the approach we introduced in Sect. 4.2 for generating resonant squeezed light on the D2 line.

Figure 4.9(a) shows the energy level diagram for the non-degenerate FWM in the D2 line ($5^2S_{1/2}$ to $5^2P_{3/2}$) of ^{85}Rb. This configuration produces more than -3 dB of off-resonant squeezing [78]. Using our approach introduced in Sect. 4.2, the FWM process can be configured such that the probe beam is resonant with the D2 $F = 2$ to $F' = 3$ transition in ^{87}Rb, as shown in Fig. 4.9(b). However, this did not lead to any squeezing due to the inefficiency of the process. Therefore, we use an additional laser beam resonant with the D1 $F = 2$ to $F' = 2$ transition of ^{85}Rb to enhance the FWM.

The experimental setup is shown in Fig. 4.10. Overall the experimental setup is similar to the FWM setup in Ch. 3, but here we tune the frequency of the probe and the pump on D2 line of rubidium, and the additional laser is on D1 line of rubidium, which is taken from an external cavity diode laser and amplified with a tapered amplifier

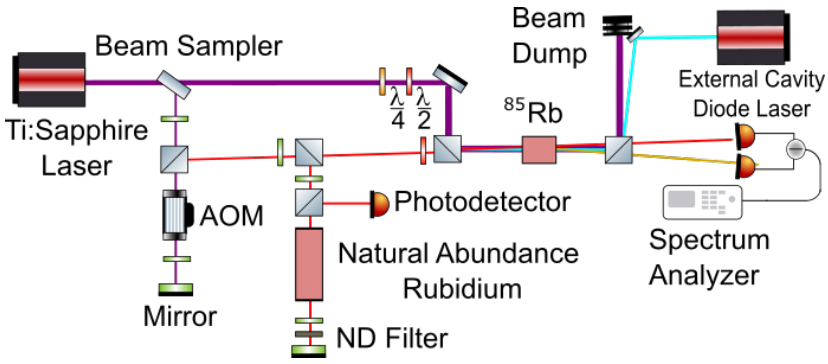

Figure 4.10: Simplified schematic of the experimental setup. An additional pump beam tuned to the D1 transition is counter propagating with the fields used to implement the FWM in the D2 line.

system. This additional pump is then sent in a counter propagating configuration through the center of the vapor cell at the power of 350 mW with a $1/e^2$ diameter of 0.58 mm. The FWM pump and probe beams intersect at an angle $\theta \approx 0.7°$ at the center of a 35.4 mm ^{85}Rb vapor cell with anti-reflection coated windows. In this configuration, the temperature of the vapor cell is set to 95°C. However, the optimum pump power for FWM decreases from 80 mW to 75 mW with $1/e^2$ diameter of 1.05 mm at the center of the cell.

This different behavior of optimum squeezing as a function of temperature and pump power with respect to the additional laser beam shows the different role that the additional beam plays compared to Sect. 4.3.1. In the last section, the optical pump beam transferred the population from one ground state to the another to increase the population contributing to the FWM process, thus providing more atoms that can participate in the FWM process. Given that larger population, it is possible to

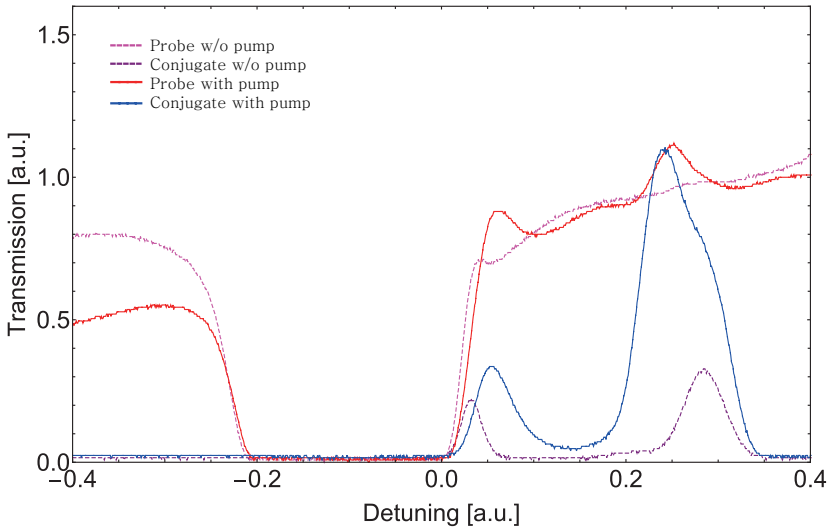

Figure 4.11: Transmission spectra in the D2 line of ^{85}Rb for the probe (red/pink trace) and the conjugate (blue/purple trace) generated with the FWM process with/without the counter propagating pump beam as the one-photon detuning of the FWM pump is scanned while the two-photon detuning is kept fixed at $\delta = 5$ MHz.

lower the temperature to reduce competing process of spontaneous decay due to the forbidden π transition.

In non-degenerate FWM, the process uses both ground states, so it seems that a temperature change would not be required with and without the additional laser beam because population transfer does not make the process significantly efficient. However, we believe that the additional laser beam is primarily used to dress the energy levels and control the efficiency of the FWM process. As the additional pump beam is dressing the FWM, overall efficiency of the process can be optimized. Thus, the required pump power decrease as the process becomes more efficient [81].

Figure 4.11 shows the transmission spectra of the probe (red/pink) and conjugate

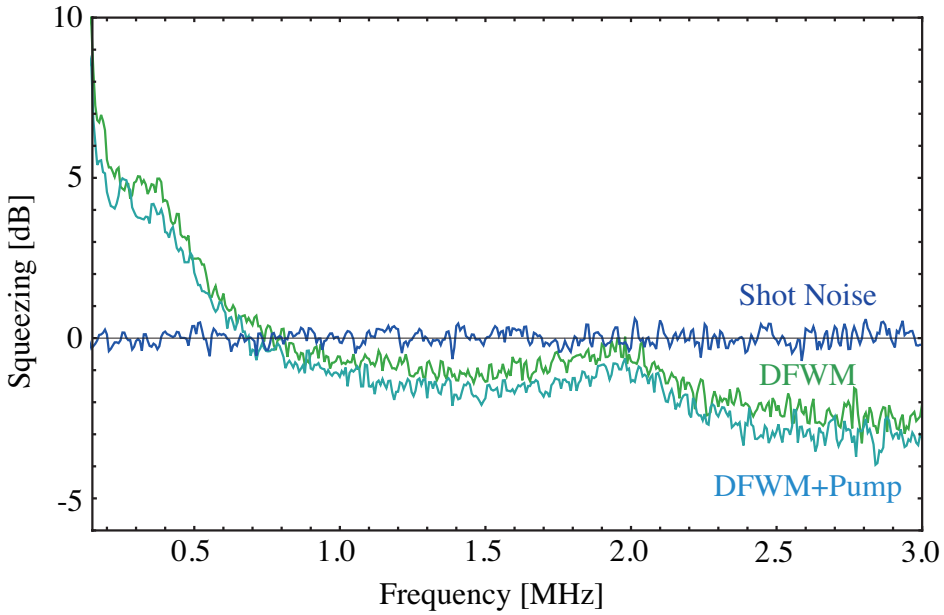

Figure 4.12: Intensity difference squeezing spectra. The blue trace shows the shot noise limit while the green and cyan traces show the intensity difference squeezing in the D2 line of ^{85}Rb with and without an additional pump beam, respectively. For these measurements the electronic noise has been subtracted and the spectrum analyzer was set to a resolution bandwidth of 30 kHz and a video bandwidth of 100 Hz.

(blue/purple) for the non-degenerate FWM with/without an additional pump beam. The coupling of the additional pump beam improves the gain of the FWM process even at lower pump powers. We can see the enhancement of the probe and conjugate gain around the detuning at 0 (arbitrary unit).

When the probe is on resonance with the D2 $F = 2$ to $F' = 3$ of ^{87}Rb, we measure -1.0 dB of intensity difference squeezing without the additional pump beam after subtraction of the electronic noise. The squeezing increases to -1.5 dB as we apply the additional pumping beam, as shown in Fig. 4.12, at an analysis frequency of 1.5 MHz.

We observe higher squeezing at higher frequencies, but further data needs to be collected since the noise at higher frequency is very close to the electronic noise.

The level of squeezing is significantly decreased compared to Ref. [80]. Since we are fixing the one-photon detuning to be resonant with the D2 $F = 2$ to $F' = 3$ transition of ^{87}Rb, our probe beam is closer to resonance with ^{85}Rb. However, we showed that coupling an additional pump beam can further enhance the FWM to generate twin beams with a larger degree of squeezing.

4.3.3 Non-Degenerate Four-Wave Mixing in the D1 Line of Sodium

In the final section of this chapter, we introduce an ongoing collaboration that uses an additional pump beam to generate squeezed light in sodium. This project is a collaboration with Dr.Arne Schwettmann and his students, Hio Giap Ooi, Qimin Zhang, and Matt Peters that has the goal of using squeezed light to probe a sodium Bose-Einstein condensate (BEC) [82, 83, 84, 85].

Although the first squeezed light was demonstrated in sodium nearly 40 years ago [32], large squeezing near a sodium resonance is still difficult. For crystals, the required wavelength is too short to be produced with ordinary PPKTP. This is because the crystal has to be pumped at 300 nm to produce squeezed light at 589 nm, which is significantly inefficient due to losses.

The generation of squeezed light with a sodium system is also a challenge because the hyperfine splitting of sodium (1.7 GHz) is small as shown in Fig. 4.13, compared to the Doppler broadening in atomic vapor. Compared to the other alkali systems, such

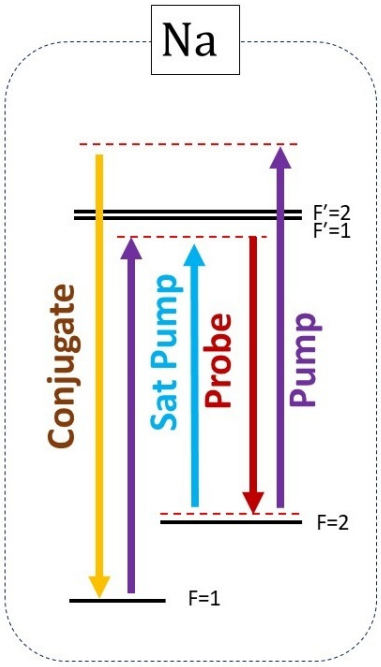

Figure 4.13: Energy level diagram of the double-lambda system in the D1 line of Na. We proposed using an additional pump to saturate the probe transition and reduce the absorption loss by the D1 $F = 2$ to $F' = 1$ transitions in Na.

as rubidium (3 GHz) and cesium (9.2 GHz), the Doppler-broadened absorption lines of sodium overlap with each other, which leads to a significant amount of loss from the absorption. Due to the high loss, it is difficult to show squeezing. Despite the challenge, previous work has implemented FWM in potassium vapor, where the hyperfine splitting (462 MHz) is smaller than the one for sodium [86] to produce -1.1 dB of squeezing. This showed that squeezing in a very lossy system is still possible.

Sodium systems pose additional challenges for the generation of squeezed light because its vapor pressure at a given temperature is relatively low compared to other alkali atoms. For example, a rubidium vapor density of 10^{-4} torr requires 100°C, but

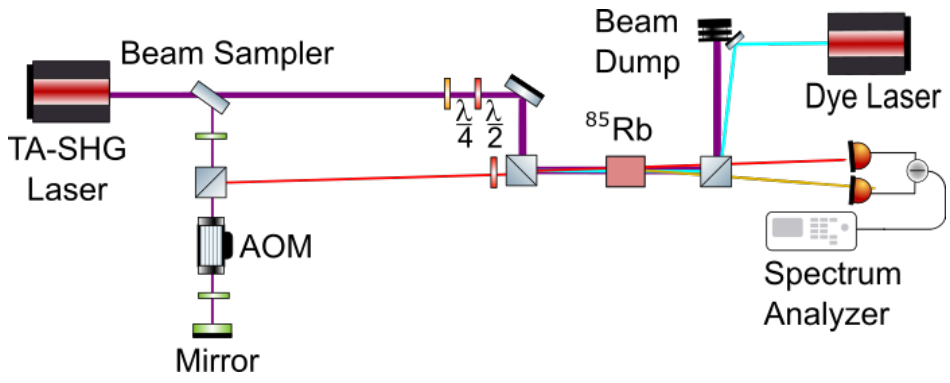

Figure 4.14: Simplified schematic of the experimental setup. An additional saturation pump beam is counter propagating with respect to the D1 Na FWM beams.

sodium has to be heated to 200°C to reach the same vapor pressure. This is a problem in particular for glass vapor cells because the sodium atoms interact with the glass at high temperatures, which limits the sodium vapor pressure and the efficiency of the FWM process. We are currently building an all-metal vapor chamber to solve this problem. While building the vapor chamber, we have demonstrated the effect of an additional pump beam to saturate the absorption transition and increase the transmission of the probe as part of the generating of squeezed light in the sodium D1 transition.

The experimental setup is shown in Fig. 4.14. A TA-SHG laser is used to generate the pump beam required for the FWM. A small portion of the laser is passed through an AOM to shift its frequency and generate the probe so that the frequency difference between the probe and pump is 1.76 GHz. The perpendicularly polarized pump and probe beams intersect at an angle $\theta \approx 0.1°$ at the center of a 76.2 mm Na vapor cell. After the FWM process, the pump beam is blocked with a polarization filter and

the probe and conjugate beams are measured with a balanced detection system. The additional pumping beam is taken from a dye laser and counter propagate through the vapor cell.

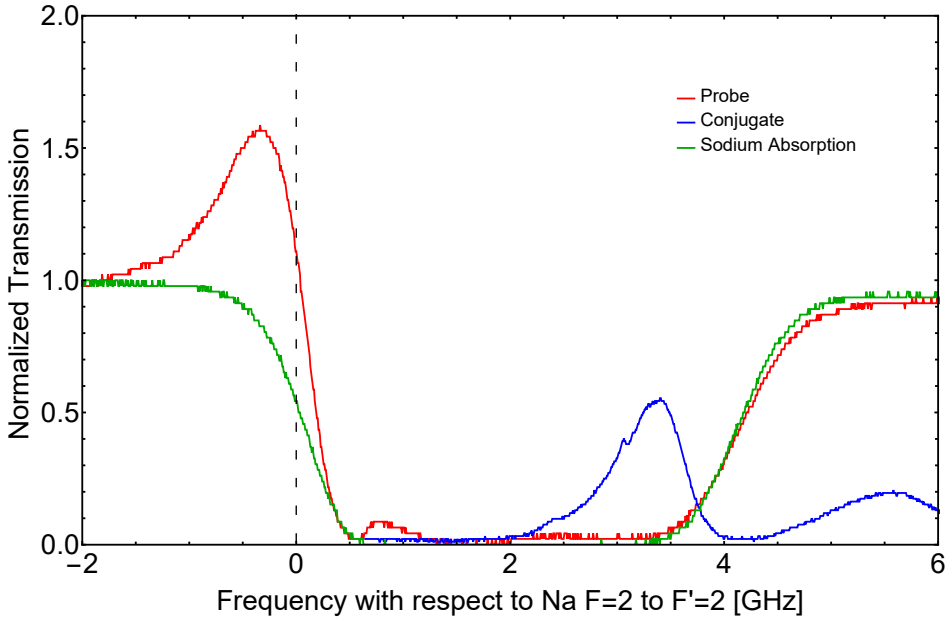

Figure 4.15: Transmission spectra for the probe (red) and the conjugate (blue) generated with the FWM process in the D1 line of Na as the one-photon detuning of the pump is scanned. Sodium transition is shown with green trace where we can observe that conjugate despite of strong absorption from the resonant transition.

Figure 4.15 shows the transmission spectra of the probe and the conjugate from the non-degenerate FWM an additional pump beam with a frequency equal to the one of probe field and a cell temperature of 160°C. The pump and probe powers are 800 mW and 200 uW with $1/e^2$ diameters of 1 mm and 0.5 mm, respectively. The additional pump beam counter-propagates to saturate the probe transition and reduce the absorption. Using an additional pump beam, we show a 10% improvement in

transmission from 20% to 30%.

In the FWM process in sodium, we have a limited gain for the process due to the temperature limit when using a glass cell. As we increase the temperature of the vapor cell to 160°C, we start to notice a decrease in the sodium pressure due to interactions of the sodium with the glass cell.

4.4 Conclusion

We have demonstrated the generation of bright two-mode squeezed light in which the probe and/or the conjugate can be on resonance with different transitions of ^{87}Rb and ^{85}Rb using either a non-degenerate or degenerate FWM process in ^{85}Rb.

Utilizing different transitions of rubidium isotopes, we obtain -3.9 dB of intensity difference squeezing for the doubly-resonance configuration in which the probe and conjugate are on resonance with the D1 transition in ^{87}Rb. The intensity difference squeezing increases to -6.3 dB and -6.2 dB when only the probe or the conjugate is tuned to resonance with the D1 transition in ^{87}Rb, respectively.

When combining the non-degenerate or degenerate FWM process with an additional pump beam, the FWM process is enhanced through the dressing of the atomic system or the redistribution of population, which helps with the generation of squeezed light resonant with the D1 line of ^{85}Rb and the D2 line of ^{87}Rb. At the end of the chapter, we present ongoing work to generate twin beams compatible with sodium though a FWM process assisted with an additional pump beam.

Our work on resonant squeezed light using atomic ensembles overcomes several experimental difficulties associated with crystal-based sources. The generation of resonant squeezed states with bandwidths of the order of the atomic natural linewidth will make it possible to study the interaction between atoms and quantum states of light. In addition, we believe that these quantum states of light will make it possible to enhance quantum devices based on atomic systems and to deterministically transfer the quantum correlations present between the probe and the conjugate to two remote atomic ensembles.

There are a few remaining limitations of the techniques we introduced in this chapter. For the degenerate FWM process in the D1 line of ^{85}Rb and the non-degenerate FWM in the D2 lines of ^{85}Rb, the level of squeezing is still too small due to strong absorption and an inefficient FWM process even with an additional laser beam. On the other hand, the non-degenerate FWM technique that takes advantages of isotopes can generate large level of squeezing, but it is not possible to generate resonant squeezed light for other rubidium transitions in the D1 lines of ^{85}Rb and particular transitions in the D1 lines of ^{87}Rb, such as the D1 $F = 1$ to $F' = 2$ and $F = 2$ to $F' = 1$ transitions.

To generate larger levels of squeezing and be able to reach different resonant transitions, it is required to increase the tunability of the FWM process. To overcome these challenges we describe our work in which we dress the atomic states of the source via a DC electric field in the next chapter.

Chapter 5

Frequency Tunable Squeezed Light Through Atomic State Dressing

> *At midday, O King, I saw on the way a light from heaven, brighter than the sun, shining all around me and those who were journeying with me. And when we had all fallen to the ground, I heard a voice saying to me in the Hebrew dialect, 'Saul, Saul, why are you persecuting me?*
>
> - St. Luke the Evangelist, *Acts 26:13–14*

To extend the applicability of squeezed light to atomic-based sensors, we showed in Ch. 4 that we can use FWM in an atomic vapor to generate resonant two-mode squeezed light. As discussed in Sect. 4, as the approach we used relies on an atomic system close to resonance, we suffered from strong absorption and small tunability, which are the main challenges in generating atomic resonance squeezed light for certain transitions.

Figure 5.1 shows results for resonant squeezed light with approaches introduced in Ch. 3 and Ch. 4. The squeezed light from the off-resonance FWM (red trace) is ∼800 MHz away from the D1 $F = 3$ to $F' = 3$ of ^{85}Rb and the squeezed light from the on-resonance FWM (orange trace) is 816 MHz away from the D1 $F = 2$ to $F' = 1$ of ^{87}Rb. To generate resonant squeezed light for more transitions in rubidium atoms, we now present a technique to increase the frequency tunability of squeezed light by using atomic dressing via an electric field. With this approach, we show a frequency shift by 600 MHz and show squeezing at the D1 $F = 3$ to $F' = 3$ transition of ^{85}Rb [87].

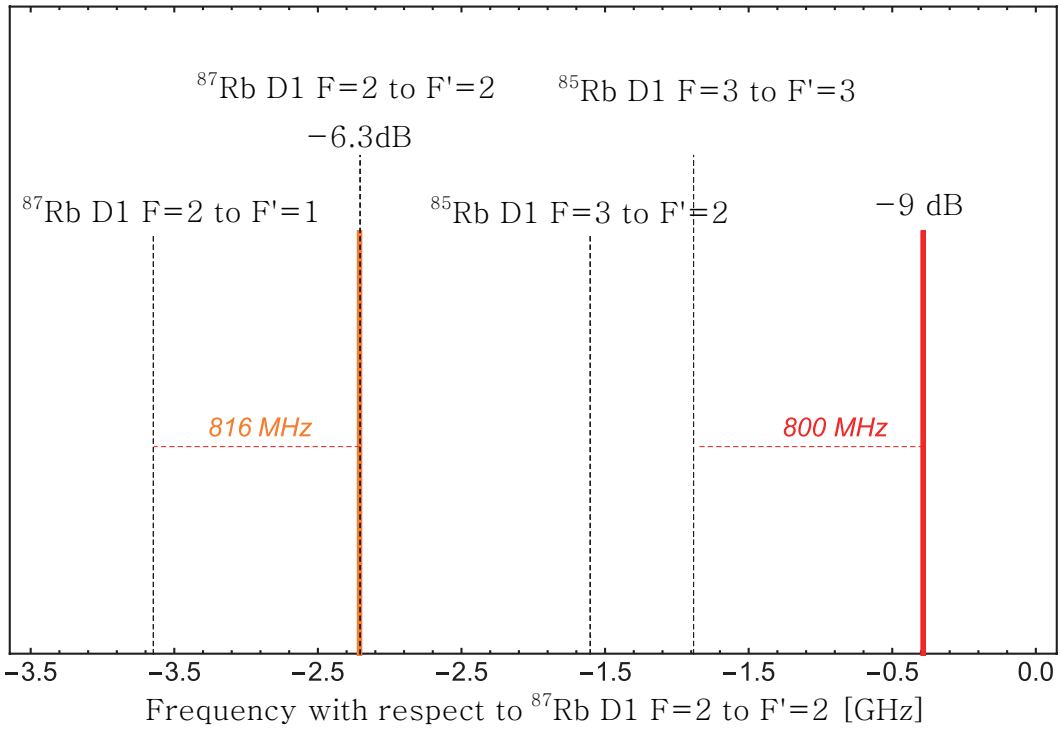

Figure 5.1: Generation of squeezed light off-resonance FWM (red) and on-resonance FWM (orange) with the level of squeezing. If the frequency tunability of the source can be increased more than 800 MHz, it is possible to generate resonant squeezed light for the D1 $F = 2$ to $F'1$ of ^{87}Rb and the D1 $F = 3$ to $F'3$ of ^{85}Rb, and the required frequency tunability is written on the dashed line.

5.1 Atomic Dressing and Four-Wave Mixing Process

To generate squeezed light on resonance with other transitions, we want to shift the energy levels without modifying the structure to keep larger levels of squeezing, so that light generated is resonant with atom not shifted. To do that, we use atomic dressing with an external field can tune the energy levels of atoms.

The common techniques to dress the atomic system are based on magnetic and

electric fields. The interaction between an external field and an atom can be modeled with a Hamiltonian of the form

$$H = H_0 + V_{int}. \tag{5.1}$$

where H_0 is the unperturbed Hamiltonian of the atoms, and V_{int} is the interaction Hamiltonian between the external field and the atom.

For a magnetic field, the interaction Hamiltonian takes the form $V_{int} = -\mu_{\mathbf{M}} \cdot \mathbf{B}$, where $\mu_{\mathbf{M}}$ is the magnetic moment of the atom and $\mathbf{B}$ is the magnetic field. In the absence of an external magnetic field, all the $2F + 1$ magnetic sub-levels, m_F, in the hyperfine energy level $\mathbf{F}$ are degenerate. However, when a small external magnetic field is applied to the atomic system, the degeneracy is broken and the level splits into $2F+1$ states with a shift due to the coupling between orbital $\mathbf{L}$ and spin $\mathbf{S}$, proportional to m_F. As the magnetic field increases, $\mathbf{L}$ and $\mathbf{S}$ couple with the magnetic field more strongly than to each other (magnetic Paschen–Back regime), resulting in the mixing of magnetic sub-levels. Therefore, magnetic field dressing is not ideal for increasing the tunability of FWM process, as it significantly modifies the energy level structure and introduces broadening of the absorption due to the splitting, which can increase the loss of squeezing.

For the electric field, the interaction with an external field is of the form $V_{int} = -\mu_{\mathbf{E}} \cdot \mathbf{E}$, where $\mu_{\mathbf{E}}$ is the electric dipole moment. The electric field can be either a static or an oscillating field. We studied the effects of an oscillating electric field to enhance FWM process by shifting energy levels with the AC Stark shift and introducing the

population transfer in Sect. 4.3. However, the AC Stark shift can shift the energy levels and break the degeneracy of the magnetic sub-levels, as well as it also requires a strong field to shift the energy levels by 800 MHz as needed to shift the energy levels to obtain resonant squeezed light [88]. Additionally, the strong coupling between the energy levels will produce other nonlinear processes and decrease the FWM efficiency.

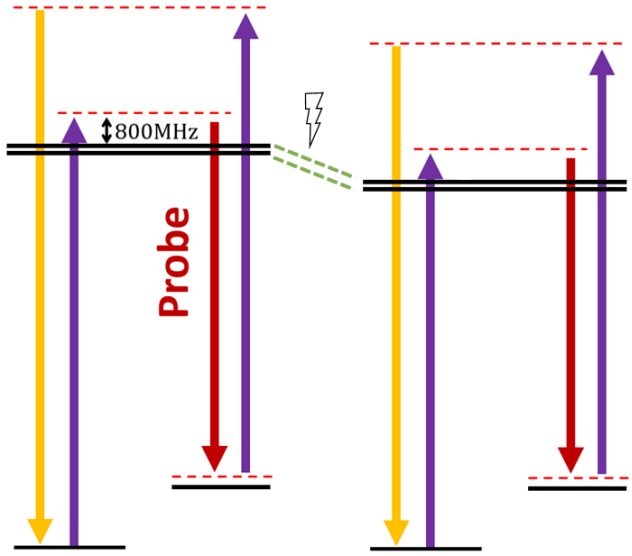

Figure 5.2: FWM process in the presence of a DC electric field. The DC Stark effect shifts the energy levels such that the source remains in its optimal configuration with an 800 MHz detuning from the D1 $F = 3$ to $F' = 3$ of ^{85}Rb and the generated probe beam shifts toward resonances for an atom in the absence of field.

In the case of static electric fields, the energy level shift due to the external field is called the DC Stark shift. The interaction Hamiltonian of the DC Stark shift can be calculated using ordinary second-order time-independent perturbation theory with the

assumption of a weak external field compared to the hyperfine splitting [89, 40, 90],

$$V_{int} = -\frac{1}{2}\alpha_0 E_z^2 - \frac{1}{2}\alpha_2 E_z^2 \frac{3J_z^2 - J(J+1)}{J(2J-1)}, \tag{5.2}$$

where α_0 and α_2 are the scalar and tensor polarizabilities, respectively, $\mathbf{J} = \mathbf{L} + \mathbf{S}$ is the quantum number associated with the total angular momentum that results from the coupling between $\mathbf{S}$ and $\mathbf{L}$, J_z is z-projection of $\mathbf{J}$, and E_z, is the electric field along the z-direction. For rubidium, the value of the polarizabilities have been obtained from the previous experiments [91, 92, 93], such that $\alpha_0(5^2S_{1/2}) = 0.0794\ h$ Hz/(V/cm)^2, $\alpha_0(5^2P_{1/2}) - \alpha_0(5^2S_{1/2}) = 0.1223\ h$ Hz/(V/cm)^2, $\alpha_0(5^2P_{3/2}) - \alpha_0(5^2S_{1/2}) = 0.1340\ h$ Hz/(V/cm)^2, and $\alpha_2(5^2P_{3/2}) = -0.0406\ h$ Hz/(V/cm)^2 with Planck constant h.

For our applications, the DC Stark shift offers a great advantage over effects due to other external fields, as states with total angular momentum $J = 1/2$ are not affected by tensor Stark shifts. As such, the only effects comes from the scalar terms, as shown in Eq. (5.2). The scalar term shifts the whole fine structure together without mixing the magnetic sub-levels or the hyperfine structure. This is crucial as 1) it will not change the optimal configuration for the FWM process used to generate squeezed light, and 2) it will not lead to broadening of the energy levels due to the magnetic sub-levels splitting. Therefore, this makes it possible to shift the energy levels, and provide a range of tunability of the atomic source. In Fig. 5.2 we show the energy level shift due to the DC Stark effect in the FWM process. As the shift increases, the frequency of the probe beam needed for the optimal FWM configuration approaches the D1 $F = 3$

to $F' = 3$ transition of ^{85}Rb atom in the absence of on external field.

Using Eq. (5.2), we can calculate the required voltage to shift the energy level for the D1 $F = 3$ to $F' = 3$ transition of ^{85}Rb by 800 MHz to generate resonant squeezed light. As shown in the Table. 5.1, a voltage of 17.2 kV should be applied across plates keeping a distance of 1.5 mm to obtain a field of 114.6 kV/cm. This requires special design of the vapor chamber that can sustain such a high electric field.

5.2 High Voltage Rubidium Chamber

Unlike previous implementations of the FWM given in Sect. 3 and Sect. 4, this approach requires constructing a vapor chamber that contains parallel plates that can supply a large DC electric field across the Rb atomic vapor. Figure 5.3 shows the final design of the vacuum chamber used for the experiment, which has a plate separation of 1.5 mm between the plates. Details of the design will be presented in later in the chapter. We apply the high negative voltage to one of the plates and connect the other plate to ground.

Shift (MHz)	100	200	300	400	500	600	700	800	900	1000
Voltage (kV)	6.0	8.5	10.5	12.1	13.6	14.9	16.0	17.2	18.2	19.2

Table 5.1: DC Stark frequency shift for the D1 $F = 3$ to $F' = 3$ transition of ^{85}Rb when a voltage is applied across plates with a separation of 1.5 mm.

Applying the required large electric fields inside the high voltage chamber, especially at high atomic number densities, is a difficult process because the electric field can lead

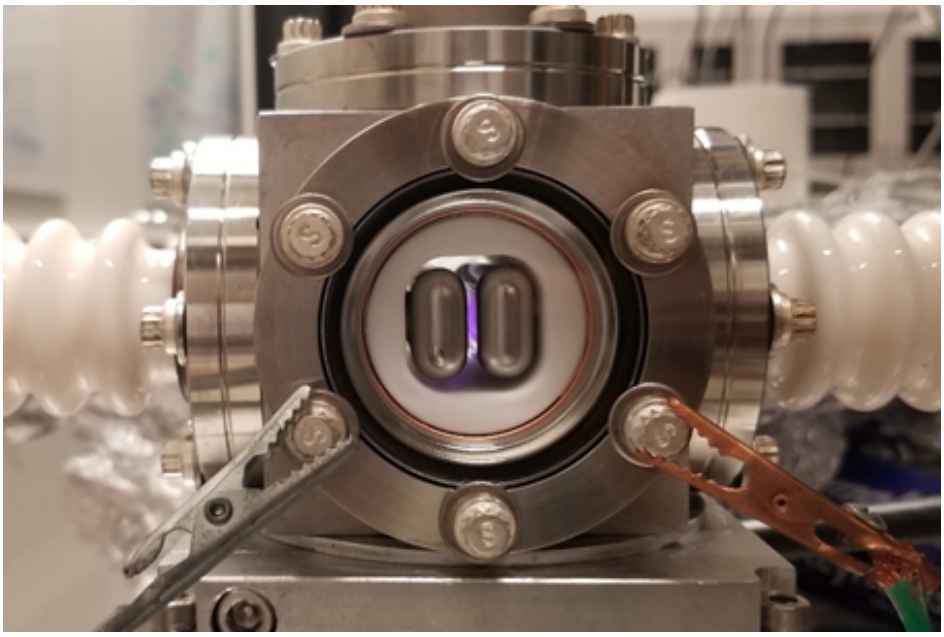

Figure 5.3: Picture of high voltage vacuum chamber used for the experiments. Two stainless plates are used to apply a high DC electric field. The plates are mounted inside a macor insulator. Plates are mechanically polished to maximize the curvature and electrically polished to minimize electrical arcing.

to ionization and electrical breakdown. There are previous studies that use a DC Stark shift in Rydberg atom transitions [94, 95, 96], but these systems only demonstrated shifts for small electric fields (of the order of 1 to 500V/cm). However, we not only need to apply extremely high electric fields (of the order of 100kV/cm) to the atoms, but also need to operate at high vapor pressure due to the typical FWM regime that requires a vapor pressure of 10^{-3} torr. Since the vapor pressure is close to the level used by rubidium discharge lamps [97], this makes it difficult to operate the high voltage vacuum chamber at the required electric fields. Therefore, to apply a large electric field

inside the chamber, the discharge effect described in the following subsections must be suppressed.

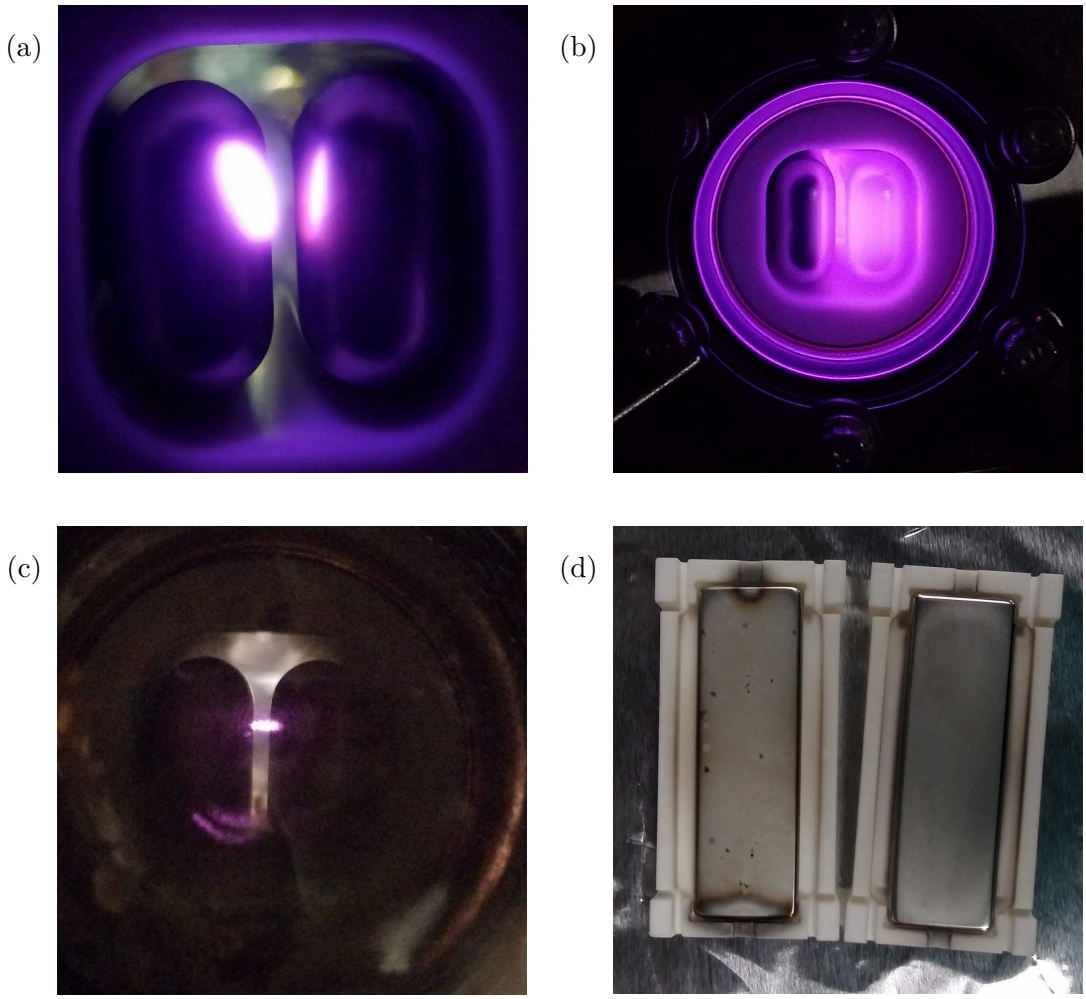

Figure 5.4: (a) and (b) Corona discharge due to contamination in the vacuum chamber. (c) Electrical arc discharge due to imperfections in the plates. (d) Damage from the breakdown voltage.

5.2.1 Corona Discharge

There are different types of discharge effects when working with high voltage systems. Corona discharge is a side effect of ionized atoms and electrons. When a neutral atom is ionized by a high electric field, positive ions and free electrons are produced. The ions and electrons are then accelerated in opposite directions by the electric field. During the process, electrons have a higher velocity than the positive ions due to the high charge/mass ratio as compared to the positive ions.

In our experiment, we apply a high voltage to one plate and ground the other plate. Therefore, if we apply a negative voltage, the conductor with high voltage will attract positive ions, while the positive voltage conductor will attract electrons. As ions and electrons accelerate and gain kinetic energy, they collide with other atoms and ionize them. This creates another positive ion and electron pair that can collides with more atoms. Such an avalanche process is called a positive corona if the conductor is negative, so the positive ions are accelerated toward the conductor. The effect is called a negative corona if the conductor is held at a positive voltage. We have tried both negative and positive voltages but decided to use a negative voltage as our positive voltage supply caused more problems such as damaging other devices due to arcing.

The process by which atoms recombine to emit photons of light creates beautiful colors, as shown in Figs. 5.4(a) and (b), and is often used as a discharge lamp. A corona discharge is a problem for our experiment because it makes impossible to increase the voltage inside the chamber to dress the atoms given that a connection between the

conducting and the grounding plates is effectively made.

5.2.2 Electric Arc Discharge

A corona can form even when a conductor is significantly separated from the other conductors. However, if the spacing between the two plates is close, electric current can flow between the two conductors, which creates arcing. This arc limits the strength of the electric field that can be applied across the two plates and depends on the pressure of the gas as determined by the Paschen's law [98, 99], which is an equation for breakdown voltage with respect to the pressure and the separation between the two plates.

Therefore, when the separation is small, even the smallest surface roughness on the plates can concentrate the electric field enough to make the system very sensitive to electric arcing. Also, as the pressure in the chamber increases, the likelihood of arcing increases. Therefore, it is important to smooth the plates as much as possible and lower the pressure of the vacuum chamber before we insert the rubidium into the chamber. We can see an electric arc discharge in Fig. 5.4(c). In addition to preventing high voltage, arcing can cause damage to the conducting plates and destroy of the insulation as shown in Fig. 5.4(d).

5.2.3 Partial Discharge

A partial discharge is a localized dielectric breakdown of a small portion of the insulator under high voltage. In our first design of chamber, shown in Fig. 5.5(b), two plates

were separated by pieces of Macor insulator. Macor glass is a good insulator with high dielectric strength, but small gaps between that the insulator and metal plates can experience an extremely high electric field because the dielectric constant of the small gap is less than the one of the surrounding dielectric, which makes the electric field across the small gap increases significantly. This create a partial discharge inside of the gap.

5.2.4 Chamber Designs

To prevent different types of discharge effects, we implemented chambers with different designs. In Fig. 5.5, we show the different iterations of the design of our high voltage vapor cell. We first tried a commercial vapor cell with inbuilt copper plates, as shown in Fig. 5.5(a), but this cell only worked at low electric fields because of the sharpness of the edges of the plates and the imperfections in the parallelness between the plates. Figure 5.5(b) shows the second design of the chamber, in which we held the plates together with a Macor insulator. As mentioned in Sect. 5.2.3, the voltage cannot be increased due to the partial discharge in the gaps between the insulators and the plates.

We then came up with the design shown in Fig. 5.5(c), which removes the insulation between the plates. Here the plates are held with a Macor insulator around the exterior of the plates and no additional elements between them. In this design, our plates were flat and thin, which created sharp edges at the ends of the plates. This lead to concentrated electric fields that created a corona effects. This problem led to the final design shown in Fig. 5.5(d), which eliminates the sharpness of the edges and

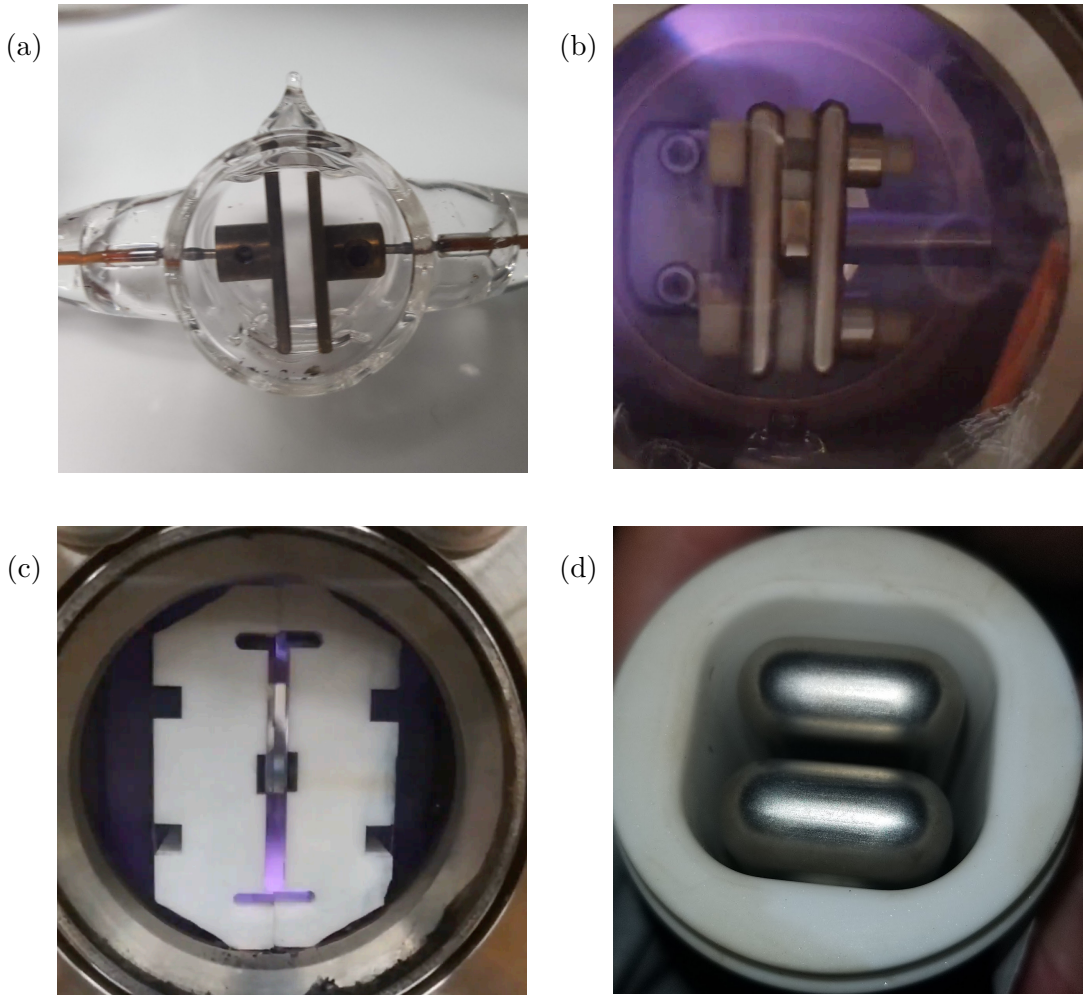

Figure 5.5: (a) Our first design with plates inside a commercial rubidium vapor cell. (b) Second design of the cell implemented in a vacuum chamber. (c) Third design of the cell to remove insulators between the plates. (d) Final design of the cell that maximizes the curvature of the plates.

maximize the smoothness of the plates and overall structure to solve the corona and partial discharges problems.

Our final design can support the plates and hold them parallel to each other. This

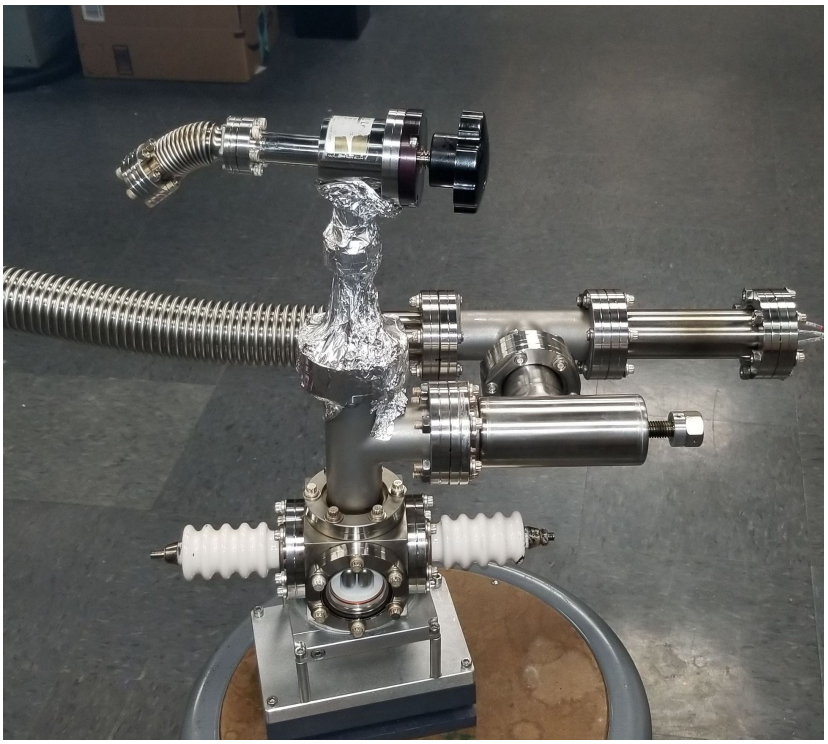

Figure 5.6: Final design of the high voltage vacuum chamber.

prevents the broadening of the rubidium absorption, as non-parallel plates introduce a nonuniform electric field. Our design not only provides more space for rubidium to migrate between the plates, but also prevents the partial discharge due to the localized dielectric breakdown by removing the insulation between the plates. We provide more details of the design in Appendix A

Additional measures are taken to smooth out the plates to minimize electrical arcing. To do this, we first grind the plates and then electropolish them to improve the surface finish, as shown in Figs. 5.7(b) and (c). In addition to smoothing the surface of plates, we used a commercial cube design and mechanically smooth and grind the interior surface of the chamber. We remove a spherical area inside of the cubic chamber, as

(a) 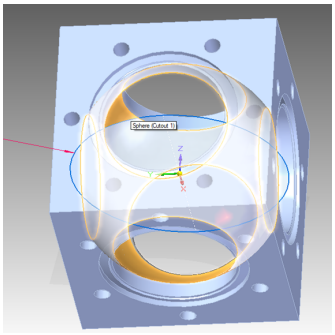 (b)  (c) 

Figure 5.7: (a) Spherical area inside the chamber made with mechanical grinding with a CNC (Computer numerical control) machine, (b) electropolishing of the plates to remove a thin layer of material from the stainless plates, and (c) plates after mechanical and electropolishing of their surfaces.

shown in Fig. 5.7(a).

After polishing, we assemble the plates inside the vacuum chamber. The final assembly of the vacuum chamber is shown in Fig. 5.6. We slowly apply an electric field to create a controlled arc. The small arcs that appear due to imperfection in the surface of the plates help to remove any left over roughness in the surfaces.

After smoothing the plates and the chamber, we first test the vacuum and capability of applying a high voltage. After testing, we insert the rubidium into the high voltage chamber. To insert the rubidium, we use a bellow to hold an ampule with Rb. We then bend the bellow to crack the break-seal of the ampule. More details on the design and how the rubidium is migrated to the region between the plates are in Appendix A. Our system can support electric fields on the order of 110 kV/cm.

5.3 Experiment

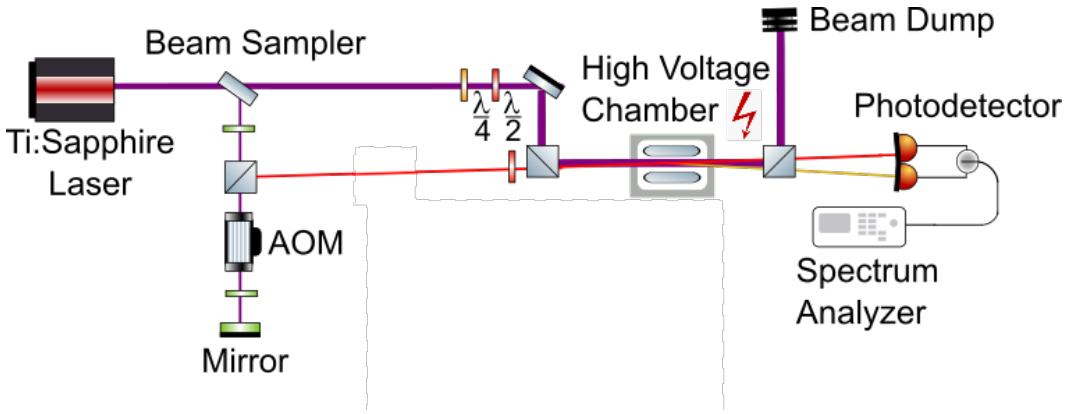

Figure 5.8: Simplified schematic of the experimental setup. The pump and probe beams intersect at a slight angle inside a ^{85}Rb high voltage vapor chamber.

To test the frequency tunability of the generated squeezed light with the high voltage chamber, we use the experimental FWM setup shown in Fig. 5.8. The overall setup is the same as the previous one we used in Ch. 3, but we replace the vapor cell with our high voltage chamber. The pump and probe after the fibers are sent to the high voltage rubidium vapor chamber at an the angle of 0.3° between them. We first optimize squeezing in the D1 line of ^{85}Rb, which leads to a pump power of 1 W with a $1/e^2$ diameter of 1.3 mm and a probe with $1/e^2$ diameter of 0.6 mm. The temperature of the chamber is 85°C and the two-photon detuning δ is set to -1 MHz.

5.3.1 Results in the D1 Line

Figure 5.9(a) shows the transmission spectra for the probe after the FWM in the D1 line of ^{85}Rb. The red trace indicates FWM without an electric field and as the electric

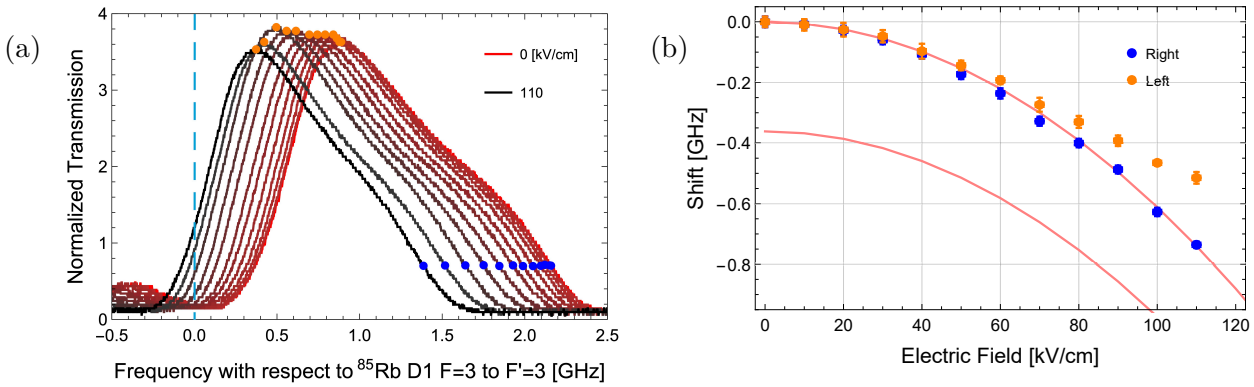

Figure 5.9: (a) Transmission spectra for the probe generated with the FWM process in the D1 line of ^{85}Rb as the one-photon detuning of the pump is scanned while the two-photon detuning is kept fixed at $\delta = -1$ MHz. The x-axis shows the one-photon detuning frequency with respect to $F = 3$ to $F' = 3$ transition in the D1 line of ^{85}Rb. The red trace shows the FWM without an electric field, and as the trace changes to black, the stronger the applied electric field is. The orange and blue dots are tracking points for the peak of the FWM and the shift of the spectrum, respectively. (b) Frequency shift of the two tracking points for the DC Stark shift. Blue dots exactly follow the theoretical prediction (red line) of the D1 line shift in the $^5S_{1/2}$ to $^5P_{1/2}$ transition. The two excited states in the $^5P_{1/2}$ experience energy level shifts due to the external electric field by the prediction.

field is applied the traces transitions to black. The black trace on the far left shows the FWM with an applied field of 110 kV/cm. The orange and blue dots are the tracking points for the peak of the FWM and the shift of the spectrum, respectively.

In Fig. 5.9(b), we can see two different behaviors for the two tracking points. The

peak of the FWM gain (orange dots) shows a smaller shift than expected, with a maximum shift of 510 MHz. On the other hand, we can see that the tracking point (blue dots) are in good agreement with the theoretical predictions from Eq. (5.2), with a maximum measured shift of 730 MHz, as shown in Fig. 5.9(b), in agreement with the predicted shift of 730 MHz.

The different behavior between the two tracking points is due to absorption from the D1 $F = 3$ to $F' = 3$ transition in ^{85}Rb. As we increase the electric field, the peak of the FWM gain gets close to resonance. However, there is some residual rubidium in the small gap between the plates and the windows that do not see the same field and do not experience a significant DC stark shift. This introduces absorption as the FWM approaches resonance, which lead the a decrease of the FWM gain and deforms the gain profile. This limits the shift of the maximum of the FWM gain. However, the location of the blue tracking points does not experience any absorption as we increase the frequency; therefore, we can see good agreement between the theory and the blue tracking points, but not with the orange tracking points as we increase the electric field.

Despite the decrease in gain, we measure -3.8 dB of squeezing after subtracting electronic noise and show that the level of squeezing is preserved in the presence of a high electric field, as shown in Fig. 5.10(a). The red dots represent the squeezing measurements without an electric field. The black dots show the squeezing with an electric field of 106 kV/cm. The frequency error bars are obtained from the uncertainty in the wavemeter which we use to measure the absolute frequency of the probe, and

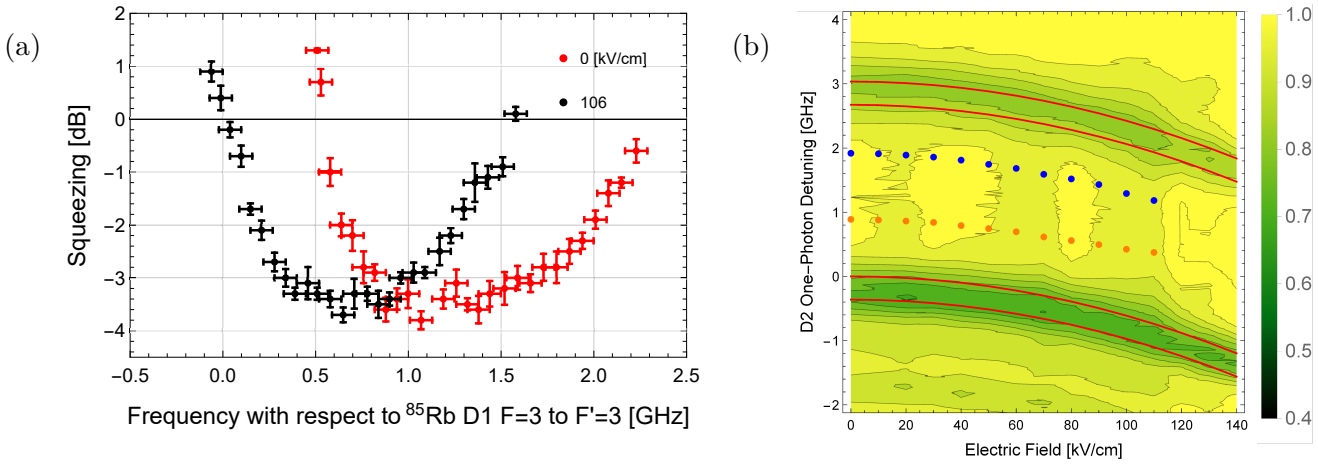

Figure 5.10: (a) Intensity difference squeezing as a function of the one-photon detuning at an analysis frequency of 1.25 *MHz. Squeezing is preserved after the atomic dressing and squeezing is present over a range of 1.5 GHz around the maximum squeezing. This shifts the frequency of the squeezed light by* 600 *MHz and extends the tunability range of the squeezed light. The spectrum analyzer was set to a resolution bandwidth of* 30 *kHz and a video bandwidth of* 100 *Hz. (b) Contour plot of the normalized saturation absorption spectroscopy transmission of the chamber at* $35^{\circ}C$ *in the D1 line as a function of the electric field. Blue and orange dots represent the tracking points of the shift from the FWM result, and the red line is the theoretical prediction.*

the error bars for the squeezing level are obtained from the standard deviation of the squeezing measurements around the analysis frequency of 1.25 MHz. For these measurements, the spectrum analyzer was set to a resolution bandwidth of 30 kHz, a video bandwidth of 100 Hz, and an analysis frequency of 1.25 MHz. Thus, we increase

the frequency tunability of the squeezed light by 600 MHz, which makes it possible to reach resonance with the D1 $F = 3$ to $F' = 3$ transition of ^{85}Rb .

Figure 5.10(b) shows the contour plots of the normalized transmission obtained with saturation absorption spectroscopy. For these measurements, we decreased the temperature of the chamber to 35°C to obtain the absorption spectrum for the rubidium transitions. As can be seen, the theoretical predictions of the energy level shifts due to the DC stark effect align well with the measured absorption shifts.

5.3.2 Results in the D2 Line

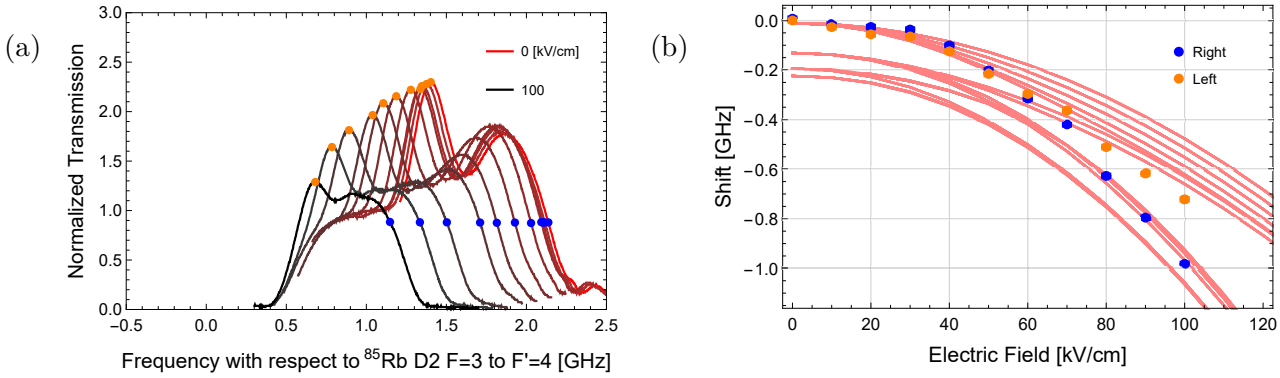

Figure 5.11: (a) Transmission spectra for the probe generated with the FWM process in the D2 lines of ^{85}Rb with respect to the one-photon detuning of the pump. (b) The two tracking points and the theoretical prediction (red line) for the D2 line shift in $^5S_{1/2}$ to $^5P_{3/2}$ transition.

We repeated the experiment in the D2 line of rubidium. The energy level shift in the D2 line is more complicated than in the D1 line. The total angular momentum of the D1

line, $J = 1/2$, means that it is not affected by the tensor Stark shift; however, the D2 line does mix the magnetic sub-levels and hyperfine structure through the second-order effect, which leads to atomic dressing in the electric hyperfine Paschen-Back regime. Therefore, we are expecting larger frequency tunability but with a change the energy level structure with respect to the optimal FWM due to the splitting of energy levels. Similar to the reason why we did not uses magnetic field to dress the atomic system, the use of the DC Stark effect on the D2 line to generate tunable squeezed light will lead to the splitting and mixing of energy level that will degrade the FWM.

As we optimize the process, we decreased the pump power to 400 mW, and increased the temperature from 85°C to 95°C. The two-photon detuning δ is set to -3 MHz. Figure 5.11(a) shows the transmission spectra for the probe in the D2 line. Without the electric field (red trace), the gain of the FWM is significantly decreased compared to that of the the D1 line, as shown in Fig. 5.9(a), due to an inefficient FWM in the D2 line transition. As we increase the strength of the electric field, the peak of the FWM gain shifts by a larger amount and the FWM gain decrease faster than in the D1 line due to the effect of the tensor Stark shift and also getting close with the resonance. As a result, we observed that as the spectrum shifts toward the $F = 3$ to $F' = 4$ by 1 GHz, the peak of the gain shift by only 720 MHz for an applied field of 100 kV/cm, as shown in Fig. 5.11(b).

Fig. 5.12(a) shows a measured level of -2.2 dB of squeezing after subtracting the electronics noise at an analysis frequency of 1.65 MHz without electric field. Despite the splitting of the energy levels, we were able to shift the frequency of the squeezed

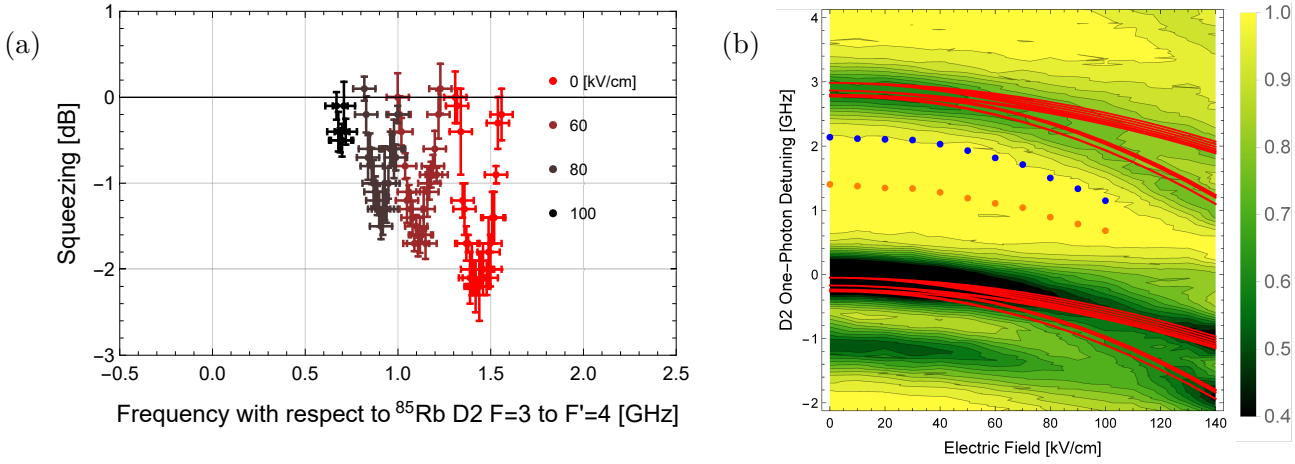

Figure 5.12: (a) Intensity difference squeezing in the D2 lines as a function of one-photon detuning with respect to squeezing at an analysis frequency of 1.65 *MHz. Electric field shifts the frequency of the squeezed light by* 740 *MHz peak to peak. The spectrum analyzer was set to a resolution bandwidth of* 30 *kHz and a video bandwidth of* 100 *Hz. (b) Contour plots of the normalized saturation absorption spectroscopy transmission of the chamber at 35 °C in the D2 lines as a function of the electric field. Blue and orange dots represent the tracking points of the shift from the FWM measurements, and the red line is the theoretical prediction.*

light by 740 MHz with −0.7 dB of squeezing remaining. Squeezing decreases as the electric field increases, consistent with a decrease of the FWM gain.

Figure 5.12(b) shows the contour plots of the normalized transmission obtained with saturation absorption spectroscopy. We can see that the magnetic sub-levels are mixed together and split according to the value of $|m_J|$ as we increase the electric field. This is result of the experiment in the electric hyperfine Paschen-Back effect

analog to the Paschen-Back effect for magnetic fields. We believe this approach can be viable for sufficiently large electric fields where we can separate the $|m_J| = 1/2$ and $|m_J| = 3/2$ manifolds completely. This would lead to a good candidate for a source of large-frequency tunable squeezed light, since those levels are much more sensitive to a DC electric field.

5.4 Limitations

Compared to previous squeezed light generation [78], we obtained less squeezing -4 dB and -2 dB in the D1 line and the D2 line, respectively, compared to -9 dB and -3.5 dB in a vapor cell. This is because we have higher losses at the vacuum chamber ($T = 75\%$), residual atoms between the plates and the windows, and a tighter phase-matching condition due to a longer ~ 7 cm propagation the vacuum chamber compared to the 2.54 cm commercial vapor cell.

In our experiments, the maximum electric field is limited by electrical breakdown, also as the vapor pressure increases, arching is unavoidable due to imperfections in the surface of the plates, ionization by atomic collisions, and contamination of the vacuum inside the chamber. For these reasons, the higher the temperature of the chamber, the faster electrical breakdown is observed.

5.5 Conclusion

We demonstrate frequency tunable squeezed light generation through atomic state dressing with a large DC electric field. Our system can support electric fields up to 110 kV/cm, which leads to a shift of 730 MHz and 1 GHz in the D1 and the D2 transitions, respectively. This allows us to generate rubidium resonant squeezed light and increase its frequency tunability by 600 MHz and 740 MHz with -3.8 dB and -0.8 dB of squeezing in the D1 and the D2 transitions, respectively. Squeezing in the D1 line is preserved as we increase the electric field, but we observe that squeezing in the D2 line decreases due to energy level mixing in the electric hyperfine Paschen-Back regime.

Our technique will open the door to the generation of alkali-resonant squeezed light and increased frequency tunability [100, 101, 102]. In addition to its application to frequency tunable resonant squeezed light, our system can serve for precise measurements of the atomic polarizability [92] and provide a platform for frequency tunable atomic processes based on Rydberg atom, EIT transitions, and polarized self-rotation [103].

Chapter 6

Generation of Single-Mode Squeezed States of Light Using Feedforward

Death is not an event in life: we do not live to experience death. If we take eternity to mean not infinite temporal duration but timelessness, then eternal life belongs to those who live in the present. Our life has no end in just the way in which our visual field has no limits.

- Ludwig Wittgenstein, *Tractatus Logico-Philosophicus*

In Ch. 4 and Ch.5, we discuss possible methods to generate resonant two-mode squeezed light using a degenerate and a non-degenerate FWM process. The resonant property of these states opens up the possibility of squeezed light interacting with atomic systems. The next two chapters will introduce a technique that can extend the applicability of squeezed light by showing the control of the quantum properties of light.

Quantum properties, such as entanglement and uncertainty principles, are used in quantum communications [49] and quantum computers to implement certain algorithms not possible with classical systems to develop new drugs [104], optimize the material properties for batteries [105], and financial analysis [106]. Among the many candidates that can provide the quantum resources needed for quantum computers, squeezed light offers a fundamental building block [107, 52].

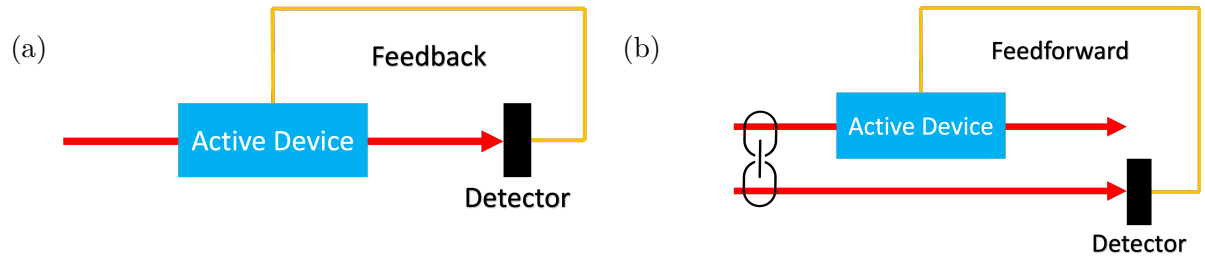

Figure 6.1: Example of control of the noise properties of light (a) using a single beam with feedback and (b) twin beams with feedforward.

Therefore, creating quantum states of light, transferring, and controlling their quantum properties plays an important role in quantum information science. This chapter introduces a feedforward technique for transferring the quantum properties of the light to show that we can generate single-mode amplitude squeezed light by transferring the quantum properties from two beams to one.

6.1 Transferring Quantum Fluctuation Using Feedforward

There are many techniques to control the classical properties of light (noise above QNL), such as the use of a noise eater to cancel classical technical noise. This idea of reducing the classical noise is applied to reduce the noise below QNL. This has been done via controlling the active device and semiconductor laser [108], as shown in Fig. 6.1(a). However, this requires monitoring the total intensity of the light to feedback the signal to the active device, so it is not possible to extract the quantum properties from such a system.

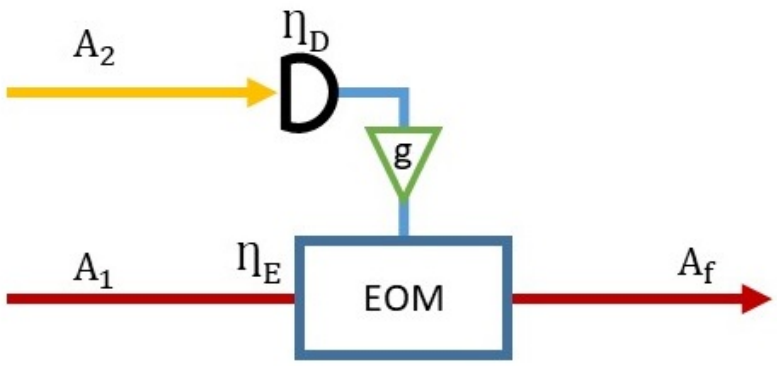

Figure 6.2: Schematic of the feedforward setup. One mode (conjugate) from the FWM process is measured with a photodiode and the resulting photocurrent is used to drive the EOM in order to modulate the other mode (probe). Through the feedforward process, we can reduce the noise of the probe below the QNL.

After the discovery of twin beams that have quantum correlation between two modes, the idea of controlling the device to feedback in closed-loop system extended to feedforward. If we use the noise information from one of the beams to modulate intensity of the second beam, we can reduce the noise of the second beam because the intensity fluctuations of the two beams are correlated [109], as shown in Fig. 6.1(b). The intensity difference squeezing present in two-mode squeezed states can be transferred to single-mode squeezing using active control on one beam with an electro-optic modulator (EOM) based on the measurement of fluctuations of the other beam [110]. This technique is called feedforward.

Figure 6.2 shows the schematic of the feedforward setup. We first measure the

fluctuations of optical field A_2 with a photodetector. The intensity fluctuations of optical field A_2 are then converted to current fluctuations and amplified with gain g. The amplified intensity fluctuation signal is used to modulate the transmission through the EOM, and as a result the intensity of A_1. If there are a quantum correlations between A_1 and A_2, the intensity fluctuation of A_f after the feedforward can have reduced intensity noise below the QNL.

This process can be modeled by using a semi-classical approach based on the linearization of the operator as described in Ref. [111]. For this, we can write an operator $\hat{A}_i$ as

$$\hat{A}_i = \langle \hat{A}_i \rangle + \delta \hat{A}_i, \tag{6.1}$$

where $\hat{A}_i$ is a time dependent field operator for each beam (i=1,2), $\langle \hat{A}_i \rangle$ is the mean value of the field,and $\delta \hat{A}_i$ are the fluctuations of the field. Since we are measuring the intensity of the A_2, $I = \langle \hat{A}_2^\dagger \hat{A}_2 \rangle$, which corresponds to the photon number operator, as discussed in Ch. 2. This is an ideal model for the photodiode where we have a one-to-one correspondence between the photon number and the electrons in the photocurrent diode [111]. The linearized photocurrent I from the optical field, $\hat{A}_2$, can be written as,

$$I = \langle \hat{A}_2^\dagger \hat{A}_2 \rangle = \eta_D \langle \hat{A}_2 \rangle^2 + \sqrt{\eta_D} \langle \hat{A}_2 \rangle (\sqrt{\eta_D}\ \delta \hat{X}_2^\dagger + \sqrt{1-\eta_D}\ \delta \hat{X}_v^\dagger), \tag{6.2}$$

where $\delta \hat{X}_2^\dagger = \delta A_2^\dagger + \delta A_2$, η_D is the detector efficiency and $\delta \hat{X}_v^\dagger$ are the vacuum fluctuation that couple in due to the losses. We are assuming that the quadratic in fluctuation is negligible. The first term is the DC photocurrent and the second term represents the

intensity fluctuations. This second term represents one for feedforward to modulate the amplitude of the optical field, $\hat{A}_1$. We denote the amplified intensity fluctuations from the measurement of the $\hat{A}_2$ field as that $\delta\hat{X}^{\dagger}_{EOM}$. Then, the final output, $\hat{A}_f$, is related to the input field and feedforward signal according to

$$\begin{aligned}\hat{A}_f &= \hat{A}_1 - \frac{1}{2}\delta\hat{X}^{\dagger}_{EOM} \\ &\rightarrow \sqrt{\eta_E}\hat{A}_1 + \sqrt{1-\eta_E}\ \delta\hat{v} - \frac{1}{2}\delta\hat{X}^{\dagger}_{EOM},\end{aligned} \tag{6.3}$$

where η_E is the efficiency of the EOM, and $\delta\hat{v}$ are the vacuum fluctuations. The factor of 1/2 is chosen to simplify the calculations of the power spectrum of the field after the feedforward. To understand the effect of the feedforward, we need to calculate $\delta\hat{X}^{\dagger}_{EOM}$, which is given by the convolution of the field fluctuation and the response of the electronic feedforward loop $k(t)$ with the total detection time T, that is

$$\delta\hat{X}^{\dagger}_{EOM} = \sqrt{\eta_D}\langle\hat{A}_2\rangle \int_0^T k(\tau)\big[\sqrt{\eta_D}\ \delta\hat{X}^{\dagger}_2(t-\tau) + \sqrt{1-\eta_D}\ \delta\hat{X}^{\dagger}_v(t-\tau)\big]d\tau. \tag{6.4}$$

Through a Fourier transform from time to frequency, we can obtain the fluctuations in the frequency domain for $\hat{A}_f$ to be of the form

$$\delta\tilde{A}_f = \sqrt{\eta_E}\ \delta\tilde{A}_1 + \sqrt{1-\eta_E}\ \delta\tilde{v} - \frac{1}{2}\sqrt{\eta_D}\ g\ (\sqrt{\eta_D}\ \delta\tilde{X}^{\dagger}_2 + \sqrt{1-\eta_D}\ \delta\tilde{X}^{\dagger}_v), \tag{6.5}$$

where g is defined as $k(\omega)\langle\hat{A}_2\rangle$, which is related to the gain of the amplifier and electronic loop. To evaluate the noise of the beam after feedforward, we calculate the power spectrum, S, of the fluctuations of the field. The power spectrum normalized to the corresponding shot noise is given by $\langle\delta\tilde{X}^{\dagger}\delta\tilde{X}\rangle$. Therefore, S become 1 for coherent light.

From Eq. (6.5), we can derive the noise spectrum of the output beam, S_f by expanding $\delta\hat{X}^\dagger = \delta\hat{A}^\dagger + \delta\hat{A}$ and using the relation $\langle(\delta\tilde{X_1} - \delta\tilde{X_2})^2\rangle = \langle\delta\tilde{X_1}^\dagger\delta\tilde{X_1}\rangle + \langle\delta\tilde{X_2}^\dagger\delta\tilde{X_2}\rangle - \langle\delta\tilde{X_1}^\dagger\delta\tilde{X_2}\rangle - \langle\delta\tilde{X_2}^\dagger\delta\tilde{X_1}\rangle$. By assuming that $\langle\delta\tilde{X_1}^\dagger\delta\tilde{X_1}\rangle$ and $\langle\delta\tilde{X_2}^\dagger\delta\tilde{X_2}\rangle$ are the same, the noise fluctuation spectrum after feedforward becomes

$$S_f = (\eta_E + \eta_D^2 g^2 - 2\eta_D g\sqrt{\eta_E})S_1 + (1-\eta_E) + \eta_D(1-\eta_D)g^2 + 2\eta_D g\sqrt{\eta_E}S_{1-2}, \quad (6.6)$$

where S_1 is the single beam noise and S_{1-2} is the intensity difference noise between $\hat{A}_1$ and $\hat{A}_2$ given by $\langle(\delta\tilde{X_1} - \delta\tilde{X_2})^2\rangle$. Since the gain can be optimized for minimum noise, we can calculate the optimized gain to be given by

$$g_{opt} = \sqrt{\eta_E}\frac{(S_{1-2} - S_1)}{(1-\eta_D) + \eta_D S_1}. \quad (6.7)$$

The noise spectrum with optimum gain becomes,

$$S_{f,opt} = (1-\eta_E) + \eta_E S_1 - \eta_D\eta_E\frac{(S_1 - S_{1-2})^2}{(1-\eta_D) + \eta_D S_1}, \quad (6.8)$$

where $S_{f,opt}$ is the prediction for the noise after the feedforward. The first part, $(1-\eta_E) + \eta_E S_1$, of the equation describes the probe beam fluctuations coupled with the vacuum noise introduced due to imperfect transmission through the EOM, while the other part of the equation describes the cancellation of the noise due to the measurements of intensity fluctuation of A_2.

If we have perfect correlations without any losses, and the excess noise of each beam is large ($S_1 \gg 1$), then the noise output will be $S_{f,opt}$=2 S_{1-2}, which is half of the initial noise reduction from the twin beam. This is due to the fact that we are measuring the

intensity of A_2, which corresponds to a loss of 3 dB (half of the beam) with respect to the initial squeezing.

We want to note that twin beams generated with the FWM process have high intensity and a high degree of quantum correlations between the two modes. This is advantageous for generating single-mode amplitude squeezed light because detectors for high intensity beams are generally more efficient than ones used for low photon flux. Thus, the large degree of correlations can be efficiently used to reduce the noise of one of the other beams by feedforwarding the fluctuation measurements of the other mode [110, 109]. Since two-mode squeezed light from FWM has been shown near -9 dB of squeezing, theoretically, with feedforward it is possible to generate a single-mode squeezed state with -6 dB of squeezing.

6.2 Experimental Results

The feedforward technique requires fast intensity modulation done by an AOM or an EOM. In general, it is easier to do fast modulation with an AOM because an EOM requires high voltage for its modulation. However, the response of the EOM is faster than the one of the AOM because the AOM is modulated by sound waves and the EOM is modulated by electric field. Implementing amplitude modulation from with an EOM requires an electro-optic crystal and a PBS. When an electric field is applied to the electro-optic crystal, the crystal changes the polarization of the light transmitted through the EOM. The polarization rotation of the light is transferred to a change in

the intensity by the PBS. The bandwidth of the EOM is tens of MHZ, so light can be modulated within that bandwidth.

We implement feedforward to two different configurations, one in which the probe beam is off-resonance and the other in which it is on-resonance. We first generate bright two-mode squeezed states of light using a non-degenerate FWM process in a double-lambda configuration in the D1 line of ^{85}Rb, as explained in Ch. 4,

Figure 6.3 shows the schematic of the experimental setup for the feedforward along with the setup for generating two-mode squeezed light with FWM. We add an optical delay line to compensate for the delay introduced by the electronics. As can be seen in the figure, a photodiode converts the intensity fluctuations of the conjugate to current fluctuations, which are then amplified and sent to the EOM. The amplified intensity fluctuation signal is used to modulate the transmission through the EOM with 88% transmission. Since the intensity fluctuations of the probe and the conjugate are quantum correlated, the probe beam after the feedforward has reduced the intensity noise below the QNL.

We consider two different configurations for the feedforward technique: the probe beam is on exact resonance or off-resonance with the D1 $F = 2$ to $F' = 2$ transition of ^{87}Rb. For both configurations, we take a portion of the probe beam and send it to a saturated absorption spectroscopy setup to measure the absolute frequency of the probe beam, as shown in Fig. 6.3.

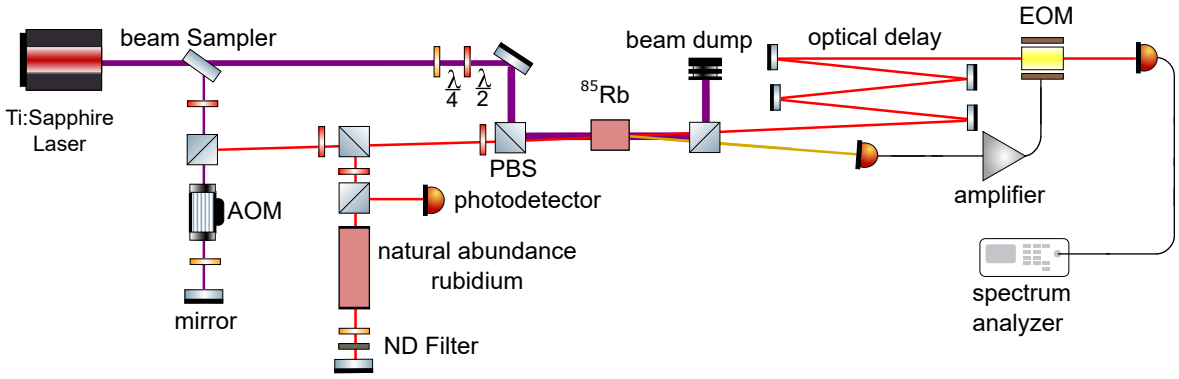

Figure 6.3: Simplified schematic of the experimental setup for feedforward. The pump and probe beams intersect inside a ^{85}Rb vapor cell. After the FWM process, the pump beam is filtered with a PBS. The conjugate light is measured and the measured signal is amplified with an electronic amplifier. The amplified signal is used to modulate the intensity of the probe that is transmitted through the EOM in order to feedforward on its noise and reduce it. A saturated absorption spectroscopy setup is used measure the absolute frequency of the probe beam. Copyright (2019) by Optica Publishing Group. Reprinted with permission [112].

6.2.1 Off-Resonance Configuration

We first consider the off-resonance configuration from Sect. 3.3 where the probe beam is off-resonant with the D1 $F = 2$ to $F' = 2$ transition of ^{87}Rb, as shown in Fig. 4.1(a) in Sect. 4.2. The one-photon detuning is 800 MHz to the blue of the D1 transition of ^{85}Rb. The optimum level of squeezing is obtained for an angle θ of 0.5°, pump power and $1/e^2$ diameter of 300 mW and 1.3 mm, respectively, probe diameter of 0.9 mm, a vapor cell temperature of 107°C, and a two-photon detuning δ of 2 MHz. We find an intensity difference squeezing level of −7.6 dB at an analysis frequency of 360 kHz

after subtracting the electronic noise.

After the generation of the two-mode squeezed light, we feedforward the fluctuation measurements from the conjugate beam to the probe beam as described in Fig. 6.3. During the feedforward process, electronics used for feedforward have a finite time response that introduces a time delay introduced on the signal of the conjugate fluctuations. A delay in the time domain translates to a phase shift in the frequency domain that effectively makes the sign of the feedforward gain oscillate as a function of frequency. This would result in a probe noise level after the feedforward that oscillates between the probe-conjugate intensity-difference and intensity-sum noise levels. Thus, if the electronic delay is not compensated, the noise spectrum of the probe after feedforward will oscillate between squeezing and excess noise. In order to compensate for the delay, we optimize the optical delay line before sending it through the EOM, as shown in Fig. 6.3. We find the optimum optical path to be 21.7 m, which represents a delay of $\approx$72 ns. After feedforward, we obtain a single-mode squeezed state with an intensity squeezing level of -2.9 dB at an analysis frequency of 360 kHz after subtracting the electronic noise.

By using the optimum gain for the EOM modulation that minimizes the intensity fluctuation, we can obtain the theoretical prediction of intensity fluctuation S_f after feedforward, as given by Eq. (6.8) in Sect. 6.1. For the prediction, we used measured efficiency of the EOM (η_{EOM}= 88%) and quantum efficiency of the photodiode (η_D= 95%).

Using Eq. (6.8), we obtain a theoretical predicted squeezing level of -3.0 dB after

the feedforward for measurements at an analysis frequency of 360 kHz, which is in good agreement with the experimental measurements. We have larger loss in the level of squeezing than the ideal 3 dB due to the high transmission loss from the EOM. We believe that this can be resolved to increase the squeezing level to -3.6 dB by implementing the feedforward through a displacement operation by combining the probe beam with a strong coherent state on a highly reflecting (99/1) BS [113].

Figure 6.4 shows the measured intensity noise spectra after subtracting the electronic noise and normalization to the corresponding shot noise. This figure shows the noise traces for the single-mode squeezed light obtained from the feedforward are shown with optical delay (black trace) and without optical delay (grey trace), the noise traces for the conjugate before the feedforward (purple trace), the QNL (green trace), and the initial squeezing of the twin beams (blue trace).

Without optimizing the optical delay, we obtain single-mode squeezing in the low frequency region, as the noise increases as the frequency increases due to the phase factor from the time delay. Given the time delay, we are expecting the oscillation from the intensity difference to the intensity sum to happened at 13.8 MHz. Since we are only looking at a frequency range of 3 MHz, we do not see the full oscillation and only observe the increasing part of the noise trace. With compensation of the optical delay, the noise of the single-mode squeezed state is in good agreement with the predicted value after feedforward, and we observe squeezing from at least 200 kHz to over 2.2 MHz. However, we still observe that the noise increases as the frequency increases. We believe that this is a result of an increase in the electronic noise of the

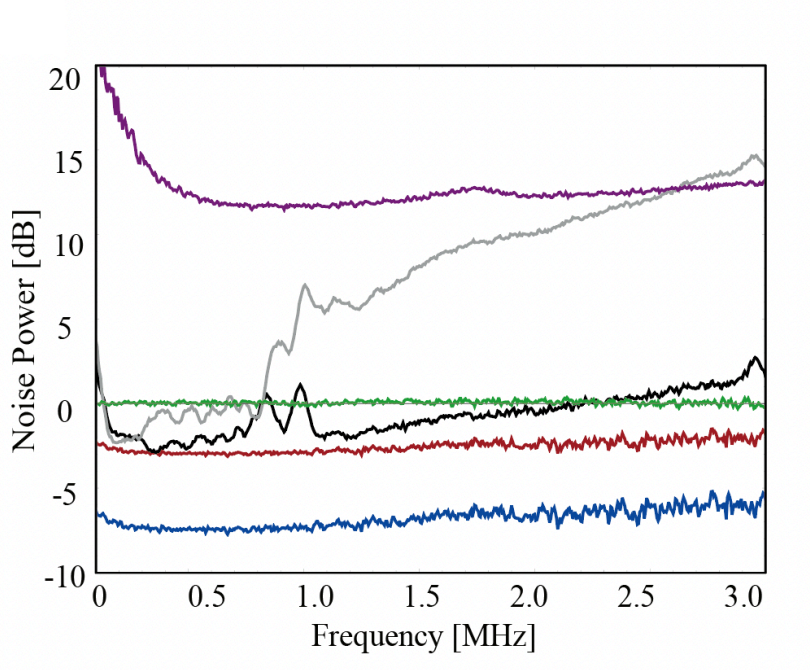

Figure 6.4: Intensity noise spectra for the off-resonance FWM. Each trace represents: the single beam noise from the conjugate (purple trace), the shot noise limit (green trace), the single beam noise of the probe after feedforward with optical delay (black trace), without optical delay (grey trace), intensity difference (blue trace), and the predicted single beam noise after the feedforward (red trace). For these measurements, the electronic noise has been subtracted and the spectrum analyzer was set to a resolution bandwidth of 30 *kHz and a video bandwidth of* 100 *Hz with 10 averages. Copyright (2019) by Optica Publishing Group. Reprinted with permission [112].*

detector as the frequency approaches the bandwidth of the detector (4 MHz). The noise traces from the feedforward in both cases, with and without delay, have a peak around 1 MHz, which is due to a piezo-electric resonances of the EOM.

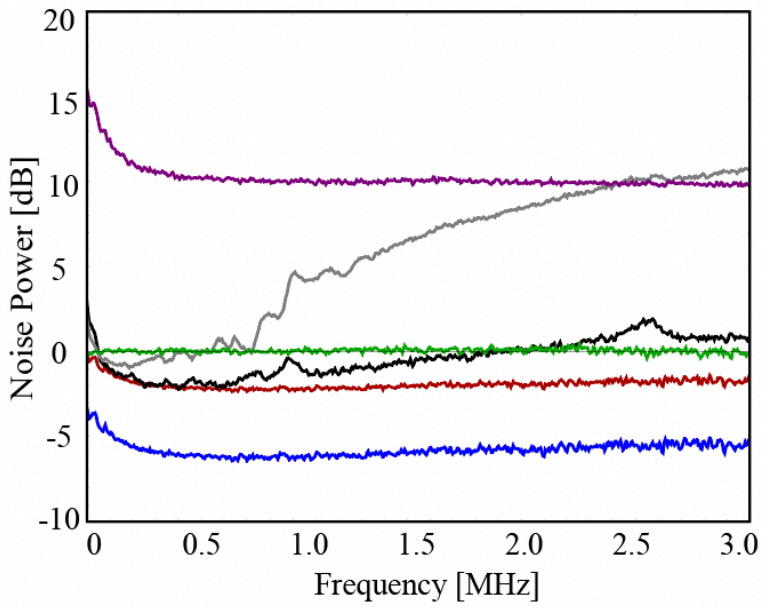

Figure 6.5: Intensity noise spectra for the probe on-resonance with the D1 $F = 2$ to $F' = 2$ transition of ^{87}Rb. Copyright (2019) by Optica Publishing Group. Reprinted with permission [112].

6.2.2 On-Resonance Configuration

The feedforward technique to produce off-resonant single-mode squeezed light can be implemented to produce on-resonance squeezed light with the configuration shown in Fig. 4.1(b) in Sect. 4.2. In this configuration, the one-photon detuning is set to produce a probe resonant with the D1 $F = 2$ to $F' = 2$ transitions in ^{87}Rb; the two-photon detuning is optimized to obtain the maximum level of squeezing with δ of 8 MHz. The optimum level of squeezing is obtained with an angle θ of 0.4°, pump power and diameter of 750 mW and 1.3 mm, respectively, probe diameter of 0.9 mm, and a vapor

cell temperature of 90°C.

The optimum optical delay path for the conjugate beam is 19.6 m which represents a delay of ≈65 ns. There is a slight different optical path length due to the different delay from the FWM processes operating at a different detuning. The FWM in the double-lambda introduces a delay in the probe beam with respect to the conjugate beam [114], which we find experimentally to be of ≈7 ns for the off-resonant configuration by optimizing the squeezing with an electronic delay. However, the delay is negligible for the on-resonance case, so we can estimate the delay from the electronics to be ≈65 ns. After feedforward, we obtain a single-mode squeezed state with an intensity squeezing level of −2.1 dB at an analysis frequency of 360 kHz. After subtracting the electronic noise, the theoretical predicted squeezing is of −1.9 dB, which is in good agreement with the measurement.

Figure 6.5 shows the measured intensity noise spectra for single-mode resonant squeezed light. Similar to the off-resonant case, without optimizing the optical delay, we can only obtain single-mode squeezing in the low frequency region of the spectrum, and the noise increases as the frequency increases. Given the time delay, we are expecting an oscillation from the intensity difference to the intensity sum at a frequency of 15.4 MHz. With the optimized optical delay, we observe squeezing from at least 200 kHz to over 2.0 MHz, which is a slightly small range compared with the off-resonant configuration due to the smaller amount of initial squeezing for the resonant configuration.

It is also possible to obtain single-mode squeezing with tunability. Previous papers showed that it is possible to obtain off-resonance two-mode squeezing over a region of

more than 1 GHz [115] and on-resonance two-mode squeezing over a region of the order of 500 MHz [12]. The tunability of the two-mode squeezed light can be transferred to the single-mode squeezed light to make it possible to generate squeezed state of light on-resonance with the D1 $F = 1$ to $F' = 1$ transitions in ^{87}Rb with the feedforward technique.

6.3 Conclusion

In this chapter, we have demonstrated the generation of bright single-mode squeezed light using a non-degenerate FWM process in the D1 line of ^{85}Rb through the use of a feedforward technique. We obtained an intensity squeezing of -2.9 dB when we tune to off-resonance. For the resonance configuration, in which the probe is on-resonance with the $F = 2$ to $F' = 2$ transitions in the D1 line of ^{87}Rb, we obtained -2.1 dB of intensity squeezing.

The feedforward technique in combination with the FWM process can offer a larger level of single-mode squeezing on atomic resonance compared to squeezed light generated with other atomic process such as polarization self-rotation [67], the feedforward technique overcomes several experimental difficulties associated with crystal-based sources as discussed in Sec. 4.2. In addition, resonant squeezed states have bandwidths of the order of the atomic natural linewidth and high intense light [113], which is particularly applicable for experiments based on direct intensity measurements [109].

Chapter 7

Generation of Scalable Genuine Multipartite Gaussian Entanglement With a Parametric Amplifier Networks

I am the light of the world. Whoever follows me will never walk in darkness, but will have the light of life.

- John the Apostle, *John 8:12*

In Sect. 2.2.2, we discussed entanglement in a pure two-mode squeezed state and introduced a way to characterize entanglement using the PPT criteria. However, for a system with more than two modes, entanglement is more complex than for the bipartite case and as a result its characterization becomes more difficult. For a system with n mode, if its state can be written as

$$\rho_{1,2,..,n} = \sum_m c_m \ \rho_1^m \otimes \rho_2^m \otimes ... \otimes \rho_n^m, \tag{7.1}$$

then it is a fully separable state [116].

In multipartite entanglement, states that have the strongest form of non-locality are said to have genuine multipartite entanglement (GME). This inseparable state is considered a valuable resource for quantum information science [117]. For example, it has been proposed as a resource for teleportation and dense coding [118], to enhance the rate of quantum key distribution [119], and to reach the highest sensitivities in quantum interferometry [120, 121].

Previously in Ch. 4 and Ch. 5, we have shown that FWM offers advantages over other systems for the generation of quatnum state of light, such as the possibility of enabling efficient interactions with atomic systems. If we can create a state with GME based on the FWM process, it can be a building block for quantum technology. Therefore, in this final chapter, we theoretically propose a novel method for generating GME based on PA networks and outline a possible experimental implementation. We first describe how to characterize GME using the PPT criteria, then introduce our theoretical proposal and conclude with the proposed experimental setup [122]

7.1 Verification of Genuine Multipartite Entanglement

In Sect. 2.2.2. we showed how to determine the presence of entanglement in the two-mode case. If we cannot write the system with two independent quantum systems, the system has entanglement. In the multipartite system, if the system cannot be written as tensor product of bipartite states in any bipartition, the system has GME. We can use of the PPT criteria to verify that the system was a bipartite inseparable state. With the PPT criteria, if we verify that system is not bipartite, we can conclude that the system has GME.

Figure 7.1 shows all possible bipartitions for different systems with different number of modes. For the three-mode case, we need to perform three PPT tests to determine if our system has GME. However, for the four-mode case, the verification process becomes more complicated. Here, it takes a total 7 PPT criteria to show that four modes have

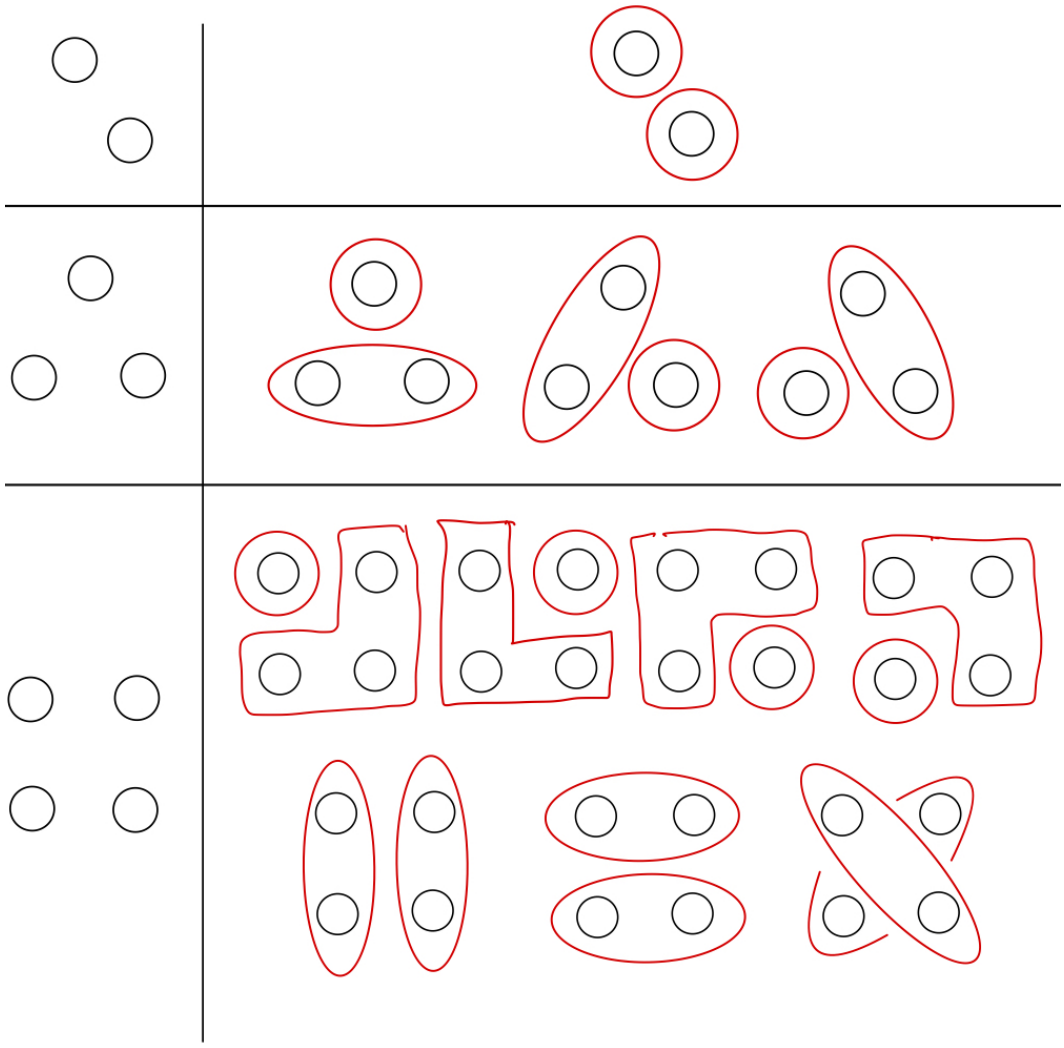

Figure 7.1: Total possible ways of bipartition in two, three, and four modes system. Shapes with red-lines are used to show two bipartite regions in each case.

GME. We must first check the bipartitions composed of one mode and the other three modes, as well as bipartitions composed of two modes and the remaining other two. The number of required test for a given number of modes can be counted using all possible combinations,

$$ {}^{n}C_{k} = \frac{n(n-1)(n-2)\cdots(n-k+1)}{k(k-1)\cdots 1}. \tag{7.2} $$

2	3	4	5	6	7	8	9	10	11	12	13	14	n
1	3	7	15	31	63	127	255	511	1023	2047	4095	8191	$2^{N-1}-1$

Table 7.1: Required number of the PPT criteria that need to be verified for an N-mode system.

where n is the total modes in the system and k is the selected number of modes in one of the partition. For example, if we consider bipartitions composed of one mode in one bipartition and three modes in the other, we are checking for 1X3 separability, where n is equal to 4 and k is equal to 1.

In 1X3 separability, there are ${}^4C_1 = 4$ ways of bipartitioning the four modes, and for 2X2 separability there are ${}^4C_2/2 = 4/2$ ways of bipartitioning. Note that we need to divide by 2 to avoid double counting for the symmetric bipartitions. The sum of all possible ways to bipartition an N-mode system, derived in Appendix B.1,is $2^{N-1}-1$. We can see that this number increases exponentially with N. The number of required PPT criteria that need to be verified to show GME is shown in Table 7.1. To verify GME for an N-mode Gaussian system for electric field quadratures, we first need to construct the CM, $\sigma = \langle \xi \xi^T \rangle$. For a multipartite system, ξ is the N-mode element vector $\xi = [\hat{X}_1, \hat{Y}_1, \hat{X}_2, \hat{Y}_2, \hat{X}_3, \hat{Y}_3, \hat{X}_4, \hat{Y}_4 ... \ \hat{X}_n, \hat{Y}_n]$, such that it contains the quadratures $\hat{X}$ and $\hat{Y}$ for each mode. As discussed in Sect. 2.2.2, a physical CM must

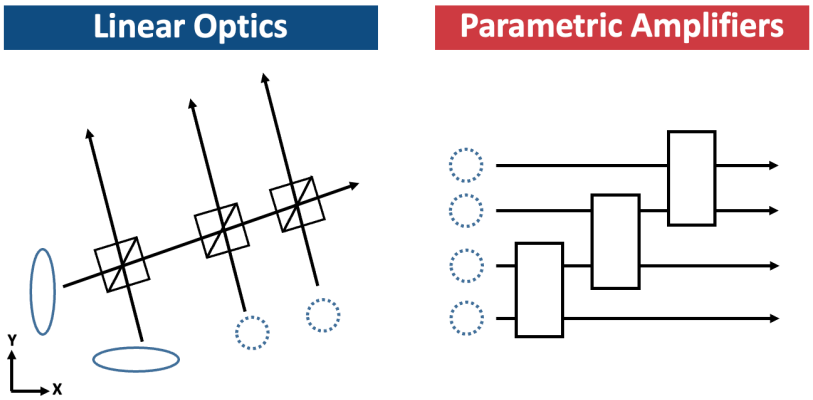

Figure 7.2: (left) GME generation using a single-mode squeezed state and beamsplitters. The larger number of beamsplitters, the larger the number of entangled modes. (right) GME generation using cascaded parametric amplifiers. Similar to the beamsplitter method, adding more parametric amplifiers increases the number of entangled modes.

satisfy $\sigma + i\Omega \geq 0$ [27], where the symplectic matrix Ω for N-modes takes the form

$$\Omega = \bigoplus_{j=0}^{N} J, \quad J = \begin{pmatrix} 0 & -1 \\ 1 & 0 \end{pmatrix}. \tag{7.3}$$

Here, the difference between the two-mode and the N-mode systems is that we need to check that all possible bipartitions are inseparable through the PPT criteria [29] to show that our system has GME.

7.2 Generation of Genuine Multipartite Entanglement

Multi-mode GME has been realized experimentally [123, 124] and there are proposals to scale it up to higher number of modes through the use of BS arrays [29, 125] or

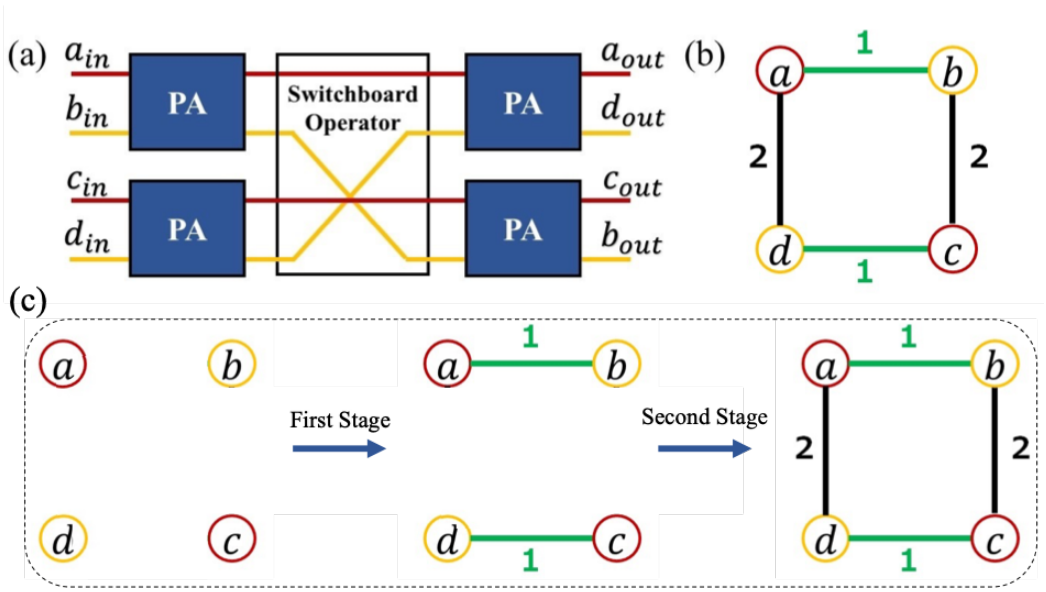

Figure 7.3: (a) Schematic of proposed system to generate genuine quadripartite entangled states. (b) Graphical representation of connections between the modes in the quadripartite state generated with the proposed scheme and (c) connections introduced by the first and the second stages of network. PA: parametric amplifier.

PA arrays [126, 127], as shown in Fig. 7.2. Although these approaches are simple and straightforward, the transmission loss from the BSs or the PAs increase as the number of modes increases.

To overcome this limitation, Fig. 7.3 shows our proposal for the use of a two PA stages to realize quadrapartite GME. Our model connects all the modes through two stages of PAs shown as blue boxes and a switchboard operation that swap modes. To make it easier to recognize each mode, we marked the probe and conjugate red and yellow, respectively, for each PA in Fig. 7.3(a), and represent the connections introduced by the first and the second stage with green and black lines, respectively

in Fig. 7.3(b). We show how each mode is connected through the first and the second stage of PAs in Fig. 7.3(c). The first stage introduces pair wise connections, are marked with green line, then the second stage completes the missing connections marked in black.

Our proposal does not require large array of optics as we increase the number of modes, as we will show throughout the chapter. This reduces the complexity of system. We will show that our approach is easier to work with and extended to a large number of modes with GME, as it is easy to track the correlations between the different modes.

7.2.1 Quadrapartite Genuine Multipartite Entanglement

To show the presence of GME in the state generated using our proposed system, we first need to construct the CM of the quadrapartite system shown in Fig. 7.3(a). The general form of the CM in this case, assuming input vacuum states to the two input PAs, is an 8×8 matrix, as shown in Eq. (7.4), where $\sigma = \left\langle \xi\xi^T \right\rangle$ with the quadrature vector organized as $\xi = [\hat{X}_a, \hat{Y}_a, \hat{X}_b, \hat{Y}_b, \hat{X}_c, \hat{Y}_c, \hat{X}_d, \hat{Y}_d]$,

$$\sigma_4 = \begin{pmatrix} \left\langle \hat{X}_a^2 \right\rangle & 0 & \left\langle \hat{X}_a\hat{X}_b \right\rangle & 0 & \left\langle \hat{X}_a\hat{X}_c \right\rangle & 0 & \left\langle \hat{X}_a\hat{X}_d \right\rangle & 0 \\ 0 & \left\langle \hat{Y}_a^2 \right\rangle & 0 & \left\langle \hat{Y}_a\hat{Y}_b \right\rangle & 0 & \left\langle \hat{Y}_a\hat{Y}_c \right\rangle & 0 & \left\langle \hat{Y}_a\hat{Y}_d \right\rangle \\ \left\langle \hat{X}_a\hat{X}_b \right\rangle & 0 & \left\langle \hat{X}_b^2 \right\rangle & 0 & \left\langle \hat{X}_b\hat{X}_c \right\rangle & 0 & \left\langle \hat{X}_b\hat{X}_d \right\rangle & 0 \\ 0 & \left\langle \hat{Y}_a\hat{Y}_b \right\rangle & 0 & \left\langle \hat{Y}_b^2 \right\rangle & 0 & \left\langle \hat{Y}_b\hat{Y}_c \right\rangle & 0 & \left\langle \hat{Y}_b\hat{Y}_d \right\rangle \\ \left\langle \hat{X}_a\hat{X}_c \right\rangle & 0 & \left\langle \hat{X}_b\hat{X}_c \right\rangle & 0 & \left\langle \hat{X}_c^2 \right\rangle & 0 & \left\langle \hat{X}_c\hat{X}_d \right\rangle & 0 \\ 0 & \left\langle \hat{Y}_a\hat{Y}_c \right\rangle & 0 & \left\langle \hat{Y}_b\hat{Y}_c \right\rangle & 0 & \left\langle \hat{Y}_c^2 \right\rangle & 0 & \left\langle \hat{Y}_c\hat{Y}_d \right\rangle \\ \left\langle \hat{X}_a\hat{X}_d \right\rangle & 0 & \left\langle \hat{X}_b\hat{X}_d \right\rangle & 0 & \left\langle \hat{X}_c\hat{X}_d \right\rangle & 0 & \left\langle \hat{X}_d^2 \right\rangle & 0 \\ 0 & \left\langle \hat{Y}_a\hat{Y}_d \right\rangle & 0 & \left\langle \hat{Y}_b\hat{Y}_d \right\rangle & 0 & \left\langle \hat{Y}_c\hat{Y}_d \right\rangle & 0 & \left\langle \hat{Y}_d^2 \right\rangle \end{pmatrix}$$

$$= \begin{pmatrix} \alpha_+\beta_+ & 0 & \alpha_-\beta_+ & 0 & \alpha_-\beta_- & 0 & \beta_-\alpha_+ & 0 \\ 0 & \alpha_+\beta_+ & 0 & -\alpha_-\beta_+ & 0 & \alpha_-\beta_- & 0 & -\beta_-\alpha_+ \\ \alpha_-\beta_+ & 0 & \alpha_+\beta_+ & 0 & \beta_-\alpha_+ & 0 & \alpha_-\beta_- & 0 \\ 0 & -\alpha_-\beta_+ & 0 & \alpha_+\beta_+ & 0 & -\beta_-\alpha_+ & 0 & \alpha_-\beta_- \\ \alpha_-\beta_- & 0 & \beta_-\alpha_+ & 0 & \alpha_+\beta_+ & 0 & \alpha_-\beta_+ & 0 \\ 0 & \alpha_-\beta_- & 0 & -\beta_-\alpha_+ & 0 & \alpha_+\beta_+ & 0 & -\alpha_-\beta_+ \\ \beta_-\alpha_+ & 0 & \alpha_-\beta_- & 0 & \alpha_-\beta_+ & 0 & \alpha_+\beta_+ & 0 \\ 0 & -\beta_-\alpha_+ & 0 & \alpha_-\beta_- & 0 & -\alpha_-\beta_+ & 0 & \alpha_+\beta_+ \end{pmatrix}. \quad (7.4)$$

where $\alpha_\pm = (e^{-2s_1} \pm e^{2s_1})/2$ and $\beta_\pm = (e^{-2s_2} \pm e^{2s_2})/2$.

The PPT criteria for all the bipartitions of the form 1×3 (a|bcd, b|acd, c|abd, d|abc) is identical due to the symmetry of the graphical representation, as seen in Fig. 7.4(a),

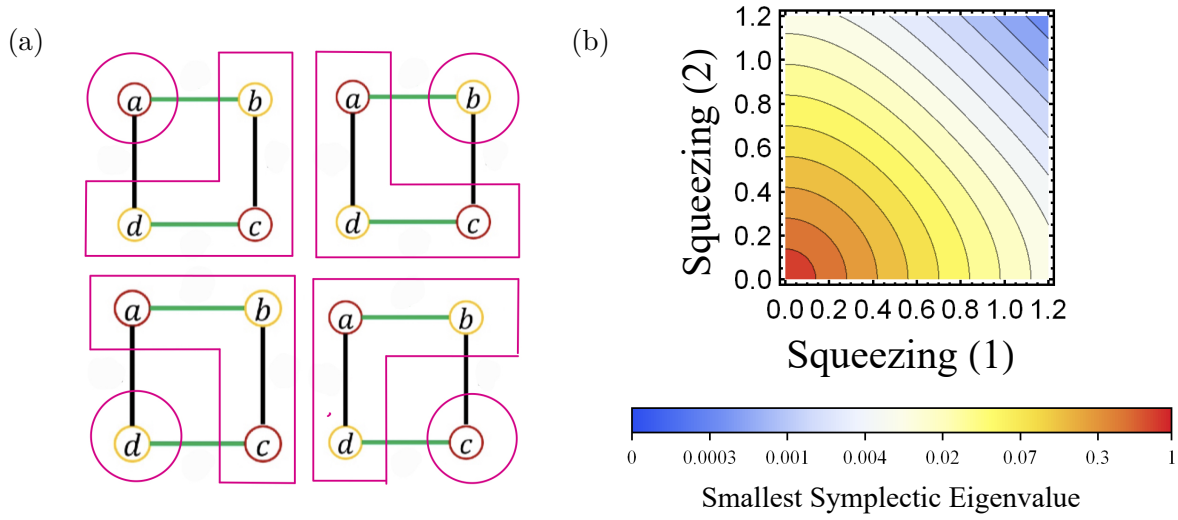

Figure 7.4: (a) Graphical representation of all the 1×3 bipartitions for the four-mode case. (b) Contour plot of the smallest symplectic eigenvalues with respect to the gains of the two stages of the PA network.

and takes the form

$$\begin{aligned}\Delta^{(1\times3)} = {} & \alpha_-^2\left(\beta_+^2-\beta_-^2\right)+\alpha_+^2\left(\beta_-^2+\beta_+^2\right) \\ & -2\alpha_+\beta_+\sqrt{\alpha_-^2\left(\beta_+^2-\beta_-^2\right)+\alpha_+^2\left(\beta_-^2+\beta_+^2\right)-\alpha_+^2\beta_+^2},\end{aligned} \tag{7.5}$$

where $\Delta^{(1\times3)}$ is the smallest symplectic eigenvalue of the PPT matrix, $\Delta \equiv -(\widetilde{\Omega}\sigma)^2 \geq 1$ shown in Sect. 2.2.2, for verifying 1X3 separability. In the PA process, two-mode squeezing operation can be characterized by s and θ, as shown in Ch. 2. We set the phase of each PA to $\theta = 0$ to maximize the amplification process and denote the squeezing parameters of the PAs of the first and second stages as s_1 and s_2, respectively. Figure 7.4(b) shows the contour plot of the smallest symplectic eigenvalue, $\Delta^{(1\times3)}$, with respect to the squeezing parameters for the first and the second stages. As can be seen

in Fig. 7.4(a), all the bipartitions have the exact same connections given by the green and black lines, which corresponds to the first and second stage of PAs.

The bipartitions of the form 2×2 are shown in Figs. 7.5(a) through (c), which correspond to the bipartitions ab|cd, ad|bc, and ac|bd. We calculate the criteria for these bipartition and find that they take the form $\left(\alpha_+^2 - \alpha_-^2\right)\left(\beta_- + \beta_+\right)^2$, $\left(\alpha_- + \alpha_+\right)^2\left(\beta_- + \beta_+\right)^2$, and $\left(\alpha_- + \alpha_+\right)^2\left(\beta_+^2 - \beta_-^2\right)$; respectively.

The bipartitions ab|cd and ad|bc shown in Figs. 7.5(a) and (b) become e^{-2s_2} and e^{-2s_1} are independent of the first stage and the second stage because $\left(\beta_+^2 - \beta_-^2\right) = 1$ and $\left(\alpha_+^2 - \alpha_-^2\right) = 1$. Unlike the bipartitions ab|cd and ad|bc, the bipartition ac|bd depends on the gain of both stages, as shown in Fig. 7.5(c). This is due to the connection from a to c requiring both stage of PA, which makes it the most entangled bipartition in the four-mode case.

For all bipartition, if we turn off all the PAs, we have $\alpha_+ = \beta_+ = 1$ and $\alpha_- = \beta_- = 0$, which implies that all the PPT criteria become 1. This implies that the system is always separable when there is no squeezing from any of the PAs. This is expected as turning off all the PAs implies that are no interactions between any of the four modes, and since the four modes are initially independent of each other, they do not violate any of the PPT criteria. When the squeezing parameters from both stages are greater than 0, the PPT criteria show that all the bipartitions are inseparable, as shown in Figs. 7.5 (d) through (f), which implies that the system is genuine quadrapartite entangled.

We want to note that the PPT criteria only works for a pure quantum state. In Appendix B.2, we introduce a stronger criteria that works for both pure and mixed

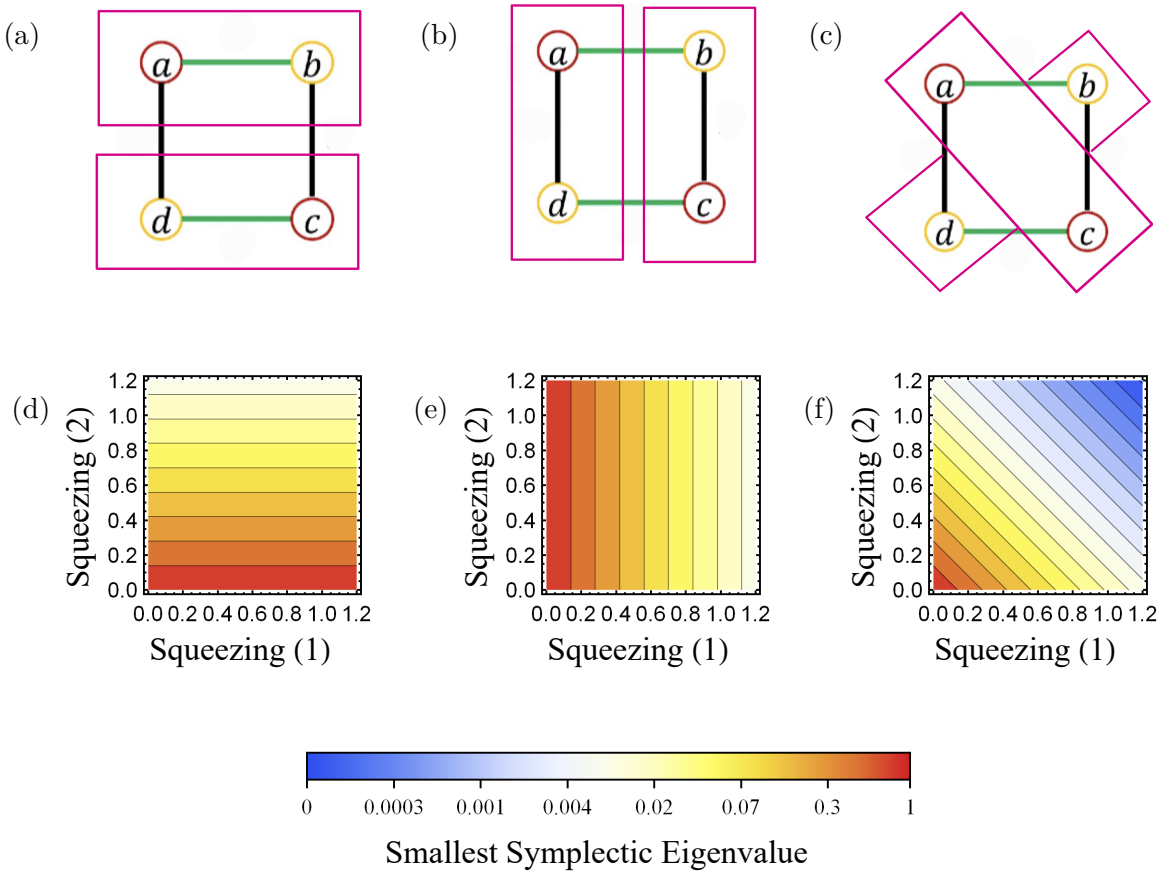

Figure 7.5: (a)-(c) Graphical representation of all the 2×2 bipartitions for the four-mode case and contour plots of the smallest symplectic eigenvalues (s.s.e.) with respect to the gains of the two stages for (d) ab|cd, (e) ad|bc, and (f) ac|bd.

states and show that the system is genuine quadrapartite entangled even with this stronger criteria.

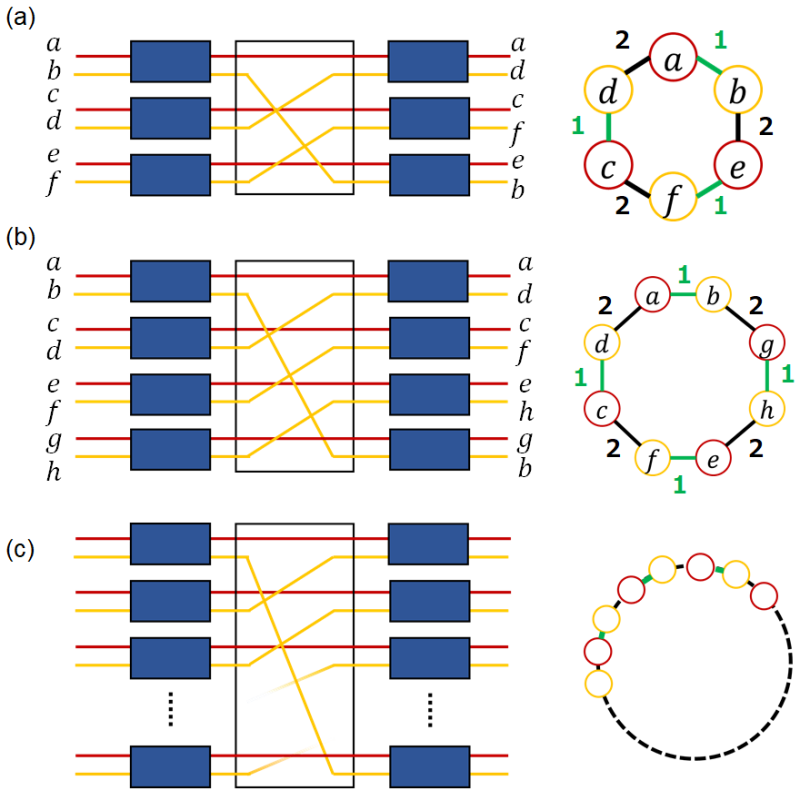

Figure 7.6: Schematic of the proposed scheme for the generation of (a) hexapartite entanglement and (b) octapartite entanglement with two-mode squeezers and a switchboard operation. Figures to the right give the graphical representation of the connections between modes. (c) Generalized of scheme to $2N$-partite case.

7.2.2 Hexapartite Genuine Multipartite Entanglement

One of the advantage of our proposed system is that it can easily be extended to more modes. In Fig. 7.6(a), we show how to generate a hexapartite GME through the proposed PA network. Note that for a hexapartite system, there are a total of $2^{6-1} - 1 = 31$ possible bipartitions. Figure 7.7(b) shows the PPT criteria for the 1×5 bipartitions [a|bcdef, b|acdef, c|abdef, d|abcef, e|abdf, f|abcde]. We simplify the system

by assuming that both stages have same squeezing parameter ($s_1 = s_2 = s$). Figures without this assumption are shown in Appendix B.3. As shown in Fig. 7.7(a), all the bipartitions of the 1×5 for the six-mode case are identical due to the symmetry in the connections between the bipartitions.

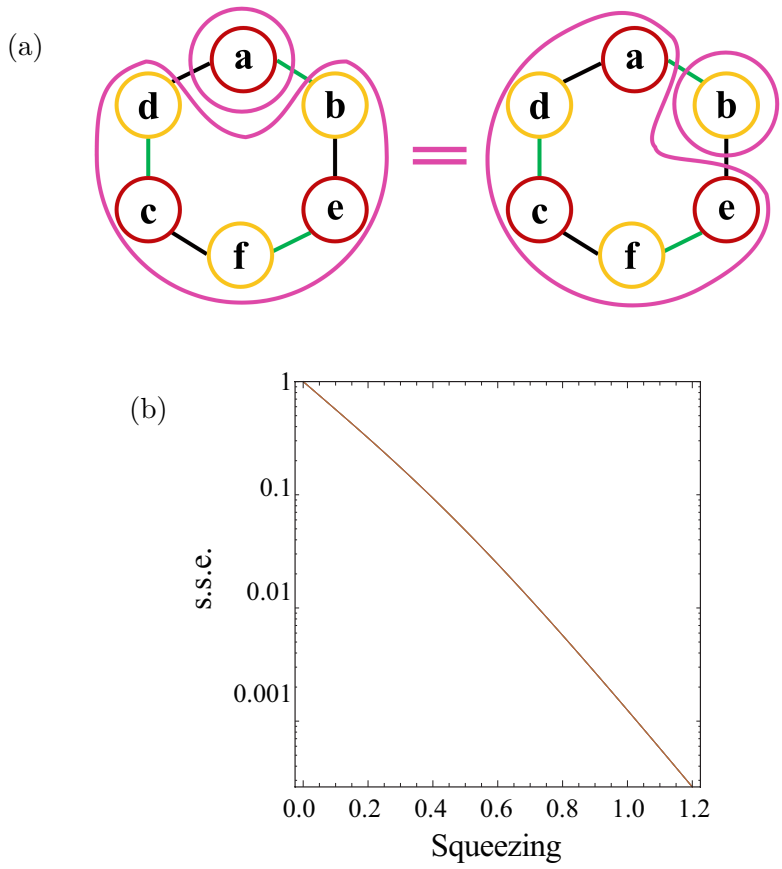

Figure 7.7: (a) Graphical representations of bipartition of form 1×5. (b) Smallest symplectic eigenvalues (s.s.e.) for the hexapartite entangled state with respect to the squeezing parameter ($s_1 = s_2 = s$) for bipartition of form 1×5.

Bipartitions of the form 2×4 and 3×3 are more complex, as shown in Fig. 7.8(d) and Fig. 7.9(e). For bipartitions of the form 2×4, there are four unique cases which

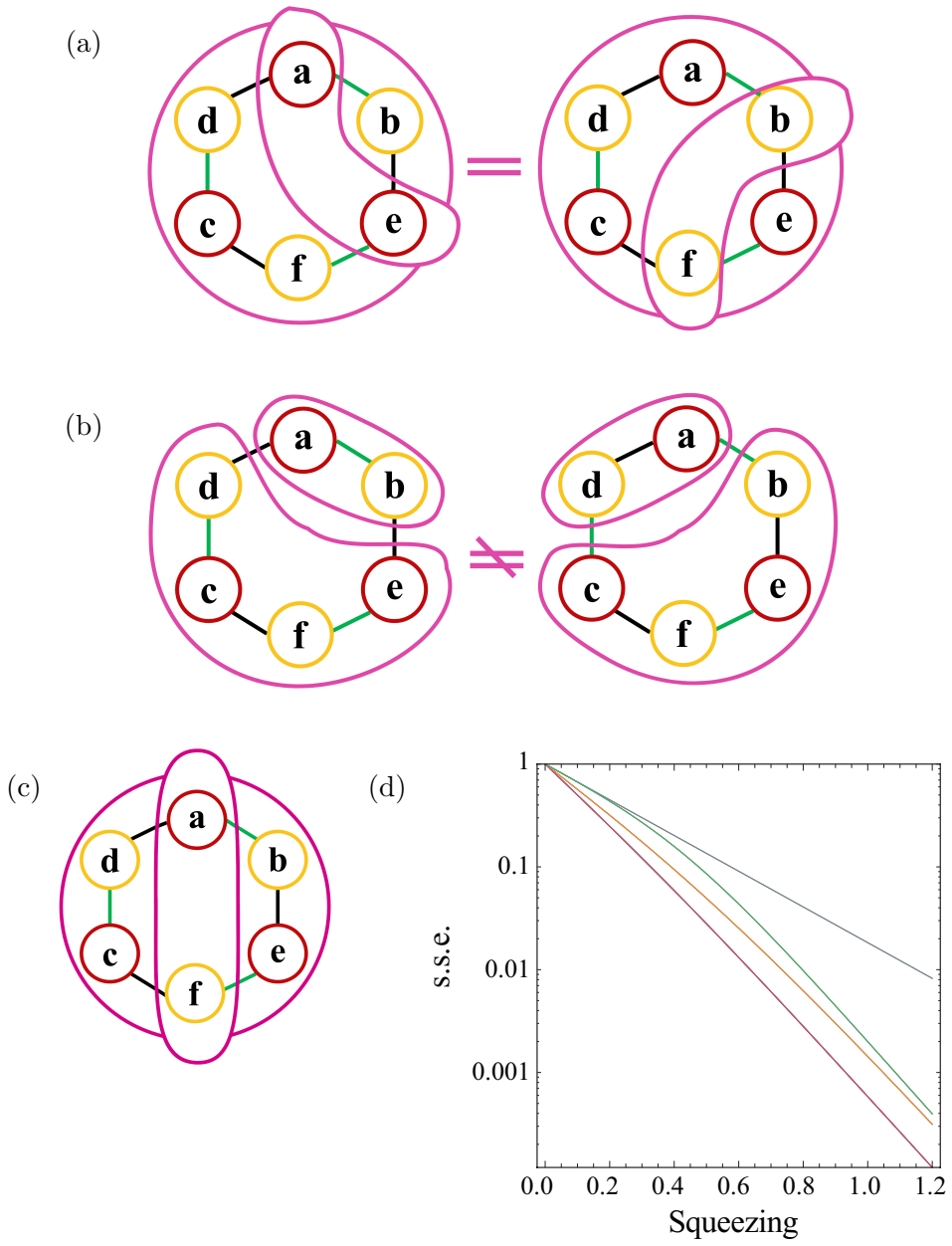

Figure 7.8: (a) through (c) Graphical representations of bipartition of form 2×4. (d) Smallest symplectic eigenvalues (s.s.e.) for the hexapartite entangled state with respect to squeezing parameter for bipartition of the form 2×4.

are shown in Figs. 7.8(a) through (c). In Fig. 7.8(d), the lowest traces (magenta) is for the bipartitions between second nearest neighbors and the rest of the system [ae|bcdf, bf|acde, ce|abdf, df|abce, ac|bdef, bd|acef], as shown in Fig. 7.8(a). A stronger violation indicates a stronger degree of entanglement between the two partitions, which means that the bipartitions between second closest neighbors and the rest of the system show the strongest entanglement for bipartitions of the form 2×4. For these partitions modes such as a and e are directly connected by a PA of the first stage and one of the second stage. Since we have a two stage direct connection, this results in the strongest connection. More or less PA processes will make the connection between two mode weaker.

The second-to-lowest trace (orange) corresponds to bipartitions [af|bcde, bc|adef, de|abcf] in which the elements of one of the partitions are connected by two PAs from the first stages and one from the second stage or by two from the second stage and one from the first stage, as shown in Fig. 7.8(c). Since these elements are not directly connected by two PAs, they exhibit weaker entanglement as compared to bipartitions shown in Fig. 7.8(a).

The last two traces, colored green and blue represent the final case of bipartitions shown in Fig. 7.8(b). These bipartitions are between nearest neighbors and the rest of the system, with the neighbors connected by a first stage PA [ab|cdef,ef|abcd,cd|abef] or a second stage PA [ad|bcef,be|acdf,cf|abde]. We find an interesting behavior in which partitions that have elements with nearest neighbors with a first stage connection, left diagram in Fig. 7.8(b), show more entanglement than ones with a second stage

connection, right diagram in Fig. 7.8(b). This can be understood by realizing that partitions described by the left diagram can be considered as an entangling operation by the first stage with added amplification noise by the second stage, but the partitions described by the right diagram can be considered as having amplification noise from the first stage and entangling by the second stage. We show in Appendix B.4 that entangling noisy state is better than making entangled states noisy.

We notice in Fig. 7.8(d) that the green trace initially follows the blue trace, then diverges and merges with the orange trace. This is because the connections between two stages begin to compete with each other and is dominated by one or the other. As we increase the squeezing, the second stage connection dominates over the first stage connection. Therefore, in the large squeezing limit, the first stage contribution decreases, and we can see that the nearest connection from the first stage [ab|cdef,ef|abcd,cd|abef] will converge to the second-to-lowest trace (orange) [af|bcde, bc|adef, de|abcf]. We show in Appendix B.4 that as we increase the squeezing, second stage connections lead to more entanglement then the first stage connections,

so if we in Fig. 7.8(b) If we remove the first level association and (c) the closest association with the first level [ab|cdef,ef|abcd,cd|abef] is the second-to-lowest trace (orange) [af|bcde, bc|adef, de|abcf].

For bipartitions of the form 3×3, there are also four unique cases, as shown in Fig. 7.9. In Fig. 7.9(e), the lowest trace (green) corresponds to partitions consisting only of second nearest neighbor (ace|bdf,bdf|ace) as shown in Fig. 7.9(a). Following the same argument as with the bipartitions of the form 2×4, these have direct first and

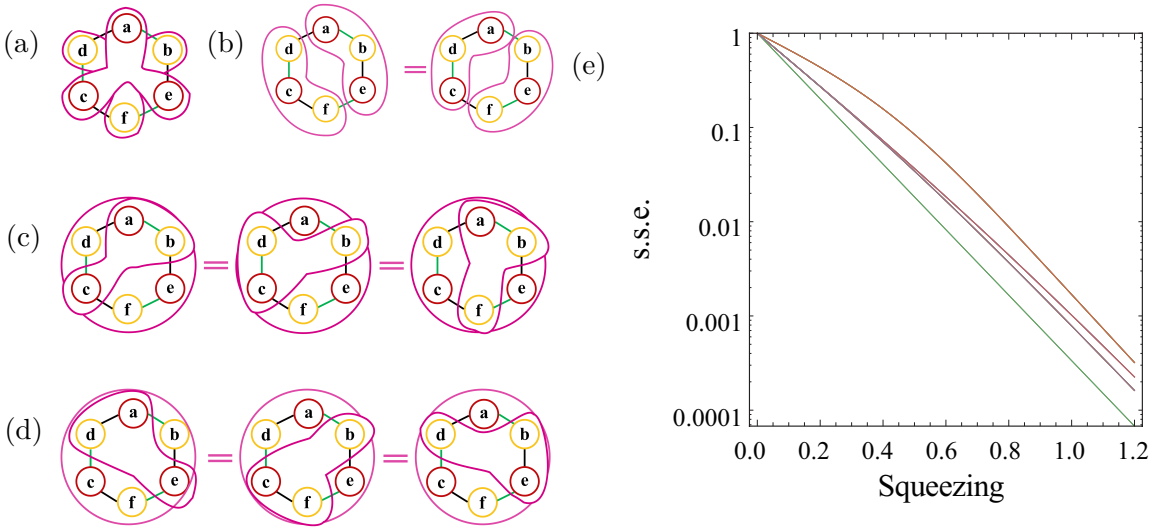

Figure 7.9: (a) through (d) Graphical representations of bipartitions of the form 3×3. (e) Smallest symplectic eigenvalues (s.s.e.) for the hexapartite entangled state with respect to the squeezing parameter for bipartitions of the form 3×3.

the second stages connections that lead to the most entanglement. The second and third lowest traces, colored purple and magenta, represent partitions that group modes with nearest neighbors connected by a first stage and one mode that is a second nearest neighbor [abc|def, abf|cde, aef|bcd], as shown in Fig. 7.9(c), and partitions that group nearest neighbors connected by a second stage and one mode that is a second nearest neighbor [ade|bcf, adf|bce, bde|acf], as shown in Fig. 7.9(d). Again, there is a difference between groupings with modes connected by a first stage PA or by a second stage PA. Groupings with the nearest neighbors from the first stage show more entanglement than groupings with nearest neighbors from the second stage. Finally, the brown trace in Fig. 7.9(b) represents bipartitions with modes in one partition composed of only

nearest neighbors [abe|cdf,bef|acd,cef|abd]. All possible bipartitions needed for the PPT criteria have their smallest eigenvalue smaller than 1 when the squeezing is larger than 0, which implies GME in the hexapartite system.

7.2.3 Octapartite Genuine Multipartite Entanglement

Following the same trend, we can increase the number of the modes by adding one more PA to the first and the second stages, as shown in Fig. 7.6(b), to create genuine octapartite entanglement. For the octapartite system, there are total $2^{8-1} - 1 = 127$ possible bipartitions that need to be verified. Figures 7.10(a), (b), (c), and (d) show the smallest symplectic eigenvalues for bipartitions of the form 1×7, 2×6, 3×5, and 4×4, respectively. For bipartitions of the form 1×7, there are ${}^8C_1 = 8$ cases for which all the traces have the same level of violation of the PPT criteria due to symmetry. Bipartition of the form 2×6 for the octapartite system behave relatively similar to the bipartition of the form 2×4 for the hexapartite system. There are total of ${}^8C_2 = 15$ partitions, but only 5 unique behaviors, as shown in Fig. 7.10(b).

Traces for the octapartite case, shown in Fig. 7.10(b), and traces for the hexapartite case, shown in Fig. 7.8(d), are identically ordered except for the one with the second-to-lowest trace, colored red in Fig. 7.10(b). These traces are composed of the partitions between fourth nearest neighbors and the rest of the system [ae|bcdfgh, bf|acdegh, cg|abdefh, dh|abcefg], as shown in Fig. 7.11(a), and the partitions between third nearest neighbors connected with two first stages and one second stage [ah|bcdefg, de|abcfgh, gf|abcdeh, bc|adefgh], as shown by the left diagram in Fig. 7.11(b).

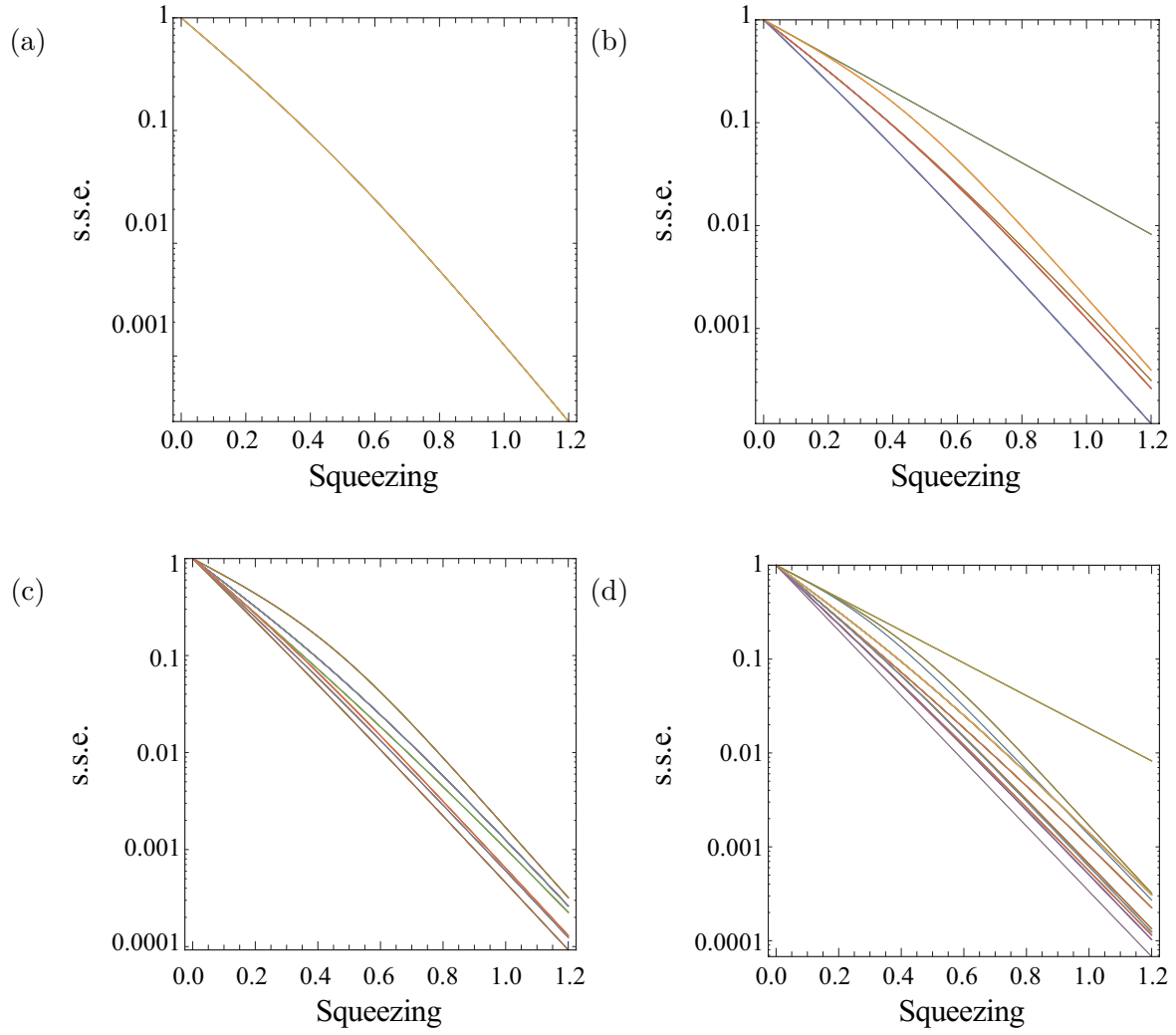

Figure 7.10: Smallest symplectic eigenvalues (s.s.e.) of the octapartite entangled state with respect to squeezing parameter ($s_1 = s_2$) with the bipartitions of the form (a) 1×7, (b) 2×6, (c) 3×5, and (d) 4×4. All possible partition for the PPT criteria have their smallest eigenvalue smaller than 1 when the squeezing is greater than 0, which implies GME in the octapartite system.

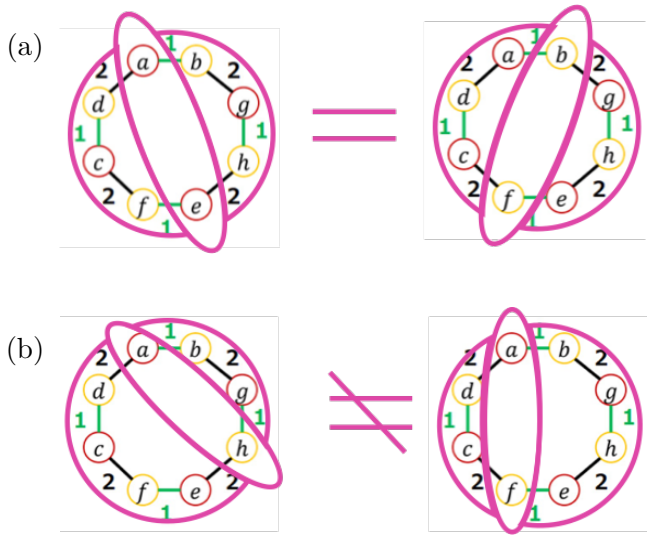

Figure 7.11: (a) and (b) Graphical representations of bipartitions of the form 2×6.

For the octapartite case, we can see that grouping the fourth nearest neighbors with two first stages and two second stage is equivalent to grouping the fourth nearest neighbor with two second stages and two first stage, as shown in Fig. 7.11(a), due to reflection symmetry. Interestingly, we can see that the left diagram in Fig. 7.11(b) has the same degree of entanglement as the one in in Fig. 7.11(a). This is because those two modes are far enough to become independent of each other. Despite the fact that distance between two modes is different, they show the same separability. This actually simplifies our system, and make it easier to track the corrections as the number of mode increase, which we will discuss in the next section.

On the other hand, Fig. 7.11(b) shows a different behaviors for the two cases of third nearest neighbors. This can be understood by tracking how they are connected to each other in the proposed scheme. The connection shown in Fig. 7.12(a) with one

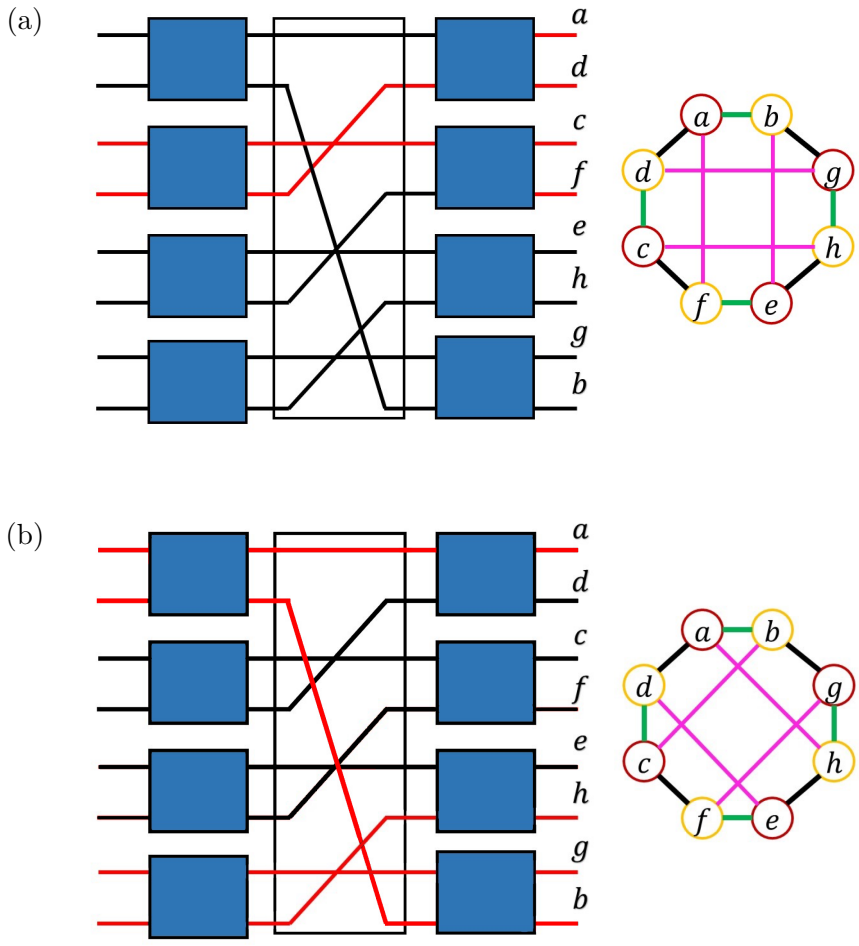

Figure 7.12: Two difference cases for third nearest neighbors such as (a) a and f connected by cascaded PAs or (b) a and h from completely independent processes.

partition composed of the third nearest neighbors with two second stage connections and one first stage connection, is a simple cascade PA configuration where the two stages generate four-mode entangled state. However, the partition composed of third nearest neighbors shown in Fig. 7.12(b) with two second stage connections and one first stage-connection are completely independent process.

Since fourth nearest neighbors are always independent, these third nearest neighbor and fourth nearest neighbors exhibit the same level of entanglement, which is a new feature of the octapartite system because the quadrapartite as the hexapartite system does not have independent processes between any two modes.

The number of total bipartitions for the rest of the system is given by ${}^8C_3 = 56$ and ${}^8C_4/2 = 35$, which have smallest symplectic eigenvalue shown in Figs. 7.10(c) and (d). Although the number of possible bipartitions increases rapidly, the physics remain the same. We check all possible bipartitions for the octapartite system and show that the smallest symplectic eigenvalue is smaller than 1 when the squeezing parameter is greater than 0. Therefore, we can conclude that we have GME in the octapartite system as well. All the calculations are done in Mathematica with the SNEG package [128].

7.3 Covariance Matrix

One of the advantages of our proposal is that as we increase the number of modes some of the mode start to become independent of the other modes. This makes the entanglement structure simple and possible to track the correlations between the different modes.

We first consider the CM for the hexapartite and octapartite systems and find the repeating patterns shown in Tables 7.2(a) and (b), respectively. We mark equal element with the same color in the matrix and define A=$\alpha_+\beta_-I_2$, B= $-1/2\ \alpha_-(\beta_+ + 1)J$, B′= $-\alpha_+\beta_-J$, C= $1/2\ \alpha_-\beta_-I_2$, and D = $-1/2\ \alpha_-(\beta_+ - 1)J$. I_2 and J are the 2x2 identity

$\sigma_6 =$

A	B	C	D	C	B′
B	A	B′	C	D	C
C	B′	A	B	C	D
D	C	B	A	B′	C
C	D	C	B′	A	B
B′	C	D	C	B	A

$\sigma_8 =$

A	B	C	0	0	D	C	B′
B	A	B′	C	D	0	0	C
C	B′	A	B	C	0	0	D
0	C	B′	A	B	C	D	0
0	D	C	B′	A	B	C	0
D	0	0	C	B	A	B′	C
C	0	0	D	C	B′	A	B
B′	C	D	0	0	C	B	A

Table 7.2: Matrix structure of the CM element for the hexapartite and octapartite cases.

matrix and diag{1,-1}, respectively.

As we increase the numbers of modes, we add two modes at a time. Such that if we extend our system, we can write the CM for an $2N$-partite system in the form given in Table 7.3. As can be seen, some elements move toward the corners and are completely separated from the center elements. This is because only neighbors with less than a fourth nearest neighbor connection show correlations in the CM, as we seen in Fig. 7.11(a).

Term "A", marked with gray, represents the self-correlation terms and corresponds to the variance of the quadratures. Since all the modes are amplified equally, they all have the same variance. Terms "B" and "B′", marked with light blue and blue, represent the first nearest neighbor. As we have explained in the previous section,

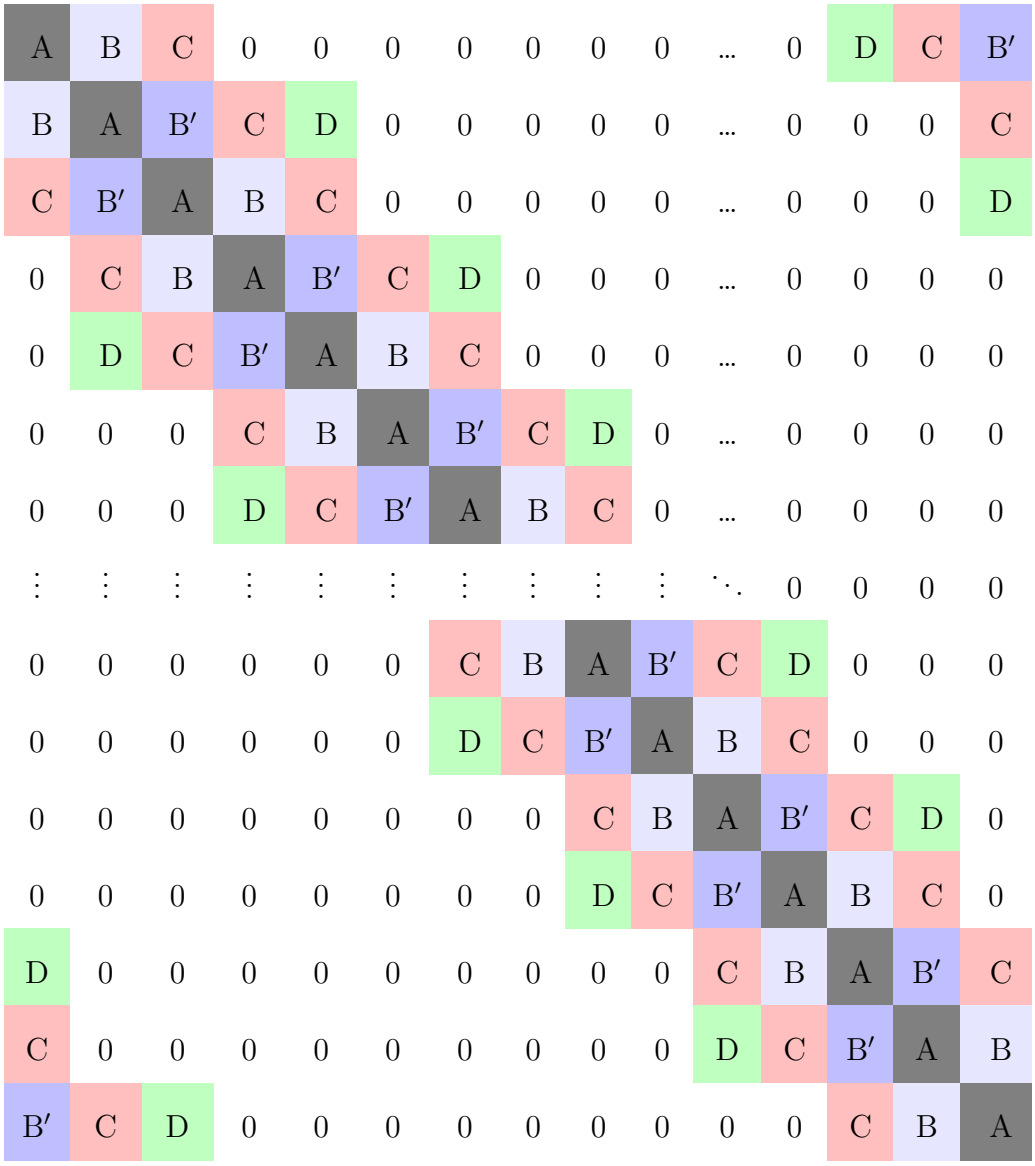

Table 7.3: Matrix structure of the quadrature CM element for the $2N$-partite system.

the nearest neighbors "B" and "B′" have different values because "B" results from entangling with a first stage PA and adding amplification noise with the second stage, but "B′" results from adding amplification noise with the first stage and entangling with a second stage PA. Term "C", marked with red, represents the second nearest neighbor, and term "D", marked with green, represents the third nearest neighbor. The other third nearest neighbors are not correlated to the rest of the modes as the corresponding elements of the CM are zero, as shown in Fig. 7.12(b).

Our generalized CM provides a way to understand the entanglement structure of our source. In Sects. 7.2.2 and 7.2.3, we pointed out that many bipartitions can be reduced down to a small number of unique cases, and that nearest neighbors with more than a fourth nearest neighbor order connection become uncorrelated. Using these observation, we are currently working on the proof that our system has genuine $2N$-partite entanglement. This portion of the work is being done in collaboration with Sho Onoe by resorting to a measure known as α-entanglement of formation, which shows that some bipartitions are more entangled than others [129, 130]. This is still part of ongoing research, and the result will be presented in a future publication.

7.4 Experimental Proposal

One of the important advantages of our scheme is that it can be implemented experimentally in a simple and compact way using only two PAs and taking advantage of the multi-spatial mode properties of the two-mode squeezed state generated with FWM.

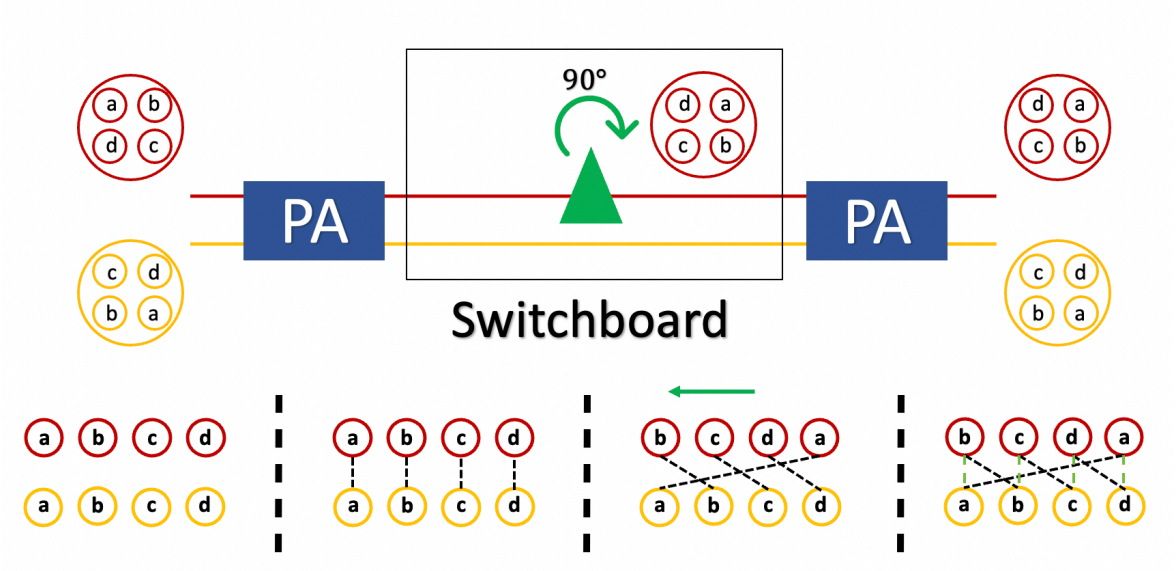

Figure 7.13: Experimental proposal to generate scalable genuine hexapartite entangled states.

Figure 7.13 shows an experimental proposal utilizing the ability to create multi-spatial entanglement [131]. Our experimental proposal is divided into four steps.

First, we prepare the initial spatially separated modes without any connections before the PA. This can be done through a liquid crystal spatial light modulator or a digital light processing. Those spatial modes are independent modes without any correlation between them. As seen in the first part of Fig. 7.13, we denote the eight spatially separated modes as [a,b,c,d] in red and [a,b,c,d] in yellow.

In the second step, we generate two-mode squeezed light using our FWM process. This can generate entanglement in many spatially modes [131]. We seed both beams into the PA. Due to momentum conservation, this process entangles the opposite mode of the light in the spatial region. These connections are indicated by a black dashed

vertical line between red and yellow circles.

The third step is the switchboard operation, which can be simply implemented with the rotation of one of the beams. For example, in the eight beam case (four beams in red and four beams in yellow), we need to rotate the beam by 90°. This rotation can be done with a dove prism. For a higher number of mode, it requires a $2\pi/N$ rotation. After the rotation, the red ordering [a,b,c,d] is shifted to [b,c,d,a].

After we rotate the beam, a second PA is then used to correlate the two beams. This spatially entangles and creates the final connections between all the modes. Again, these connections are marked with a green line between red and yellow circles. As can be seen, connections are made to every nearest neighbor, which are the same as those we have shown in the proposal for the generation of GME.

7.5 Conclusion

In conclusion, we propose a novel technique for generating scalable GME using a PA network. We show the existence of quadripartite, hexapartite, and octapartite GME by showing the violation of the PPT criteria for all possible bipartitions; and investigate the physics of each bipartition. While examining the system, we pointed out that the CM matrix can be generalized to a $2N$-partite system for which it is easy to track the correlations between the modes. In collaboration with Sho Onoe, we will generalize and show that our system has GME for the general case of a $2N$-partite system.

One of the main advantages of our scheme is that it can be easily implemented

experimentally using the spatial properties of the light. By controlling the input spatial mode and implementing the switchboard operation with a rotation, we can create a genuine multipartite entangled state of light.

The unique feature of our experimental proposal over other sources of multipartite entanglement [132, 133] is that our entanglement is not in frequency, but in terms of spatial mode. For applications in quantum computation and distributed quantum sensing, those mode need to be spatially or temporally separated in order to be measured. Our entanglement is already in the form of spatially separated modes, so this can be beneficial to perform measurements for the applications.

Chapter 8

Conclusions and Future Work

A crisis without equal on earth, the most profound collision of conscience, a decision that was conjured up against everything that had been believed, demanded, hallowed so far. I am no man, I am dynamite.

- Friedrich Nietzsche, *Ecce Homo 1*

In this dissertation, we discuss the basic properties of squeezed states of light and the techniques we can use to control the quantum state of light. From the two-mode squeezed light generated with FWM process in ^{85}Rb, we generate squeezed light resonant with the D1 ^{87}Rb, the D2 ^{87}Rb, the D1 ^{85}Rb transitions and explore resonance with D1 line of sodium. We also generate a single-mode squeezed state from a two-mode squeezed state and propose a way to generate multi-mode entangled light from PA network.

8.1 Implication of the Work

Our work will play an important role in quantum sensing, communication, and fundamental science by demonstrating and controlling quantum resources. Generating resonant squeezed light using atomic ensembles overcomes several experimental difficulties associated with crystal-based sources. In addition, a resonant squeezed state with a bandwidth of the order of the atomic natural linewidth will make it possible to

study the interaction between atoms and quantum state of light. These quantum states of light can enhance devices based on atomic sensor such as atomic interferometers and atomic magnetometers. Additionally, our ability to control and create quantum states of light could impact quantum communication and quantum computing by controlling quantum information and transmitting it to others.

The narrowband two-mode squeezed light in which both modes are simultaneously on resonance with an atomic transition opens the door for the deterministic transfer of quantum correlations from light to two remote atomic ensembles by interacting the squeezed light and atomic ensembles [134]. This can be achieved through the implementation of an EIT-based quantum memory, which has been shown to preserve the quantum properties of the light [59, 60], in two remote atomic ensembles to simultaneously transfer the quantum properties of the probe and the conjugate to the spin degree of freedom of the memories. This will lead to the possibility of storage and delay of Gaussian entangled beams of light.

8.2 Future Work

In the 7 years we have developed and completed many projects, but a lot of work is still in progress. Here are some ongoing projects related to this paper.

8.2.1 Generation of Atomic Resonant Squeezed Light

We demonstrate the generation of atomic resonant squeezed light resonance with ^{85}Rb. The ability to generation of atomic resonant squeezed light can enable to interact the

squeezed light with cold atom system to enhance the imaging technique that we can have sub-shot noise atomic imaging which can reduce the exposure time and enhance the sensitivity of the measurement.

In addition, we are collaborating with Dr. Arne Schwettmann's lab to generate the squeezed light resonance with sodium atom, because we are interested in interaction between quantum light and BEC from Dr. Arne Schwettmann's lab. As BEC can be used as an atomic sensing with excellent sensitivity [135], interaction between the BEC and squeezed light can offer squeezed light enhanced atomic sensors with extreme sensitivities.

8.2.2 Experimental Generation on Genuine Multipartite Entanglement

We are preparing for GME experiments in our lab. As we suggested in the thesis, we use the FWM process to develop two parameter amplifiers and set up an interferometer. As there are many works on building measurement-based quantum computation based on squeezed light [136], Successful generation of scalable multipartite entangled light can be valuable resource for quantum information science.

References

[1] S. Buchholz, J. Mariani, A. Routh, A. Keyal, and P. K. Kishnani, "The realist's guide to quantum technology and national security," *Deloitte Insights*, 2020.

[2] J. P. Dowling and G. J. Milburn, "Quantum technology: the second quantum revolution," *Philosophical Transactions of the Royal Society of London. Series A: Mathematical, Physical and Engineering Sciences*, vol. 361, no. 1809, pp. 1655–1674, 2003.

[3] G. Lichfield, "Inside the race to build the best quantum computer on earth," *MIT Technology Review*, Feb 2020.

[4] C. L. Degen, F. Reinhard, and P. Cappellaro, "Quantum sensing," *Rev. Mod. Phys.*, vol. 89, p. 035002, 2017.

[5] R. Wang, R. S. Tessinari, E. Hugues-Salas, A. Bravalheri, N. Uniyal, A. S. Muqaddas, R. S. Guimaraes, T. Diallo, S. Moazzeni, Q. Wang, G. T. Kanellos, R. Nejabati, and D. Simeonidou, "End-to-end quantum secured inter-domain 5G service orchestration over dynamically switched flex-grid optical networks enabled by a q-roadm," *J. Light. Technol.*, vol. 38, no. 1, pp. 139–149, 2020.

[6] E. S. Polzik, J. Carri, and H. J. Kimble, "Spectroscopy with squeezed light," *Phys. Rev. D*, vol. 68, pp. 3020–3023, 1992.

[7] A. M. Marino and J. C. R. Stroud, "Deterministic secure communications using two-mode squeezed states," *Phys. Rev. A*, vol. 74, p. 022315, 2006.

[8] G. Brida, M. Genovese, and I. R. Berchera, "Experimental realization of sub-shot-noise quantum imaging," *Nat. Photon.*, vol. 4, pp. 227–230, 2010.

[9] R. Raussendorf and H. J. Briegel, "A one-way quantum computer," *Phys. Rev. Lett.*, vol. 86, pp. 5188–5191, 2001.

[10] L. Liu, D.-S. Lü, W.-B. Chen, T. Li, Q.-Z. Qu, B. Wang, L. Li, W. Ren, Z.-R. Dong, J.-B. Zhao, W.-B. Xia, X. Zhao, J.-W. Ji, M.-F. Ye, Y.-G. Sun, Y.-Y. Yao, D. Song, Z.-G. Liang, S.-J. Hu, D.-H. Yu, X. Hou, W. Shi, H.-G. Zang, J.-F. Xiang, X.-K. Peng, and Y.-Z. Wang, "In-orbit operation of an atomic clock based on laser-cooled ^{87}Rb atoms," *Nat. Commun.*, vol. 9, no. 1, 2018.

[11] F. Wolfgramm, A. Cerè, F. A. Beduini, A. Predojević, M. Koschorreck, and M. W. Mitchell, "Squeezed-light optical magnetometry," *Phys. Rev. Lett.*, vol. 105, p. 053601, 2010.

[12] S. Kim and A. M. Marino, "Generation of ^{87}Rb resonant bright two-mode squeezed light with four-wave mixing," *Opt. Express*, vol. 26, pp. 33366–33375, 2018.

[13] N. Foundation, "The nobel prize in physics," 1921.

[14] R. J. Glauber, "Coherent and incoherent states of the radiation field," *Phys. Rev.*, vol. 131, pp. 2766–2788, 1963.

[15] D. Stoler, "Equivalence classes of minimum uncertainty packets," *Phys. Rev. D*, vol. 1, pp. 3217–3219, 1970.

[16] H. P. Yuen, "Two-photon coherent states of the radiation field," *Phys. Rev. A*, vol. 13, pp. 2226–2243, 1976.

[17] D. F. Walls, "Squeezed states of light," *Nature*, vol. 306, no. 5939, pp. 141–146, 1983.

[18] H. Yuen and J. Shapiro, "Optical communication with two-photon coherent states–part i: Quantum-state propagation and quantum-noise," *IEEE Transactions on Information Theory*, vol. 24, no. 6, pp. 657–668, 1978.

[19] C. M. Caves, "Quantum-mechanical noise in an interferometer," *Phys. Rev. D*, vol. 23, p. 1693, 1981.

[20] D. Castelvecchi, "Gravitational-wave observatory LIGO set to double its detecting power," *Nature*, vol. 566, no. 7744, p. 305–305, 2019.

[21] L. Davidovich, "Sub-poissonian processes in quantum optics," *Rev. Mod. Phys.*, vol. 68, p. 127, 1996.

[22] J. Schwinger, L. L. DeRaad, and K. A. Milton, "Casimir effect in dielectrics," *Ann. Phys.*, vol. 115, no. 1, pp. 1–23, 1978.

[23] J. W. Gibbs, *Elementary Principles in Statistical Mechanics: Developed with Especial Reference to the Rational Foundation of Thermodynamics*. Cambridge Library Collection - Mathematics, Cambridge University Press, 2010.

[24] C. W. J. Beenakker and C. Schonenberger, "Quantum shot noise," *Phys. Today*, vol. 56, pp. 37—42, 2003.

[25] A. M. Marino, *Experimental studies of two-mode squeezed states in rubidium vapor*. PhD thesis, The Institute of Optics, The College School of Engineering and Applied Sciences, University of Rochester.

[26] M. Dickson, "Non-relativistic quantum mechanics," in *Philosophy of Physics* (J. Butterfield and J. Earman, eds.), Handbook of the Philosophy of Science, pp. 275–415, Amsterdam: North-Holland, 2007.

[27] R. Simon, N. Mukunda, and B. Dutta, "Quantum-noise matrix for multimode systems: U(n) invariance, squeezing, and normal forms," *Phys. Rev. A*, vol. 49, pp. 1567–1583, 1994.

[28] L. Lami, A. Serafini, and G. Adesso, "Gaussian entanglement revisited," *New J. Phys.*, vol. 20, no. 2, p. 023030, 2018.

[29] R. Y. Teh and M. D. Reid, "Criteria for genuine n-partite continuous-variable entanglement and Einstein-Podolsky-Rosen steering," *Phys. Rev. A*, vol. 90, p. 062337, 2014.

[30] A. Yariv and D. M. Pepper, "Amplified reflection, phase conjugation, and oscillation in degenerate four-wave mixing," *Opt. Lett.*, vol. 1, no. 1, pp. 16–18, 1977.

[31] H. P. Yuen and J. H. Shapiro, "Generation and detection of two-photon coherent states in degenerate four-wave mixing," *Opt. Lett.*, vol. 4, no. 10, pp. 334–336, 1979.

[32] R. E. Slusher, L. W. Hollberg, B. Yurke, J. C. Mertz, and J. F. Valley, "Observation of squeezed states generated by four-wave mixing in an optical cavity," *Phys. Rev. Lett.*, vol. 55, pp. 2409–2412, 1985.

[33] M. S. Shahriar and P. R. Hemmer, "Generation of squeezed states and twin beams via non-degenerate four-wave mixing in a λ system," *Opt. Commun.*, vol. 158, no. 1-6, pp. 273–286, 1998.

[34] C. F. McCormick, A. M. Marino, V. Boyer, and P. D. Lett, "Strong low-frequency quantum correlations from a four-wave-mixing amplifier," *Phys. Rev. A*, vol. 78, p. 043816, 2008.

[35] Q. Glorieux, L. Guidoni, S. Guibal, J.-P. Likforman, and T. Coudreau, "Quantum correlations by four-wave mixing in an atomic vapor in a nonamplifying regime: Quantum beam splitter for photons," *Phys. Rev. A*, vol. 84, p. 053826, 2011.

[36] R. Boyd, *Nonlinear Optics*. Elsevier, 2020.

[37] M. D. Lukin, P. R. Hemmer, M. Löffler, and M. O. Scully, "Resonant enhancement of parametric processes via radiative interference and induced coherence," *Phys. Rev. Lett.*, vol. 2675–2678, pp. 37—42, 1998.

[38] M. T. Turnbull, P. G. Petrov, C. S. Embrey, A. M. Marino, and V. Boyer, "Role of the phase-matching condition in nondegenerate four-wave mixing in hot vapors for the generation of squeezed states of light," *Phys. Rev. A*, vol. 88, p. 033845, 2013.

[39] Q. Glorieux, R. Dubessy, S. Guibal, L. Guidoni, J.-P. Likforman, T. Coudreau, and E. Arimondo, "Double-Λ microscopic model for entangled light generation by four-wave mixing," *Phys. Rev. A*, vol. 82, p. 033819, 2010.

[40] D. Steck, "Rubidium 85 D Line Data," 2008. https://steck.us/alkalidata/.

[41] A. M. Marino, "Twin beam detection: unpublished,"

[42] A. I. Lvovsky, "Squeezed light," *arXiv preprint arXiv:1401.4118*, 2014.

[43] C. F. McCormick, A. M. Marino, V. Boyer, , and P. D. Lett, "Strong low-frequency quantum correlations from a four-wave-mixing amplifier," *Phys. Rev. A*, vol. 78, p. 043816, 2008.

[44] M. Mehmet, T. Eberle, S. Steinlechner, H. Vahlbruch, and R. Schnabel, "Demonstration of a quantum-enhanced fiber Sagnac interferometer," *Opt. Lett.*, vol. 35, no. 10, pp. 1665–1667, 2010.

[45] M. Dowran, A. Kumar, B. J. Lawrie, R. C. Pooser, and A. M. Marino, "Quantum-enhanced plasmonic sensing," *Optica*, vol. 5, pp. 628–633, 2018.

[46] T. L. S. Collaboration, "A gravitational wave observatory operating beyond the quantum shot-noise limit," *Nat. Phys.*, vol. 7, pp. 962–965, 2011.

[47] T. Gehring, V. Händchen, J. Duhme, F. Furrer, T. Franz, C. Pacher, R. F. Werner, and R. Schnabel, "Implementation of continuous-variable quantum key distribution with composable and one-sided-device-independent security against coherent attacks," *Nat. commun.*, vol. 6, pp. 8795–8795, 2015.

[48] C. Weedbrook, S. Pirandola, R. García-Patrón, N. J. Cerf, T. C. Ralph, J. H. Shapiro, and S. Lloyd, "Gaussian quantum information," *Rev. Mod. Phys.*, vol. 84, pp. 621–669, 2012.

[49] A. M. Marino and C. R. Stroud, "Deterministic secure communications using two-mode squeezed states," *Phys. Rev. A*, vol. 74, p. 022315, 2006.

[50] A. Kumar, H. Nunley, and A. M. Marino, "Observation of spatial quantum correlations in the macroscopic regime," *Phys. Rev. A*, vol. 95, p. 053849, 2017.

[51] N. C. Menicucci, S. T. Flammia, and O. Pfister, "One-way quantum computing in the optical frequency comb," *Phys. Rev. Lett.*, vol. 101, p. 130501, 2008.

[52] J. M. Arrazola, V. Bergholm, K. Brádler, T. R. Bromley, M. J. Collins, I. Dhand, A. Fumagalli, T. Gerrits, A. Goussev, L. G. Helt, J. Hundal, T. Isacsson, R. B. Israel, J. Izaac, S. Jahangiri, R. Janik, N. Killoran, S. P. Kumar, J. Lavoie, A. E. Lita, D. H. Mahler, M. Menotti, B. Morrison, S. W. Nam, L. Neuhaus, H. Y. Qi, N. Quesada, A. Repingon, K. K. Sabapathy, M. Schuld, D. Su, J. Swinarton, A. Száva, K. Tan, P. Tan, V. D. Vaidya, Z. Vernon, Z. Zabaneh, and Y. Zhang, "Quantum circuits with many photons on a programmable nanophotonic chip," *Nature*, vol. 591, no. 7848, pp. 54–60, 2021.

[53] G. S. Agarwal and M. O. Scully, "Ramsey spectroscopy with nonclassical light sources," *Phys. Rev. A*, vol. 53, pp. 467–470, 1996.

[54] S. S. Szigeti, B. Tonekaboni, W. Yung, S. Lau, S. N. Hood, and S. A. Haine, "Squeezed-light-enhanced atom interferometry below the standard quantum limit," *Phys. Rev. A*, vol. 90, p. 063630, 2014.

[55] T. Horrom, R. Singh, J. P. Dowling, and E. E. Mikhailov, "Quantum-enhanced magnetometer with low-frequency squeezing," *Phys. Rev. A*, vol. 86, p. 023803, 2012.

[56] I. Kruse, K. Lange, J. Peise, B. Lücke, L. Pezzè, J. Arlt, W. Ertmer, C. Lisdat, L. Santos, A. Smerzi, and C. Klempt, "Improvement of an atomic clock using squeezed vacuum," *Phys. Rev. Lett.*, vol. 117, p. 143004, 2016.

[57] A. Peng, M. Johnsson, W. P. Bowen, P. K. Lam, H.-A. Bachor, and J. J. Hope, "Squeezing and entanglement delay using slow light," *Phys. Rev. A*, vol. 71, p. 033809, 2005.

[58] D. Akamatsu, K. Akiba, , and M. Kozuma, "Electromagnetically induced transparency with squeezed vacuum," *Phys. Rev. Lett.*, vol. 92, p. 203602, 2004.

[59] K. Honda, D. Akamatsu, M. Arikawa, Y. Yokoi, K. Akiba, S. Nagatsuka, T. Tanimura, A. Furusawa, and M. Kozuma, "Storage and retrieval of a squeezed vacuum," *Phys. Rev. Lett.*, vol. 100, p. 093601, 2008.

[60] J. Appel, E. Figueroa, D. Korystov, M. Lobino, and A. I. Lvovsky, "Quantum memory for squeezed light," *Phys. Rev. Lett.*, vol. 100, p. 093602, 2008.

[61] S. A. Haine and J. J. Hope, "Outcoupling from a Bose-Einstein condensate with squeezed light to produce entangled-atom laser beams," *Phys. Rev. A*, vol. 72, p. 033601, 2005.

[62] J. Zielińska and M. W. Mitchell, "Atom-resonant squeezed light from a tunable monolithic PPRKTP parametric amplifier," *Opt. Lett.*, vol. 43, pp. 643–646, 2018.

[63] X. Guo, C. R. Breum, J. Borregaard, S. Izumi, M. V. Larsen, T. Gehring, M. Christandl, J. S. Neergaard-Nielsen, and U. L. Andersen, "Distributed quantum sensing in a continuous-variable entangled network," *Nat. Phys.*, vol. 16, no. 3, pp. 281–284, 2019.

[64] O. G. Hétet, Glöckl, K. A. Pilypas, C. C. Harb, B. C. Buchler, H. A. Bachor, and P. K. Lam, "Squeezed light for bandwidth-limited atom optics experiments at the rubidium D1 line," *J. Phys. B*, vol. 40, pp. 221–226, 2007.

[65] Y. Han, X. Wen, J. He, B. Yang, Y. Wang, and J. Wang, "Improvement of vacuum squeezing resonant on the rubidium D1 line at 795 nm," *Opt. Express*, vol. 24, pp. 2350–2359, 2016.

[66] S. Burks, J. Ortalo, A. Chiummo, X. Jia, F. Villa, A. Bramati, J. Laurat, and E. Giacobino, "Vacuum squeezed light for atomic memories at the D2 cesium line," *Opt. Express*, vol. 17, pp. 3777–3781, 2009.

[67] J. Ries, B. Brezger, and A. I. Lvovsky, "Experimental vacuum squeezing in rubidium vapor via self-rotation," *Phys. Rev. A*, vol. 68, p. 025801, 2003.

[68] I. H. Agha, G. Messin, and P. Grangier, "Generation of pulsed and continuous-wave squeezed light with ^{87}Rb vapor," *Opt. Express*, vol. 18, pp. 4198–4205, 2010.

[69] S. Barreiro, P. Valente, H. Failache, and A. Lezama, "Polarization squeezing of light by single passage through an atomic vapor," *Phys. Rev. A*, vol. 84, p. 033851, 2011.

[70] S. Kim and A. M. Marino, "Generation of narrowband 87rb resonant squeezed light with four-wave mixing," in *Rochester Conference on Coherence and Quantum Optics (CQO-11)*, p. M5A.10, Optica Publishing Group, 2019.

[71] M. D. Lukin, A. B. Matsko, M. Fleischhauer, and M. O. Scully, "Quantum noise and correlations in resonantly enhanced wave mixing based on atomic coherence," *Phys. Rev. Lett.*, vol. 82, pp. 1847–1850, 1999.

[72] C. Foot, *Atomic physics*. Oxford University Press, USA, 2005.

[73] N. Corzo, A. M. Marino, K. M. Jones, and P. D. Lett, "Multi-spatial-mode single-beam quadrature squeezed states of light from four-wave mixing in hot rubidium vapor," *Opt. Express*, vol. 19, pp. 21358–21369, 2011.

[74] E. Arimondo, M. Inguscio, and P. Violino, "Experimental determinations of the hyperfine structure in the alkali atoms," *Rev. Mod. Phys.*, vol. 49, pp. 31–75, 1977.

[75] S. Colin, E. Contesse, P. L. Boudec, G. Stephan, and F. Sanchez, "Evidence of a saturable-absorption effect in heavily erbium-doped fibers," *Opt. Lett.*, vol. 21, no. 24, pp. 1987–1989, 1996.

[76] M. W. Maeda, P. Kumar, and J. H. Shapiro, "Observation of squeezed noise produced by forward four-wave mixing in sodium vapor," *Opt. Lett.*, vol. 12, no. 3, pp. 161–163, 1987.

[77] B. L. S. Marlow, "Degenerate four-wave-mixing as a low-power source of squeezed light," *Opt. Express*, vol. 28, no. 25, pp. 38169–38183, 2020.

[78] R. C. Pooser, A. M. Marino, V. Boyer, K. M. Jones, and P. D. Lett, "Quantum correlated light beams from non-degenerate four-wave mixing in an atomic vapor: the D1 and D2 lines of ^{85}Rb and ^{87}Rb," *Opt. Express*, vol. 17, no. 19, pp. 16722–16730, 2009.

[79] C. Leonard, S. Kim, and A. Marino, "Enhanced on-resonance squeezing from four wave mixing via additional optical beam," in *APS Division of Atomic, Molecular and Optical Physics Meeting Abstracts*, vol. 2020 of *APS Meeting Abstracts*, p. Q01.063, Jan. 2020.

[80] D. Zhang, C. Li, Z. Zhang, Y. Zhang, Y. Zhang, and M. Xiao, "Enhanced intensity-difference squeezing via energy-level modulations in hot atomic media," *Phys. Rev. A*, vol. 96, p. 043847, 2017.

[81] A. M. Guerrero, R. L. R. Celis, M. Martinelli, and H. M. Florez, "Spectral control of quantum correlations in four wave mixing using dressing fields," *arXiv preprint arXiv:2201.10935*, 2022.

[82] H. G. Ooi, Q. Zhang, S. Kim, A. Marino, and A. Schwettmann, "Four-Wave Mixing in a Hot Sodium Vapor Cell in the Large Single-Photon Detuning Regime," in *APS Division of Atomic, Molecular and Optical Physics Meeting Abstracts*, vol. 2020 of *APS Meeting Abstracts*, p. Q01.071, Jan. 2020.

[83] Q. Zhang, S. Kim, L. Narcomey, A. Marino, and A. Schwettmann, "Four-wave Mixing in Hot Sodium Vapor Cells," in *APS Division of Atomic, Molecular and Optical Physics Meeting Abstracts*, vol. 2018 of *APS Meeting Abstracts*, p. T01.153, May 2018.

[84] Q. Zhang, S. Kim, M. Peters, A. M. Marino, and A. Schwettmann, "Experimental Investigation of Four-Wave Mixing in Hot Sodium Vapor Cells," in *APS Division of Atomic, Molecular and Optical Physics Meeting Abstracts*, vol. 2019 of *APS Meeting Abstracts*, p. J08.002, May 2019.

[85] H. G. Ooi, Q. Zhang, S. Kim, A. Marino, and A. Schwettmann, "Four-Wave Mixing in Hot Sodium Vapor Cells with Saturated Absorption," in *APS Division of Atomic, Molecular and Optical Physics Meeting Abstracts*, vol. 2019 of *APS Meeting Abstracts*, p. E01.098, May 2019.

[86] J. D. Swaim and R. T. Glasser, "Squeezed-twin-beam generation in strongly absorbing media," *Phys. Rev. A*, vol. 96, p. 033818, 2017.

[87] S. Kim and A. M. Marino, "Frequency Tunable Squeezed Light through Atomic State Dressing of Four-Wave Mixing," in *APS Division of Atomic, Molecular and Optical Physics Meeting Abstracts*, vol. 2020 of *APS Meeting Abstracts*, p. J02.006, Jan. 2020.

[88] Y.-J. Chen, L. F. Gonçalves, and G. Raithel, "Measurement of rb $5P_{3/2}$ scalar and tensor polarizabilities in a 1064-nm light field," *Phys. Rev. A*, vol. 92, p. 060501, 2015.

[89] R. Barret, "Theory of the hyperfine structure of free atoms," *Physics Bulletin*, vol. 24, pp. 237–237, 1973.

[90] R. Schmieder, "Matrix elements of the quadratic Stark effect on atoms with hyperfine structure," *Am. J. Phys.*, vol. 40, 1972.

[91] T. Miller and B. Bederson, "Atomic and molecular polarizabilities," *Adv. Atom. Mol. Phys.*, vol. 13, pp. 1–56, 1977.

[92] K. E. Miller, D. Krause, and L. R. Hunter, "Precise measurement of the Stark shift of the rubidium and potassium D1 lines," *Phys. Rev. A*, vol. 49, pp. 5128–5130, 1994.

[93] C. Krenn, W. Scherf, O. Khait, M. Musso, and L. Windholz, "Stark effect investigations of resonance lines of neutral potassium, rubidium, europium and gallium," *Zeitschrift fr Physik D*, vol. 41, pp. 229–233, 1997.

[94] J. Grimmel, M. Mack, F. Karlewski, F. Jessen, M. Reinschmidt, N. Sándor, and J. Fortágh, "Measurement and numerical calculation of rubidium Rydberg Stark spectra," *New J. Phys.*, vol. 17, no. 5, p. 053005, 2015.

[95] T. Vogt, M. Viteau, J. Zhao, A. Chotia, D. Comparat, and P. Pillet, "Dipole blockade at Förster resonances in high resolution laser excitation of Rydberg states of cesium atoms," *Phys. Rev. Lett.*, vol. 97, p. 083003, 2006.

[96] T. Vogt, M. Viteau, A. Chotia, J. Zhao, D. Comparat, and P. Pillet, "Electric-field induced dipole blockade with Rydberg atoms," *Phys. Rev. Lett.*, vol. 99, p. 073002, 2007.

[97] B. Ghosal, A. Banik, V. Vats, S. Pal, and R. K. Bahl, "Studies on temperature dependence of rubidium lamp for atomic frequency standard," *AIP Conf. Proc.*, vol. 1391, no. 1, pp. 321–323, 2011.

[98] M. A. Lieberman and A. J. Lichtenberg, *Principles of plasma discharges and materials processing*. Wiley, 1994.

[99] K. Rajasekaran and M. S. Naidu, "Measurement of breakdown voltages and V-I characteristics of sodium, potassium, cadmium, and zinc vapors using coaxial cylindrical electrodes," *J. Appl. Phys.*, vol. 70, pp. 4159–4164, 1991.

[100] R. E. Slusher, B. Yurke, P. Grangier, A. LaPorta, D. F. Walls, and M. Reid, "Squeezed-light generation by four-wave mixing near an atomic resonance," *J. Opt. Soc. Am. B*, vol. 4, no. 10, pp. 1453–1464, 1987.

[101] J. D. Swaim and R. T. Glasser, "Squeezed-twin-beam generation in strongly absorbing media," *Phys. Rev. A*, vol. 96, p. 033818, 2017.

[102] R. Ma, W. Liu, Z. Qin, X. Jia, and J. Gao, "Generating quantum correlated twin beams by four-wave mixing in hot cesium vapor," *Phys. Rev. A*, vol. 96, p. 043843, 2017.

[103] A. B. Matsko, G. R. W. I. Novikova, D. F. K. D. Budker, and S. M. Rochester, "Vacuum squeezing in atomic media via self-rotation," *Phys. Rev. Lett.*, vol. 66, p. 043815, 2002.

[104] M. Evers, A. Heid, and I. Ostojic, "Pharma's digital rx: Quantum computing in drug research and development," Jul 2021.

[105] J. E. Rice, T. P. Gujarati, M. Motta, T. Y. Takeshita, E. Lee, J. A. Latone, and J. M. Garcia, "Quantum computation of dominant products in lithium–sulfur batteries," *J. Chem. Phys.*, vol. 154, no. 13, p. 134115, 2021.

[106] N. Stamatopoulos, D. J. Egger, Y. Sun, C. Zoufal, R. Iten, N. Shen, and S. Woerner, "Option pricing using quantum computers," *Quantum*, vol. 4, p. 291, 2020.

[107] Y. Zhang, M. Menotti, K. Tan, V. D. Vaidya, D. H. Mahler, L. G. Helt, L. Zatti, M. Liscidini, B. Morrison, and Z. Vernon, "Squeezed light from a nanophotonic molecule," *Nat. Commun.*, vol. 12, no. 1, 2021.

[108] S. Machida and Y. Yamamoto, "Observation of sub-poissonian photoelectron statistics in a negative feedback semiconductor laser," *Opt. Commun.*, vol. 57, no. 4, pp. 290–296, 1986.

[109] J. Mertz, A. Heidmann, C. Fabre, E. Giacobino, and S. Reynaud, "Observation of high-intensity sub-poissonian light using an optical parametric oscillator," *Phys. Rev. Lett.*, vol. 64, pp. 2897–2900, 1990.

[110] J. Mertz, A. Heidmann, and C. Fabre, "Generation of sub-poissonian light using active control with twin beams," *Phys. Rev. A*, vol. 44, p. 3229, 1991.

[111] B. C. Buchler, *Electro-optic control of quantum measurements*. PhD thesis, The Australian National University.

[112] S. Kim and A. M. Marino, "Atomic resonant single-mode squeezed light from four-wave mixing through feedforward," *Opt. Lett.*, vol. 44, no. 19, pp. 4630–4633, 2019.

[113] H. Zou, S. Zhai, J. Guo, R. Yang, and J. Gao, "Preparation and measurement of tunable high-power sub-poissonian light using twin beams," *Opt. Lett.*, vol. 31, no. 11, pp. 1735–1737, 2006.

[114] A. M. Marino, R. C. Pooser, V. Boyer, and P. D. Lett, "Tunable delay of entangled images," in *Conference on Lasers and Electro-Optics/International Quantum Electronics Conference*, p. IThK3, Optica Publishing Group, 2009.

[115] R. Pooser, A. Marino, V. Boyer, K. Jones, , and P. D. Lett, "Quantum correlated light beams from non-degenerate four-wave mixing in an atomic vapor: the D1 and D2 lines of ^{85}Rb and ^{87}Rb," *Opt. Express*, vol. 17, pp. 16722–16730, 2009.

[116] R. Horodecki, P. Horodecki, M. Horodecki, and K. Horodecki, "Quantum entanglement," *Rev. Mod. Phys.*, vol. 81, no. 2, pp. 865–942, 2009.

[117] Y. Dai, Y. Dong, Z. Xu, W. You, C. Zhang, and O. Ghne, "Experimentally accessible lower bounds for genuine multipartite entanglement and coherence measures," *Phys. Rev. Applied*, vol. 13, p. 054022, 2020.

[118] Y. Yeo and W. K. Chua, "Teleportation and dense coding with genuine multipartite entanglement," *Phys. Rev. Lett.*, vol. 96, p. 060502, 2006.

[119] M. Epping, H. Kampermann, C. macchiavello, and D. Bruß, "Multi-partite entanglement can speed up quantum key distribution in networks," *New J. Phys.*, vol. 19, no. 9, p. 093012, 2017.

[120] G. Tóth, "Multipartite entanglement and high-precision metrology," *Phys. Rev. A*, vol. 85, p. 022322, 2012.

[121] P. Hyllus, W. Laskowski, R. Krischek, C. Schwemmer, W. Wieczorek, H. Weinfurter, L. Pezzé, and A. Smerzi, "Fisher information and multiparticle entanglement," *Phys. Rev. A*, vol. 85, p. 022321, 2012.

[122] S. Kim and A. M. Marino, "Scalable genuine multipartite entanglement with parametric amplifier networks," in *Frontiers in Optics / Laser Science*, p. FW7C.4, Optica Publishing Group, 2020.

[123] C. W. Sandbo Chang, M. Simoen, J. Aumentado, C. Sabín, P. Forn-Díaz, A. M. Vadiraj, F. Quijandría, G. Johansson, I. Fuentes, and C. M. Wilson, "Generating multimode entangled microwaves with a superconducting parametric cavity," *Phys. Rev. Applied*, vol. 10, p. 044019, 2018.

[124] Z. Qin, M. Gessner, Z. Ren, X. Deng, D. Han, W. Li, X. Su, A. Smerzi, and K. Peng, "Characterizing the multipartite continuous-variable entanglement structure from squeezing coefficients and the Fisher information," *NPJ Quantum Inf.*, vol. 5, no. 1, 2019.

[125] P. van Loock and A. Furusawa, "Detecting genuine multipartite continuous-variable entanglement," *Phys. Rev. A*, vol. 67, p. 052315, 2003.

[126] Z. Qin, L. Cao, H. Wang, A. M. Marino, W. Zhang, and J. Jing, "Experimental generation of multiple quantum correlated beams from hot rubidium vapor," *Phys. Rev. Lett.*, vol. 113, p. 023602, 2014.

[127] H. Wang, Z. Zheng, Y. Wang, and J. Jing, "Generation of tripartite entanglement from cascaded four-wave mixing processes," *Opt. Express*, vol. 24, no. 20, pp. 23459–23470, 2016.

[128] R. Žitko, "Sneg mathematica package for symbolic calculations with second-quantization-operator expressions," *Comput. Phys. Commun.*, vol. 182, no. 10, pp. 2259 – 2264, 2011.

[129] S. Szalay, "Multipartite entanglement measures," *Phys. Rev. A*, vol. 92, p. 042329, 2015.

[130] S. Onoe, S. Tserkis, A. P. Lund, and T. C. Ralph, "Multipartite gaussian entanglement of formation," *Phys. Rev. A*, vol. 102, p. 042408, 2020.

[131] A. Kumar, G. Nirala, and A. M. Marino, "Einstein-Podolsky-Rosen paradox with position-momentum entangled macroscopic twin beams," *arXiv preprint arXiv:2007.09259*, 2020.

[132] N. C. Menicucci, S. T. Flammia, and O. Pfister, "One-way quantum computing in the optical frequency comb," *Phys. Rev. Lett.*, vol. 101, p. 130501, 2008.

[133] J.-i. Yoshikawa, S. Yokoyama, T. Kaji, C. Sornphiphatphong, Y. Shiozawa, K. Makino, and A. Furusawa, "Invited article: Generation of one-million-mode continuous-variable cluster state by unlimited time-domain multiplexing," *APL Photonics*, vol. 1, no. 6, p. 060801, 2016.

[134] Z. Yan, L. Wu, X. Jia, Y. Liu, R. Deng, S. Li, H. Wang, C. Xie, and K. Peng, "Establishing and storing of deterministic quantum entanglement among three distant atomic ensembles," *Nat. Commun.*, vol. 8, p. 718, 2017.

[135] S. Abend, M. Gebbe, M. Gersemann, H. Ahlers, H. Müntinga, E. Giese, N. Gaaloul, C. Schubert, C. Lämmerzahl, W. Ertmer, W. P. Schleich, and E. M. Rasel, "Atom-chip fountain gravimeter," *Phys. Rev. Lett.*, vol. 117, p. 203003, 2016.

[136] M. V. Larsen, X. Guo, C. R. Breum, J. S. Neergaard-Nielsen, and U. L. Andersen, "Deterministic generation of a two-dimensional cluster state," *Science*, vol. 366, no. 6463, pp. 369–372, 2019.

[137] M. Nestor, "How many ways to partition n elements into two nonempty subsets?." Mathematics Stack Exchange. https://math.stackexchange.com/q/3340738.

Appendix A

Vacuum Chamber Design

(a)

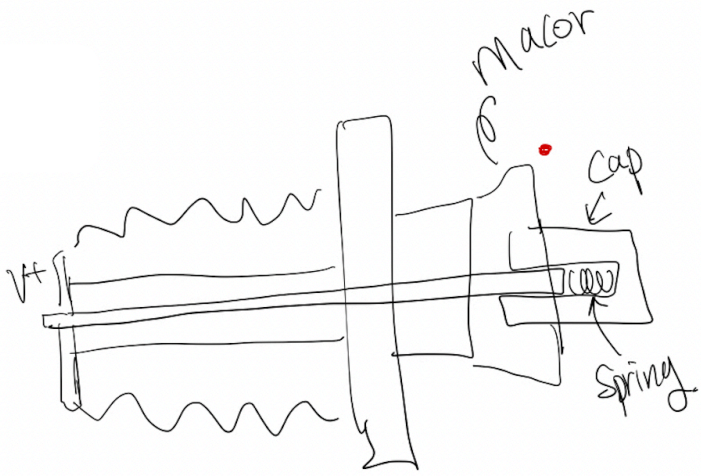

(b)

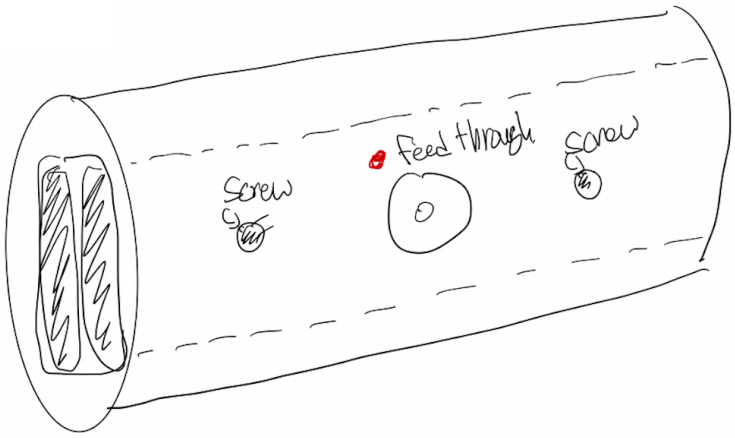

Figure A.1: (a) High voltage feedthough design and (b) Macor plate holder design.

We used a commercial vacuum feedthrough and modified it for our experiment as shown in Fig. A.1(a). An important task in the design was to avoid arcing by sharp

(a) (b)

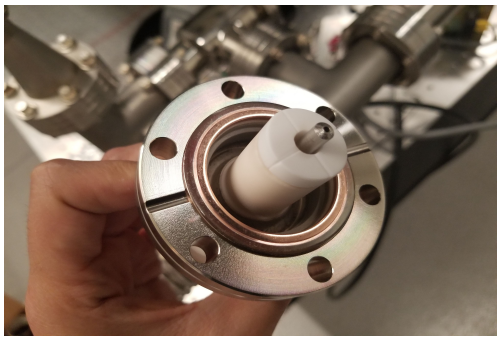

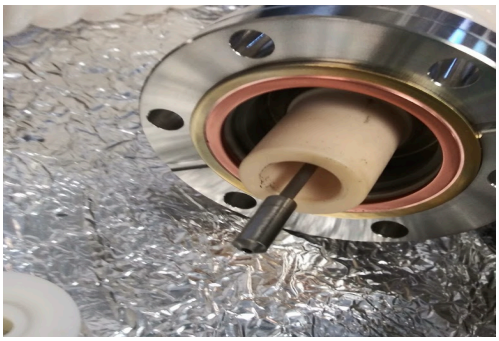

(c) (d)

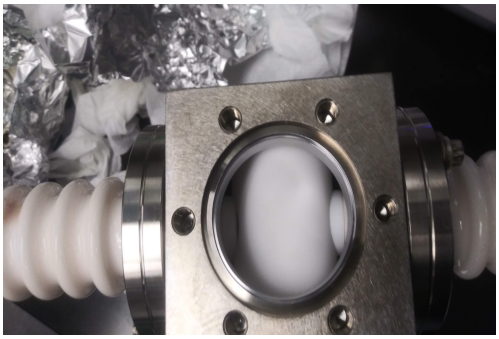

(e) (f)

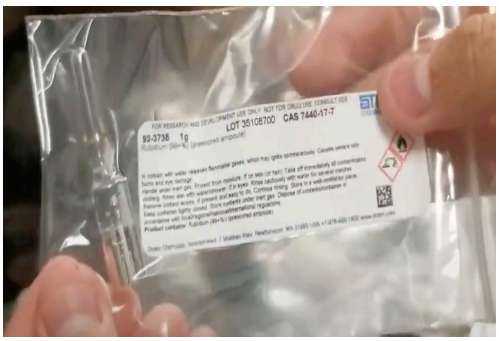

Figure A.2: (a) Feedthrough with the Macor adapter, (b) feedthrough with cap, (c) plate holder, (d) assembly of feedthrough and plate holder, (e) rubidium ampule, and (f) bellow for the cracking ampule rubidium.

points and to have good contact with the plate. Therefore, we cover the end of the conductor with a small cap with a small spring in between the cap and the conductor as shown in Figs. A.2(a) and (b)

The spring allows us maintaining contact with the plate and also increases the flexibility of the design. We also cover the conductor and the cap with a Macor adapter. The red point in Figs. A.1(a) and (b) touch each other to insulate the conductor with Macor glass. This prevents possible corona around the cap and the conductor. This can also reduce rubidium condensation inside the feedthrough due to the limited the opening.

Figure A.1(b) shows the Macor plate holder we made. Two plates are placed inside the Macor cylinder and secured with two screws to each plate. At the center there is a hole through which the conductor passes to make contact with the plate held by the Macor holder, as shown in Figs. A.2(c) through (d)

Figure 5.6 in Ch. 5 shows the overall design of the vacuum chamber. We have two valves; one small valve at the top controls the rubidium migration, and the other big valve maintain the vacuum when the vacuum pump is off. We heat the entire chamber to migrate the rubidium from the bellow into the region between the plates. Figures A.2(e) through (f) show the rubidium ampoule and the bellow.

Figure A.3 shows the procedure we use to migrate the rubidium into the chamber. We used a commercial rubidium glass ampoule and clean it with methanol and acetone. After placing the rubidium ampoule inside of the bellow, we bake the system before cracking the ampoule. Cracking the rubidium ampoule is done by applying a physical

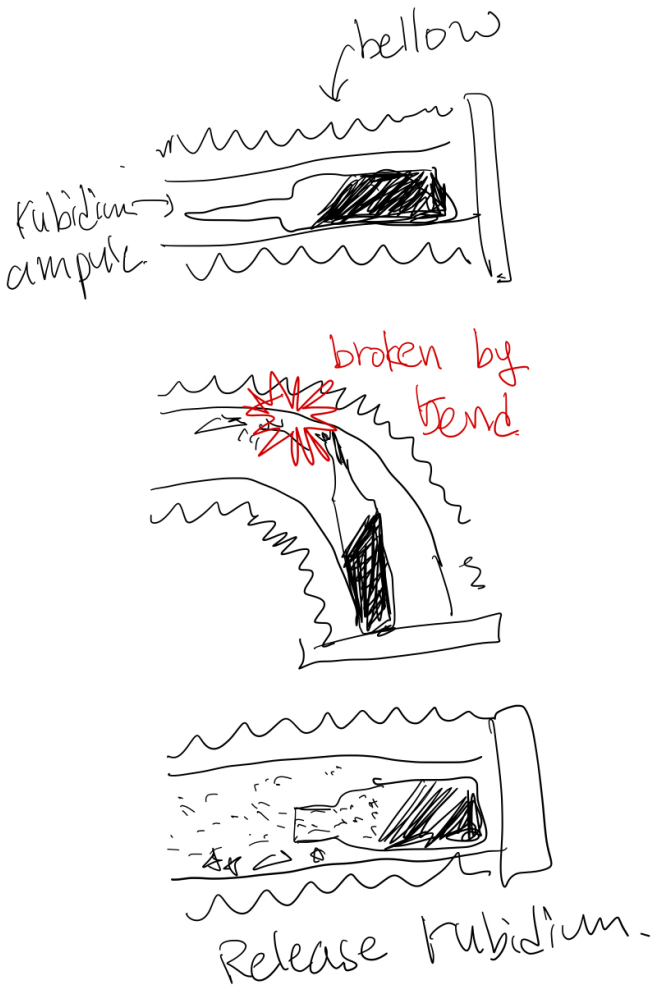

Figure A.3: Usage of the bellow to release rubidium into the high voltage chamber. First we crack the rubidium ampule by bending the bellow. We then heat up the chamber to the migrate rubidium to the region between the plates.

force by bending the bellow. Once broken, a sharp rise in pressure can be observed due to the gas inside the ampoule. After cracking, we heat the chamber to migrate rubidium into the region between the plates for the experiment.

Appendix B

Multipartite Entanglement

B.1 Partition into Two Subsets

We can calculate the total number of required PPT criteria for an N-mode case. For example, for the three-mode case [137], we can define the set S with index 1, 2, 3, such that $S = 1, 2, 3$. The power set, the set of all subsets of S, is given by

$$\mathcal{P}(S) = \Big\{\emptyset, \{1\}, \{2\}, \{3\}, \{1,2\}, \{1,3\}, \{2,3\}, \{1,2,3\}\Big\}. \tag{B.1}$$

Since we are interested in the total number of possible bipartitions in the set S, each element in the power set represent the possible bipartition. For example, if we choose $\{1\}$, automatically it will choose the other subset $\{2,3\}$. Since choosing one eliminates the other ones in $\mathcal{P}(S)$, the total possible bipartitions in set S is the number of elements in power set divide by two. Since we don't consider the bipartition with $\emptyset$ and S, we need to remove two subsets $\emptyset$ and S from $\mathcal{P}(S)$. Therefore, we can count the total number as $(2^3 - 2)/2 = 3$

In the N-mode case, the power set has 2^N elements. Choosing a pair of subset (A,B), such that A$\cup$B=S is equivalent to choosing any subsets A in $\mathcal{P}(S)$. However, we need to remove two subsets in $\mathcal{P}(S)$, $\emptyset$ and S, we thus have $2^N - 2$. When we remove the double counting from the subsets, we obtain $2^{N-1} - 1$.

B.2 Other Criteria for Quadrapartite Genuine Multipartite Entanglement

The PPT criteria is sufficient to test for the existence of genuine multipartite entanglement for a pure quantum state. However, determining GME is challenging for realistic experimental conditions where we cannot assume the system is in a pure quantum state. Therefore, it is necessary to use other tests for GME that work for mixed states, such as the Teh-Reid criteria that is based on the Loock-Furusawa inequality [125, 29].

For the quadrapartite system, the Loock-Furusawa inequalities are given by

$$\begin{aligned}
B_1 &\equiv [\Delta(\hat{X}_a - \hat{X}_b)]^2 + [\Delta(\hat{Y}_a + \hat{Y}_b + g_c\hat{Y}_c + g_d\hat{Y}_d)]^2 \geq 4, \\
B_2 &\equiv [\Delta(\hat{X}_b - \hat{X}_c)]^2 + [\Delta(g_a\hat{Y}_a + \hat{Y}_b + \hat{Y}_c + g_d\hat{Y}_d)]^2 \geq 4, \\
B_3 &\equiv [\Delta(\hat{X}_a - \hat{X}_c)]^2 + [\Delta(\hat{Y}_a + g_b\hat{Y}_b + \hat{Y}_c + g_d\hat{Y}_d)]^2 \geq 4, \\
B_4 &\equiv [\Delta(\hat{X}_c - \hat{X}_d)]^2 + [\Delta(g_a\hat{Y}_a + g_b\hat{Y}_b + \hat{Y}_c + \hat{Y}_d)]^2 \geq 4, \\
B_5 &\equiv [\Delta(\hat{X}_b - \hat{X}_d)]^2 + [\Delta(g_a\hat{Y}_a + \hat{Y}_b + g_c\hat{Y}_c + \hat{Y}_d)]^2 \geq 4, \\
B_6 &\equiv [\Delta(\hat{X}_a - \hat{X}_d)]^2 + [\Delta(g_a\hat{Y}_a + \hat{Y}_b + \hat{Y}_c + g_d\hat{Y}_d)]^2 \geq 4,
\end{aligned} \tag{B.2}$$

where g_i, for $i = a, b, c, d$, are arbitrary real parameters. In the Loock-Furusawa inequalities [125], a violation of any three inequalities indicates the presence of genuine quadrapartite entanglement; however, as Reid pointed out such a violation only shows that the state is a fully inseparable quadrapartite entangled state, which is weaker entanglement than GME. To show that the system has GME, it must violate the stronger

inequality,

$$\sum_{J=1}^{6} B_J \geq 12. \tag{B.3}$$

Figure B.1 shows Loock-Furusawa and Teh-Reid inequality for our proposed quadrapartite system described in Ch. 7. In Figs. B.1(a) through (c), the values for B_J drop below those required to violate the Loock-Furusawa inequalities; showing that a violation appears when there is some gain in both PA stages, similar to the PPT criteria. We have marked with black line to visualize the violation regions. In Fig. B.1(d), we show the Teh-Reid inequality, for which there is a much smaller region of violation compared to the Loock-Furusawa inequalities, and conclude that we can have genuine quadrapartite entanglement for large enough gain in both PA stages. This criterion is needed to identify genuine multipartite entanglement in future experimental tests.

B.3 Hexapartite Genuine Multipartite Entanglement

The PPT criteria for all possible bipartitions with respect to the squeezing parameters of the first and the second stages are shown in Fig. B.2. In Fig. B.2(a), we show bipartitions of form 1×5 [a|bcdef, b|acdef, c|abdef, d|abcef, e|abdf, f|abcde]. In Figs. B.2(b) through (e), we show the four cases of bipartition of form 3×3: partitions composed only of nearest neighbors [abe|cdf,bef|acd,cef|abd], partitions that group nearest neighbors connected through a second stage and a second nearest neighbor mode [ade|bcf,adf|bce,bde|acf], partitions that group nearest neighbors connected through a first stage and a second nearest neighbor mode [abc|def, abf|cde, aef|bcd], and

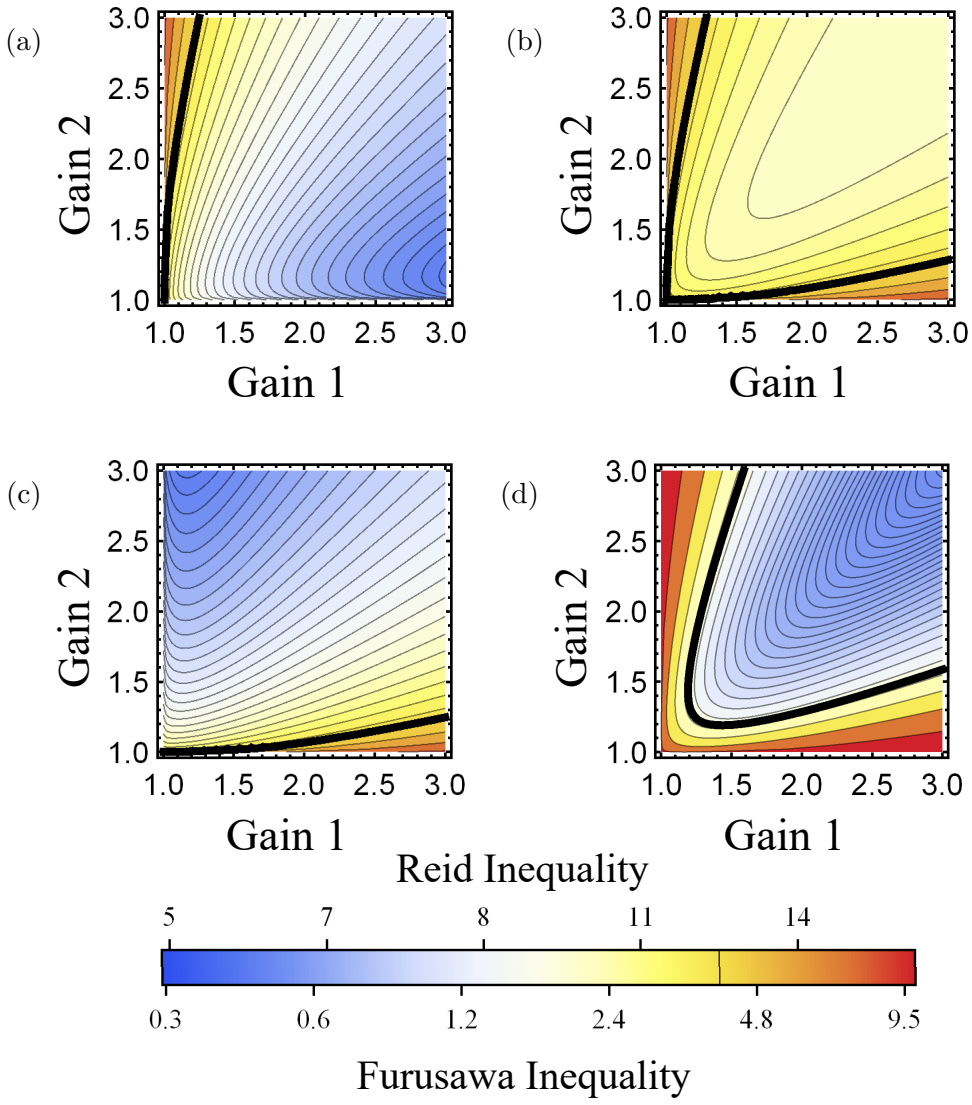

Figure B.1: Contour plots of the Loock-Furusawa and Teh-Reid inequalities for quadripartite entanglement with respect to the gain of the first and second PA stages. Their violation bound is shown with a black line. We show the Loock-Furusawa inequalities (a) B_1, (b) B_3, (c) B_6, and the (d) Teh-Reid inequality.

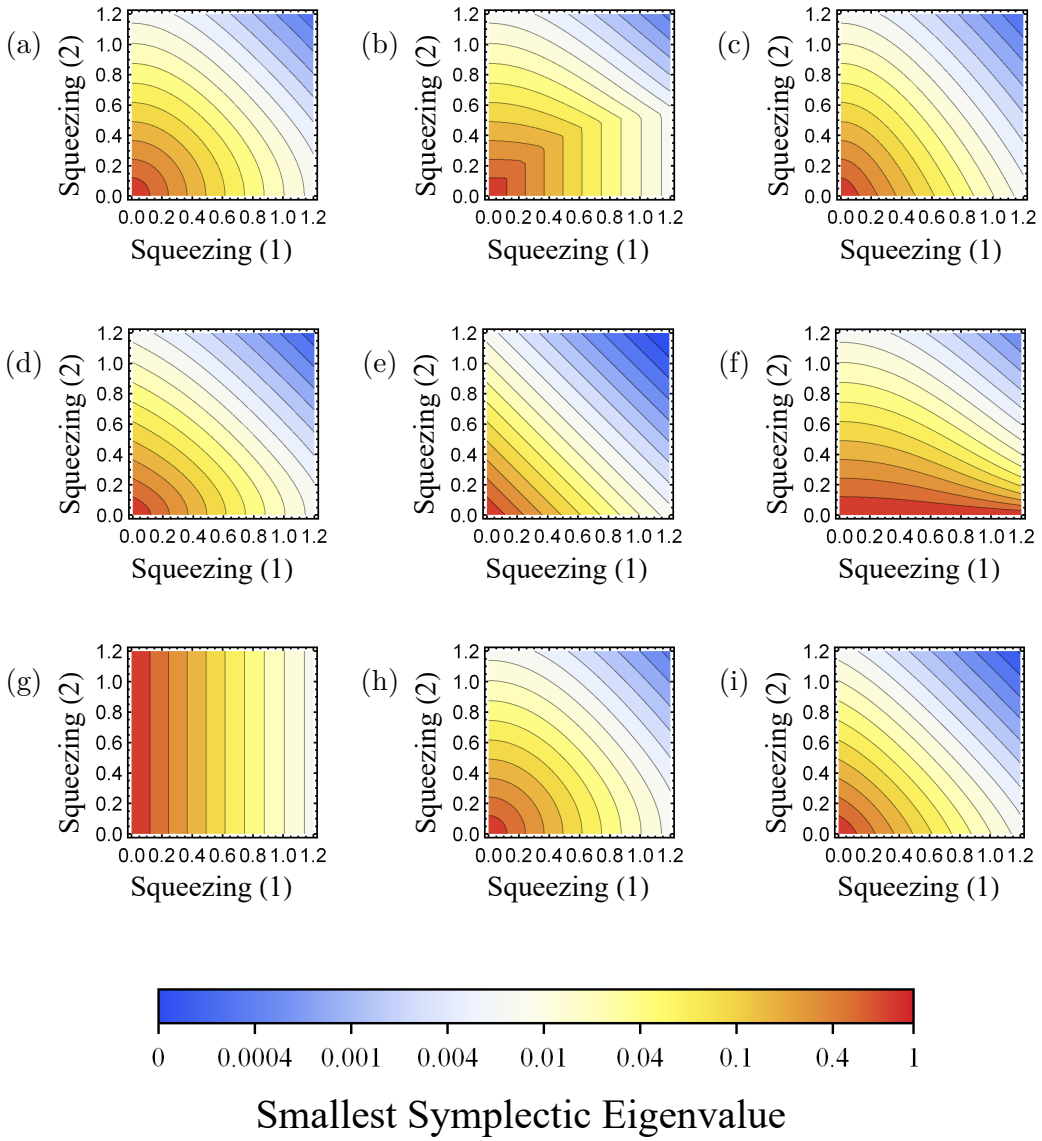

Figure B.2: PPT criteria for bipartition of form (a) 1×5 [a|bcdef, b|acdef, c|abdef, d|abcef, e|abdf, f|abcde], (b) 3×3 [abe|cdf, bef|acd, cef|abd], (c) 3×3 [ade|bcf, adf|bce, bde|acf] ,(d) 3×3 [abc|def, abf|cde, aef|bcd], (e) 3×3 [ace|bdf, bdf|ace], (f) 2×4 [ab|cdef, ef|abcd, cd|abef],(g) 2×4 [ad|bcef, be|acdf, cf|abde], (h) 2×4 [af|bcde, bc|adef ,de|abcf], and (i) 2×4 [ae|bcdf, bf|acde,ce|abdf, df|abce, ac|bdef, bd|acef]

partitions composed only of second nearest neighbors [ace|bdf, bdf|ace]. In Fig. B.2(b), the plot exhibits a discontinuous behavior because we are choosing the smallest eigenvalue from competing processes from the first stage and the second stage.

Figures B.2(f) through (i) show four cases of bipartitions of the form 2×4: bipartitions between nearest neighbors connected through a first stage and the rest of the system [ab|cdef, ef|abcd, cd|abef], bipartitions between nearest neighbors connected with a second stage and the rest of the system [ad|bcef, be|acdf, cf|abde], bipartitions between third nearest neighbors and the rest of the system [af|bcde, bc|adef ,de|abcf], and bipartitions between second nearest neighbors and the rest of the system [ae|bcdf, f|acde, ce|abdf, df|abce, ac|bdef, bd|acef].

B.4 Two Difference Cases in Hexapartite Genuine Multipartite Entanglement

As explained in Sec. 7.2.2, we find that bipartitions with nearest neighbors with a first stage connection show more entanglement than ones with a second stage connection. As we have discussed in Sect. 7.2.2, the ones with first stage connection have entangling operations applied first, while the ones with second stage connections have the amplification noise added first, as shown in Fig. B.3.

(a)

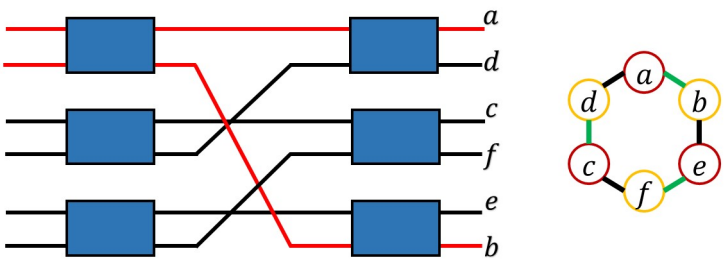

(b)

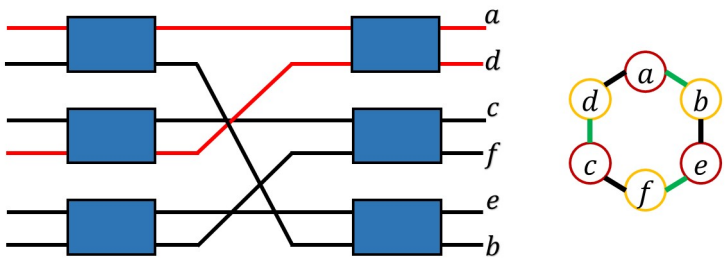

Figure B.3: Two difference cases for the nearest neighbor with (a) a-b are connected by the first stage connection and (b) a-d are connected by second stage connection.

We compare the covariance for these two cases,

$$V_{ab} = 2\sinh^2(s_2)\left[\cosh^4(s_1)\cosh^2(s_2) + \sinh^4(s_1)\cosh^2(s_2) + \sinh^2(s_1)\cosh^2(s_1)\sinh^2(s_2)\right],$$
$$V_{ad} = 2\sinh^2(s_1)\cosh^2(s_1). \tag{B.4}$$

While the covariance between the two modes with a correlation from the first stage

shows a dependence on the squeezing parameters for the first and the second stages, the covariance between the two modes with a connection from the second stage shows a dependence only on the squeezing parameter for the first stage.

When we assume the same squeezing parameter for the first and second stages $s = s_1 = s_2$, the ratio between the two covariances becomes $V_{ab}/V_{ad} = 2\sinh^4(s) + \cosh^4(s)$. This ratio increases exponentially as the squeezing increase, which indicates that connections from a second stage have stronger correlations than connections from a first stage. This is why we find a stronger violation for partitions with nearest neighbor connected by a first stage PA.